

Dissertations and Theses

---

8-2019

## Non-Linear Magnetosphere-Ionosphere Interactions at High Latitudes

Beket Tulegenov

Follow this and additional works at: <https://commons.erau.edu/edt>



Part of the Engineering Physics Commons

---

### Scholarly Commons Citation

Tulegenov, Beket, "Non-Linear Magnetosphere-Ionosphere Interactions at High Latitudes" (2019).  
*Dissertations and Theses*. 473.  
<https://commons.erau.edu/edt/473>

---

This Dissertation - Open Access is brought to you for free and open access by Scholarly Commons. It has been accepted for inclusion in Dissertations and Theses by an authorized administrator of Scholarly Commons. For more information, please contact [commons@erau.edu](mailto:commons@erau.edu).

**NON-LINEAR  
MAGNETOSPHERE-IONOSPHERE  
INTERACTIONS AT HIGH LATITUDES**

By

Beket Tulegenov

A Dissertation

Submitted to the Department of Physical Sciences

in Partial Fulfillment of the Requirements

for the Degree of

**DOCTOR OF PHILOSOPHY in ENGINEERING PHYSICS**

August 2019

Embry-Riddle Aeronautical University

Daytona Beach, Florida

© Copyright by Beket Tulegenov 2019

All Rights Reserved

**NON-LINEAR MAGNETOSPHERE-IONOSPHERE INTERACTIONS  
AT HIGH LATITUDES**

by

Beket Tulegenov

This Dissertation was prepared under the direction of the candidate's Dissertation Committee Chair, Dr. Anatoly V. Streltsov, and has been approved by the members of the Dissertation Committee. It was submitted to the Department of Physical Sciences in Partial Fulfillment of the Requirements for the Degree of

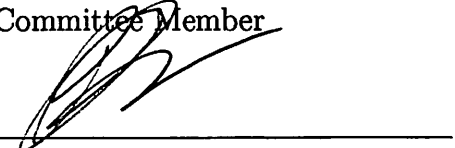
**DOCTOR OF PHILOSOPHY in ENGINEERING PHYSICS**

**Ph.D. Dissertation Committee:**

  
Dr. Anatoly Streltsov,  
Committee Chair

  
Dr. Bereket Berhane,  
Committee Member

  
Dr. Katariina Nykyri,  
Committee Member

  
Dr. Bogdan Udrea,  
Committee Member

  
Dr. Terry Oswalt,  
Department Chair, Physical Sciences

  
Dr. Karen Gaines,  
Dean, College of Arts and Sciences

  
Lon Moeller, J.D.,  
Senior Vice President for Academic Affairs and Provost

08/25/2019

Date

## Acknowledgments

First, I would like to express my sincere and deepest gratitude to my advisor, Dr. Anatoly Streletsov, for his guidance and knowledge. His patience and strong optimistic support helped me succeed in finishing this dissertation, and in shaping the views on the future prospects. I would also like to thank my dissertation committee members Drs. Nykyri, Berhane, and Udrea for the moral support they have provided throughout my years at Embry-Riddle. I really appreciate the time and effort that you have dedicated to me in your classes and in helping improving this body of work. I would also like to acknowledge the support of the Department of Physical Sciences throughout my years in the graduate school.

A big separate thank you is given to all of the past and current Ph.D. students, that helped me in staying focused on the research by distracting me from it. Big spasibo to my CIS brotherhood. Thank you Gaben and Icefrog for the thousand hours of my life that I owe you.

And a huge warm thank you to my mom Zhannat, dad Kairat, and sister Dina for simply being with me and loving me. I greatly respect your support and courage to send me to another side of the world for me to pursue my dreams.

To the memory of my grandparents Tolegen and Bibizada,  
who always believed in me

# Abstract

Non-linear, 3D electromagnetic coupling between the ionosphere and magnetosphere is investigated in this dissertation. The study is based on a non-linear, 3D, reduced magnetohydrodynamic model describing interaction between dispersive Alfvén waves and the nightside high-latitude ionosphere. Results are presented from a numerical study of small-scale, intense magnetic field-aligned currents observed in the vicinity of the discrete auroral arc by the Magnetosphere-Ionosphere Coupling in the Alfvén Resonator (MICA) sounding rocket launched from Poker Flat, Alaska, on 19 February 2012. The goal of the MICA project was to investigate the hypothesis that such currents can be produced inside the ionospheric Alfvén resonator by the ionospheric feedback instability (IFI) driven by the system of large-scale magnetic field-aligned currents interacting with the ionosphere. Simulations of the reduced 2D MHD model with realistic background parameters confirm that IFI indeed generates small-scale ULF waves inside the IAR with frequency, scale-size, and amplitude showing a good, quantitative agreement with the observations.

The 3D model was used to verify the results from the ionospheric heating experiment conducted at the High Frequency Active Auroral Research Program (HAARP) facility, Alaska, on March 12, 2013. During the experiment, HAARP transmitted in the direction of the magnetic zenith X-mode 4.57 MHz wave. The transmitted power

was modulated with a frequency of 0.9 mHz, and it was pointed on a 20 km spot at the altitude of 120 km. It was observed that this artificially initiated heating 1) generated disturbances in the magnetic field detected with the fluxgate magnetometer on the ground, and 2) produced bright luminous spots in the ionosphere, detected with the HAARP telescope. Numerical simulations of the 3D reduced MHD model reveal that these effects can be related to the magnetic field-aligned currents, excited in the ionosphere by changing the conductivity in the E-region when the large-scale electric field exists in the heating region.

The importance of the Hall currents in magnetosphere-ionosphere interactions, carried by ULF waves and field-aligned currents, has been consistently overlooked in studies devoted to the active experiments. Simulations of the 3D two-fluid MHD model, presented in this study, demonstrate that the Hall conductivity changes 1) the growth rate and the amplitude of ULF waves generated by the heating and 2) the orientation and the direction of propagation of the generated waves. These findings provide insight into the experiments where the waves were generated with a geometric modulation technique, and suggest a new and more efficient approach for conducting such experiments in the future.

# Contents

<b>Abstract</b>	<b>vi</b>
<b>List of Figures</b>	<b>x</b>
<b>1 Introduction</b>	<b>1</b>
1.1 Motivation . . . . .	1
1.2 Global Magnetospheric Resonator . . . . .	6
1.3 Ionospheric Alfvén Resonator . . . . .	10
1.4 Ionospheric Feedback Instability . . . . .	15
<b>2 MHD Numerical Model</b>	<b>20</b>
2.1 Magnetospheric Model . . . . .	20
2.2 Numerical Implementation of the Magnetospheric Model . . . . .	25
2.3 Numerical Domain . . . . .	28
2.4 Boundary Conditions . . . . .	31
2.5 Background Parameters . . . . .	35
2.6 Numerical Algorithms . . . . .	38
<b>3 2D Model: Modeling of MICA Sounding Rocket Observations</b>	<b>40</b>
3.1 Introduction . . . . .	40
3.2 MICA Data . . . . .	43
3.3 Numerical Implementation and Boundary Conditions . . . . .	47
3.4 Results and Discussions . . . . .	50
3.5 Chapter Conclusion . . . . .	59

<b>4 3D Model: Artificial Aurora</b>	<b>62</b>
4.1 Introduction . . . . .	62
4.2 The HAARP Heating Experiment . . . . .	65
4.3 Numerical Implementation and Boundary Conditions . . . . .	69
4.4 Results and Discussion . . . . .	71
4.5 Chapter Conclusion . . . . .	79
<b>5 3D Model: Efficient method of generating ULF/ELF waves</b>	<b>80</b>
5.1 Introduction . . . . .	80
5.2 Numerical Implementation and Boundary Conditions . . . . .	84
5.3 Results and Discussion . . . . .	86
5.4 Chapter Conclusion . . . . .	92
<b>6 Conclusions and Future Work</b>	<b>94</b>
6.1 Conclusions . . . . .	94
6.2 Future Work . . . . .	99
<b>Bibliography</b>	<b>100</b>

# List of Figures

1.1	Linear discreet auroral arc.	4
1.2	Nonlinear auroral forms.	5
1.3	Schematic diagram of the global magnetospheric resonator.	6
1.4	Signatures of the ULF waves trapped inside the global magnetospheric resonator.	8
1.5	Excitation of ULF waves inside the global magnetospheric resonator.	9
1.6	Schematic diagram of the ionospheric Alfvén resonator.	11
1.7	IAR boundaries.	12
1.8	Experimental IAR signatures.	13
1.9	Alfvén waves inside the IAR.	14
1.10	Ionospheric feedback mechanism explained.	16
1.11	Ionospheric feedback instability loop.	17
1.12	Structures generated by ionospheric feedback instability numerically.	19
2.1	Schematic 3D view of the numerical domain.	29
2.2	2D view of the numerical domain.	30
2.3	Schematic view of the boundary conditions implemented in the model.	32

3.1	Venetie keogram during MICA experiment. . . . .	44
3.2	In-situ measurements taken by MICA rocket. . . . .	46
3.3	Computational domain for the MICA event. . . . .	48
3.4	Dynamics of the IFI generated currents. . . . .	53
3.5	ULF waves generated inside IAR. . . . .	54
3.6	Comparison of currents measured and modeled for arc B. . . . .	55
3.7	Spectral comparison between measured and modeled signals for arc B. . . . .	56
3.8	Comparison of currents for the arc A case. . . . .	58
3.9	Comparison between measured and modeled fields. . . . .	60
4.1	Magnetometer measurements above HAARP during the experiment. .	67
4.2	Optical response of the ionosphere to the HF heating. . . . .	68
4.3	Artificial aurora in 557.7 nm and 630.0 nm. . . . .	69
4.4	Electric field in the ionosphere above HAARP during the experiment.	72
4.5	Ionospheric density above HAARP during the experiment. . . . .	73
4.6	3D view of the FACs produced by the model. . . . .	76
4.7	Ionospheric heating for cases with $\Sigma_H/\Sigma_P=2$ and $\Sigma_H/\Sigma_P=0$ . . . . .	77
5.1	3D model output of the FLR generated by heating a fixed location. .	86
5.2	Comparison between two heating methods ( $\Sigma_H = 0$ ). . . . .	88
5.3	ULF wave propagation angle as a function of $\Sigma_H/\Sigma_P$ . . . . .	90
5.4	Comparison between two heating methods ( $\Sigma_H/\Sigma_P = 2$ ). . . . .	92

# Chapter 1

## Introduction

### 1.1 Motivation

Ultra-Low-Frequency (ULF) Alfven waves carry significant fluxes of electromagnetic energy along auroral magnetic field lines and play a major role in the redistribution of electromagnetic power, particle density, mass, and momentum between the ionosphere and the magnetosphere at high latitudes. A particularly important feature of these waves is their casual connection with discrete auroral arcs. Today there is a significant understanding of mechanisms responsible for the generation of two-dimensional, “linear” systems of magnetic field-aligned currents associated with ULF Alfven waves at high latitudes. But several important questions related to the nonlinear, 3D dynamics of these waves remain unanswered. These questions include:

- What is the role of ionospheric feedback instability in the ionosphere on the development of intense field-aligned currents (FACs) and active discrete auroral forms?

- Which part of the coupled MI system is responsible for the development of quiet homogeneous discrete auroral arcs?
- Which part of the coupled MI system is responsible for the intensification, break-up, and rapid, nonlinear dynamics of the FACs/arcs?

To answer these questions, a nonlinear, 3D, time-dependent, numerical model describing dynamics of ULF Alfvén waves in the magnetosphere and the active electromagnetic coupling between these waves and the ionospheric plasma is developed in this dissertation. This model is used for the investigation of spatiotemporal properties and dynamics of intense ULF waves and magnetic field-aligned currents at high latitudes.

Electrodynamics of magnetosphere-ionosphere interactions at high altitudes involving ultra-low-frequency (ULF) Alfvén waves has been extensively studied for more than 40 years [e.g., *Radoski*, 1967; *Cummings et al.*, 1969]. The initial goal of these studies was to explain geomagnetic pulsations in the Pc5-Pc6 frequency range measured by ground-based magnetometers in the auroral zone. Later, the interest in Alfvén waves steadily increased with observations showing that these waves can be responsible for parallel electron acceleration and the occurrence of discrete auroral arcs [*Xu et al.*, 1993; *Marklund et al.*, 1994; *Samson et al.*, 1991, 1996; *Lotko et al.*, 1998]. Direct measurements from satellites [*Chmyrev et al.*, 1988; *Karlsson and Marklund*, 1996; *Chaston et al.*, 2002; *Chaston*, 2003; *Figueiredo et al.*, 2005] and rockets [*Boehm et al.*, 1990] have shown that the discrete fluxes of keV electrons registered at the auroral zone are often correlated with intense, localized, electromagnetic disturbances sometimes interpreted as dispersive Alfvén waves.

An observed connection between ULF waves and discrete auroral arcs can be ex-

plained by the hypothesis that discrete arcs are produced by magnetic field-aligned currents (FACs) carried by ULF Alfvén waves propagating along auroral magnetic field lines. The main questions which remain unanswered, to some extent, are how and where these waves are generated, and what mechanism defines their frequencies and relatively small perpendicular wavelengths. Some studies suggest that they are generated by interactions between solar wind and plasma in the magnetotail and/or equatorial magnetosphere, [e.g., *Angelopoulos et al.*, 2002; *Keiling et al.*, 2000], and the wave frequencies are defined by the external driver (e.g., variations in pressure/density of the solar wind) [*Kepko et al.*, 2002] or by the parameters of the magnetosphere along the auroral magnetic field line, inside the so-called magnetospheric field-line resonator (FLR) [*Cummings et al.*, 1969; *Chen and Hasegawa*, 1974; *Southwood*, 1974; *Kivelson and Southwood*, 1985; *Samson et al.*, 1992]. The main idea of FLR is that shear Alfvén waves can form a standing pattern along a particular magnetic field line, with eigenfrequency which matches the eigenfrequency of the global magnetospheric cavity/waveguide. Here, the coupling between shear Alfvén waves and fast MHD modes occurs. This coupling produces standing waves with relatively small perpendicular wavelengths due to the phase mixing of the resonant oscillations [*Mann et al.*, 1995; *Russell and Wright*, 2010].

Other studies suggest that the small-scale ULF waves can be generated by the electric field in the ionosphere due to the non-linear interaction between magnetic field-aligned currents and the ionospheric plasma [*Atkinson*, 1970; *Sato*, 1978; *Watanabe et al.*, 1993]. In general, it is possible that one of these scenarios can be realized under one type of geophysical condition and another can be realized under different conditions. Due to the fact that the magnetosphere and the ionosphere form a very



Figure 1.1: “Linear” discreet auroral arcs. Courtesy of Jan Curtis.

complex, dynamic, nonlinear coupled system, sometimes it is hard to distinguish the causes and the consequences of the large-scale geophysical processes based on observations performed only in one particular location and during the relatively short time interval. One way to reveal the connection between intense, localized ULF waves and the discrete auroral arcs is to develop a comprehensive numerical model of the electrodynamic coupling between the ionosphere and the magnetosphere and to reproduce in quantitative detail different characteristic features of the observations. Today there is a significant understanding of mechanisms responsible for the generation of “linear” discrete auroral arcs (See Figure 1.1). However, there are a great number of observations which cannot be explained with these models. For example, observations from the FAST, Polar, and Cluster satellites [Wygant *et al.*, 2000; Keiling *et al.*, 2000; Aikio *et al.*, 2004; Dombeck *et al.*, 2005; Figueiredo *et al.*, 2005] show that a significant fraction of the aurora is powered by intense, small-scale Alfvén waves propagating along the magnetic field lines and passing through the plasma sheet boundary layer. These magnetic field lines are stretched in the tailward direction and not always well de-



Figure 1.2: (Left) Auroral “curls” or “vortex chain”. (Right) “Rayed” aurora. Courtesy of Jan Curtis.

fined. Such facts make it hard to explain these waves with the classical, “linear” FLR theory, which requires closed magnetic field line geometry; although some attempts have been made [e.g. *Rankin et al.*, 2000]. At the same time, frequencies of the waves detected in these observations are much lower than the frequencies predicted by the IAR theory and they are detected in the magnetosphere much above the altitude where the upper boundary of the IAR is located [*Karlsson et al.*, 2004]. A number of similar observations have been reported by Cluster scientists from the University of Stockholm [e.g. *Johansson et al.*, 2004, 2005, 2006]. Other important questions which also are not answered yet are explaining the 3D structures and 3D dynamics of the discrete auroral arcs. Figure 1.2 shows two examples of these structures: “curls” or “vortex chain” (on the top) and “rayed” aurora (on the bottom). The questions of what physical mechanism in the magnetosphere or in the ionosphere causes development of these forms, their spatial sizes, frequencies, and dynamics are the main focus of this investigation. Some studies suggest that these forms are the result of Kelvin-Helmholtz instability in the equatorial magnetosphere [*Rankin et al.*, 1993; *Russell and Wright*, 2010]. Other studies suggest that they are a result of nonlinear

magnetosphere-ionosphere interactions at high latitudes [Keskinen *et al.*, 1988; Lysak and Song, 1996].

## 1.2 Global Magnetospheric Resonator

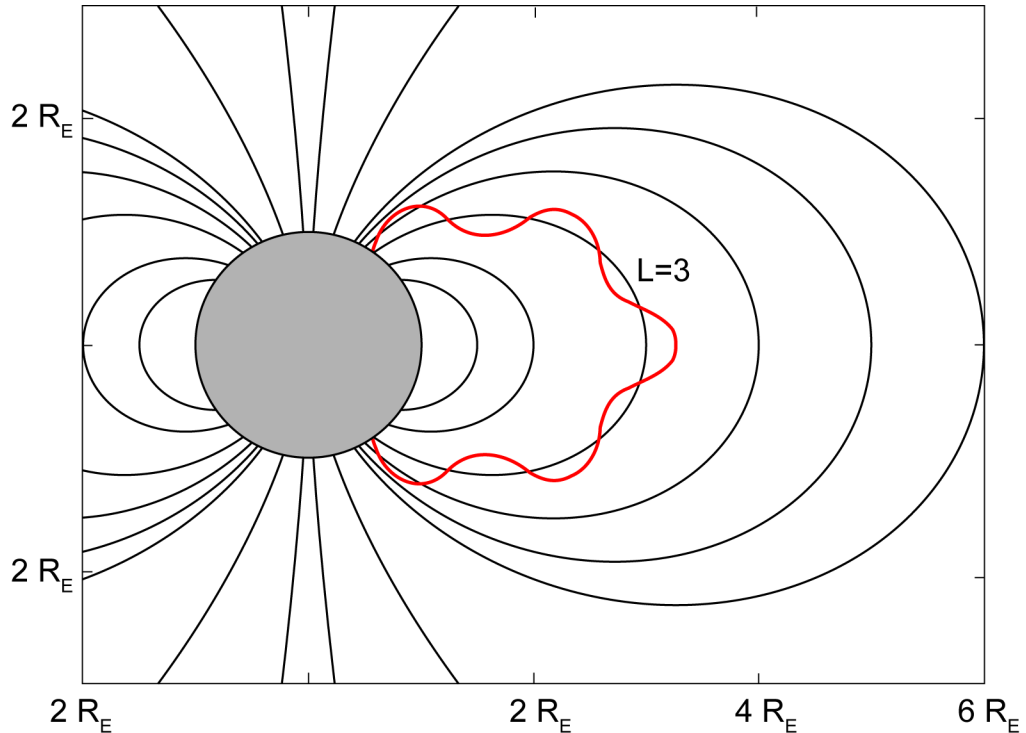


Figure 1.3: Schematic diagram of the global magnetospheric resonator formed by the magnetic dipole flux tube bounded at both ends by highly conducting ionosphere.

The shear Alfvén Field-Line Resonance (FLR) has been studied extensively for over 70 years. FLRs can be excited in the magnetosphere by the coupling of the shear Alfvén mode with the MHD compressional wave [Chen and Hasegawa, 1974; Southwood, 1974]. Ultra-low frequency (1 - 10 mHz) magnetic pulsations have been measured using networks of ground magnetometers and identified as transverse oscil-

lations of dipole magnetic flux tubes [Dungey, 1955]. These transverse hydromagnetic waves form standing wave patterns along the dipole magnetic flux tube which are bounded by the conducting ionosphere at both ends [Cummings *et al.*, 1969; Streltsov *et al.*, 1998a]. Recently, Archer *et al.* [2019, and references therein] have reported that magnetopause surface eigenmode ULF waves were measured using multipoint THEMIS spacecraft observations. Figure 1.3 shows the schematic diagram of the FLR structure in the inner magnetosphere. In simple terms, the FLR is formed when the frequency of the compressional signal acting as an energy source matches the eigenfrequency of the particular magnetic field line [Chen and Hasegawa, 1974; Radoski, 1967; Southwood, 1974]. The fundamental harmonic of standing waves that are formed inside of the global resonator have antinodes on the equatorial plane and nodes on the the ionospheric ends. The eigenfrequency of the resonant wave increases as the radial distance decreases in the dipolar domain of the magnetosphere [Samson *et al.*, 1992]. The FLR has been investigated in detail in the auroral regions due to the similarity in structure and behaviour to the auroral arcs. They are commonly seen in ground-based magnetometer observations [Samson *et al.*, 1992] and HF radar readings [Ruohoniemi *et al.*, 1991]. Waves produced inside the global resonator are considered to be large-scale having radial scale size of the order of  $0.1R_E$  in the equatorial magnetosphere.

In the auroral regions of the ionosphere, the latitudinal scale sizes of the waves are reaching tens of km [Samson *et al.*, 1992; Walker *et al.*, 1992]. Figure 1.4 shows the ground magnetometer data taken on September 28, 1988 from four stations that were part of CANOPUS array [Samson *et al.*, 1992]. This array is part of Canadian Auroral Network. The standing wave model describes the basics of the wave structure along

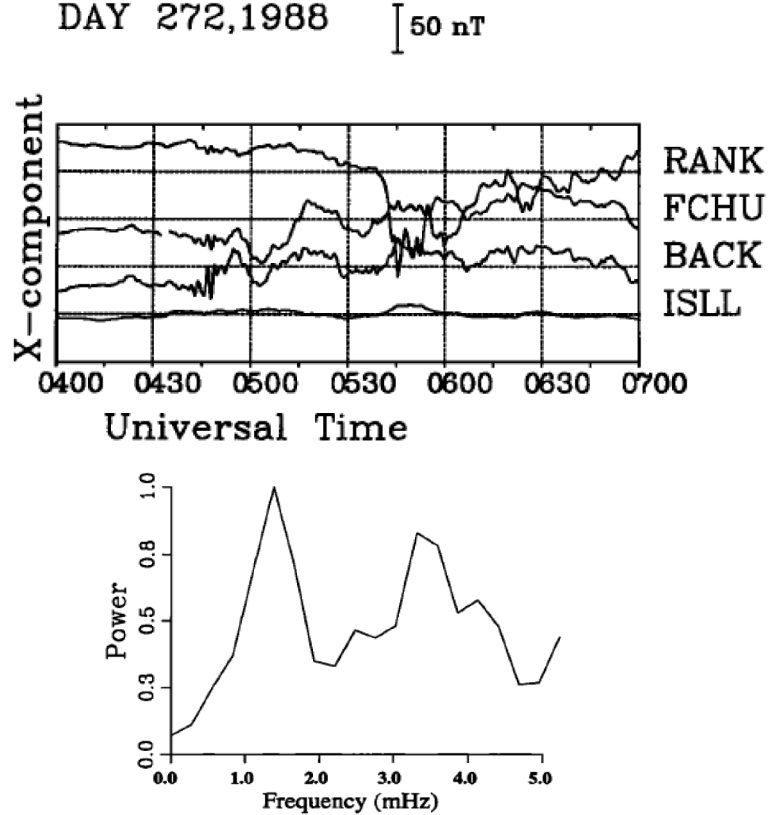


Figure 1.4: Top panel shows the X-component of the magnetic field at four stations of CANOPUS array on September 28, 1988. ULF pulsations are clearly displayed in the interval from 04:20 to 04:50 UT at BACK station. Bottom panel shows power spectrum of the X-component magnetometer data from BACK station in the interval from 04:00 to 05:00 UT taken on September 28, 1988. The signal has peaks at 1.3 mHz and 3.4 mHz. Figures are adapted from [Samson *et al.*, 1992].

the dipole flux tube and signal polarization [Sugiura and Wilson, 1964; Cummings *et al.*, 1969]. Numerical MHD Alfvén models are successfully used to determine spatio-temporal behaviour of the ionosphere and magnetosphere inside the FLR under various geomagnetic conditions [e.g. Hasegawa, 1976; Chmyrev *et al.*, 1988; Seyler, 1990; Streltsov *et al.*, 1998b; Rankin *et al.*, 2000]. Simulations with nonlinear MHD mode showed that these nonlinear effects affect the eigenfrequencies of the FLR. This

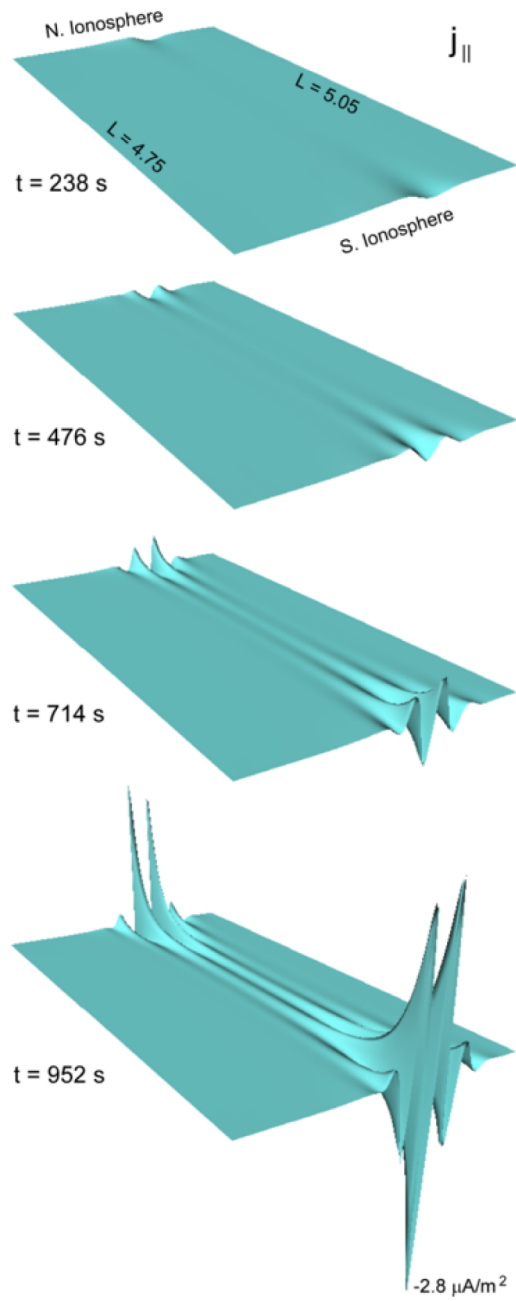


Figure 1.5: Snapshots of parallel current density  $j_{\parallel}$  displaying the growth of Alfvén wave amplitude that are excited in the global magnetosospheric resonator. Figures are adapted from 2D MHD simulations performed by Streltsov *et al.* [2005].

in turn changes the behavior of the global resonator significantly. The ionospheric conductivity is changed when particles are precipitated by the Alfvén waves, the resonant Alfvén waves themselves are dispersed when the transverse size of the global resonator layer becomes small. Figure 1.5 shows a numerical output from the 2D MHD model where the time evolution of the FLR is investigated. These snapshots indicate how the parallel current density  $j_{\parallel}$  grows and FLR forms a closed-loop field aligned current system.

### 1.3 Ionospheric Alfvén Resonator

Small-scale ( $\lambda \leq 10\text{km}$ ) Alfvén waves can be trapped in a ionospheric Alfvén resonator (IAR). This IAR is bounded from below by ionospheric E layer and from above by the sharp gradient in the electron density above the F layer, which also corresponds to the sharp gradient in the Alfvén velocity. Figures 1.6 and 1.7 show the schematic diagram of the ionospheric Alfvén resonator.

The theoretical properties of the IAR were investigated by *Polyakov and Rapoport* [1981]; *Trakhtengerts and Feldstein* [1991]; *Trakhtengertz and Feldstein* [1984] for the vertical magnetic field model. They have shown that the typical eigenfrequencies of the IAR are between 0.1 and 10 Hz. The properties of the IAR are defined by the medium along the magnetic field. Parameters that affect the properties include the physical size of the resonator, plasma density profile, plasma composition and the strength of the magnetic field. Experimental evidence was collected by *Belyaev et al.* [1990] which showed that ULF waves exist in the range from 0.1 to 10 Hz in the background noise. Figure 1.8 shows the spectrum of the horizontal component of the

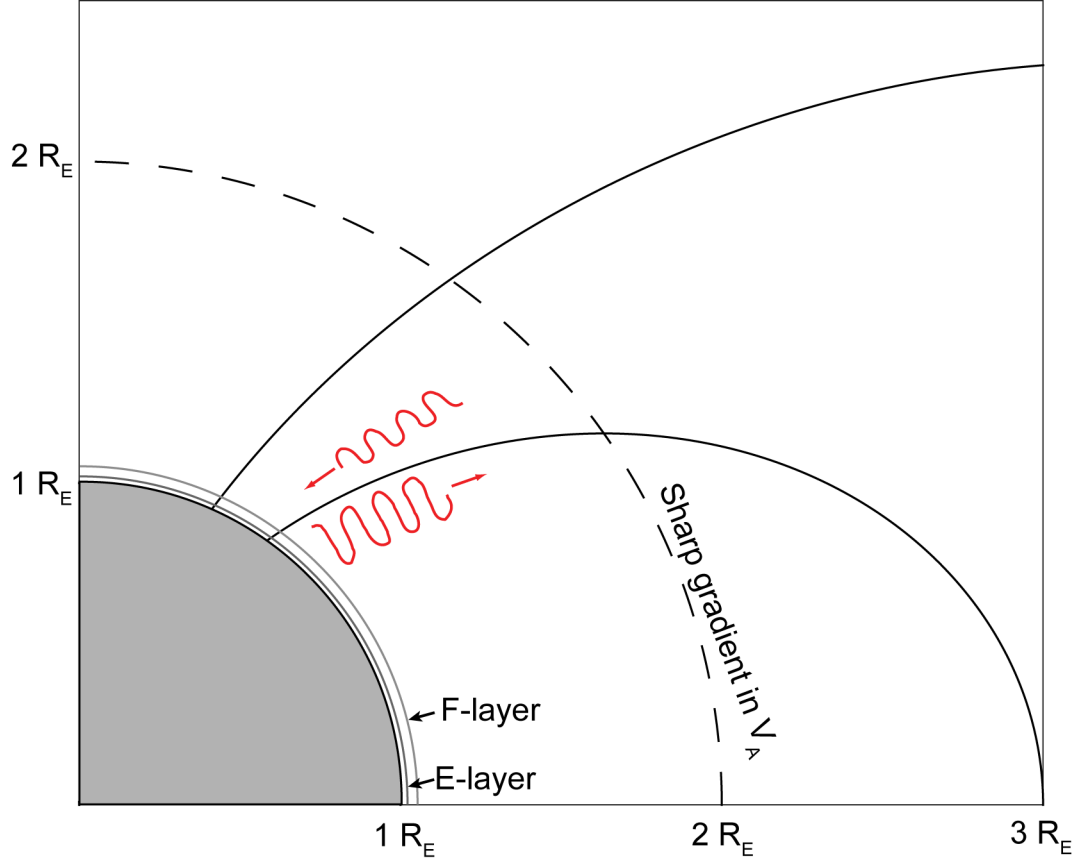


Figure 1.6: Schematic diagram of the ionospheric Alfvén resonator formed by the magnetic dipole flux tube bounded at the bottom by the ionospheric E-layer and the sharp gradient in the Alfvén speed at the altitude of 0.5-1.0  $R_E$ .

magnetic field above the Gorky station, USSR. The data collected indicates a diurnal variation of the frequencies observed in this range. Further investigations have shown that the diurnal pattern of these waves is also present at higher (auroral) latitudes [Yahnin *et al.*, 2003]. A morphological study showed that the waves are affected by the solar cycle and local geomagnetic activity.

Furthermore, both theory and experimental results suggest that the structure of the ionosphere can be inferred based on the frequencies measured. A parameter that

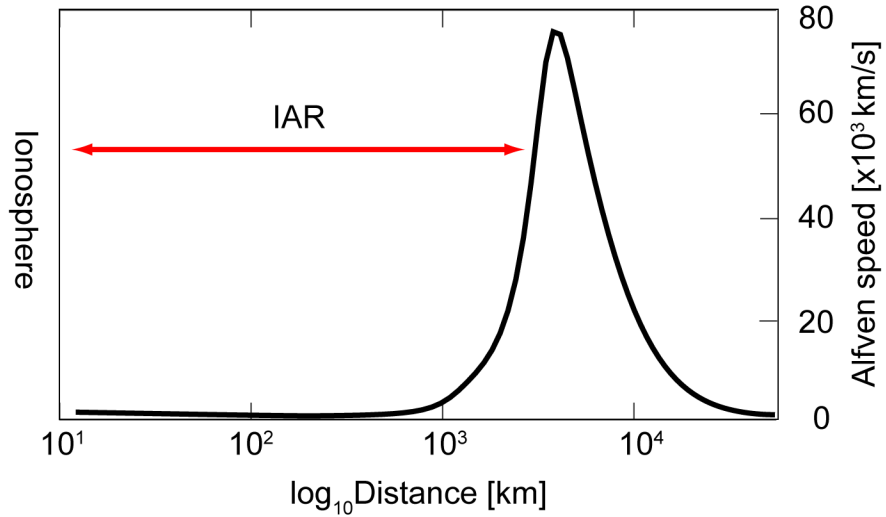


Figure 1.7: Alfvén speed profile along a magnetic field line ( $L = 7.07$ ) displaying the location of the strong gradient and forming the upper boundary of the IAR.

defines the electron density decrease above the F region can be estimated using the ground magnetometer data [*Belyaev et al.*, 1990; *Yahnin et al.*, 2003]. Latitudinal variation of the IAR was complemented by the analysis of the data at low latitudes ( $L = 1.3$ ). *Bösinger* [2002] indicated that the main characteristics of the IAR are similar to the mid and high latitude observations. The eigenfrequencies observed at  $L = 1.3$  were lower by a factor of 2 and 3 when compared to the  $L = 5.2$  values (0.4 Hz as compared to 1.0 Hz). Various numerical models are being developed to investigate the spatio-temporal properties of the IAR.

These models include both active and passive ionospheric boundary conditions and incorporate different effects. Model results presented by *Pokhotelov et al.* [2000] include the effect of the wave frequency dispersion. The results show that the ionosphere couples the shear Alfvén waves with the compressional mode. Simulations also indicate that the Hall conductivity in the ionosphere increases the growth rate of the

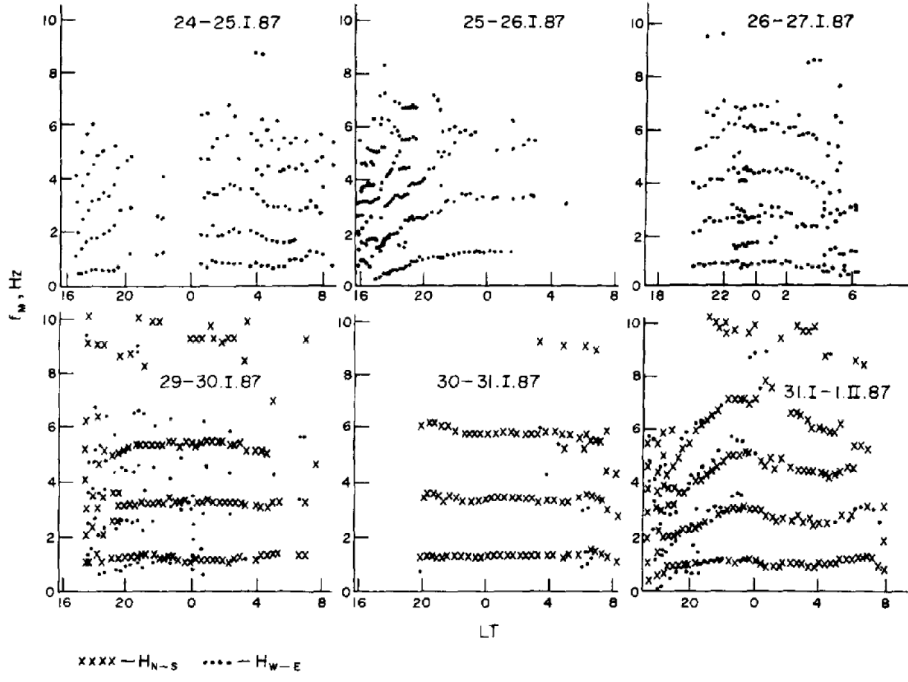


Figure 1.8: Horizontal components of the magnetic field recorded at Gorky, USSR. These measurements indicate the local time (LT) dependence of the frequencies present in the ionosphere above the station. Adapted from *Belyaev et al.* [1990].

unstable modes. It was shown that IAR may excite the unstable modes at times when the ionospheric conductivity is both low and high. Study by *Pokhotelov et al.* [2000] shows that when the Pedersen conductance in the E-layer is similar to Alfvén wave conductance the IAR generates waves with the maximum on the ionospheric ends. These types of waves can be measured by ground magnetometers. However, this is not always the case. Numerical 2D MHD simulations performed by *Streltsov et al.* [2011] show that when the conductances are higher or lower, the only way to detect these ULF waves is by flying satellites or sounding rockets through the IAR region. Numerical studies by *Streltsov and Lotko* [2003] show that the IAR develops large-amplitude, small-scale waves inside the downward current channels. These regions

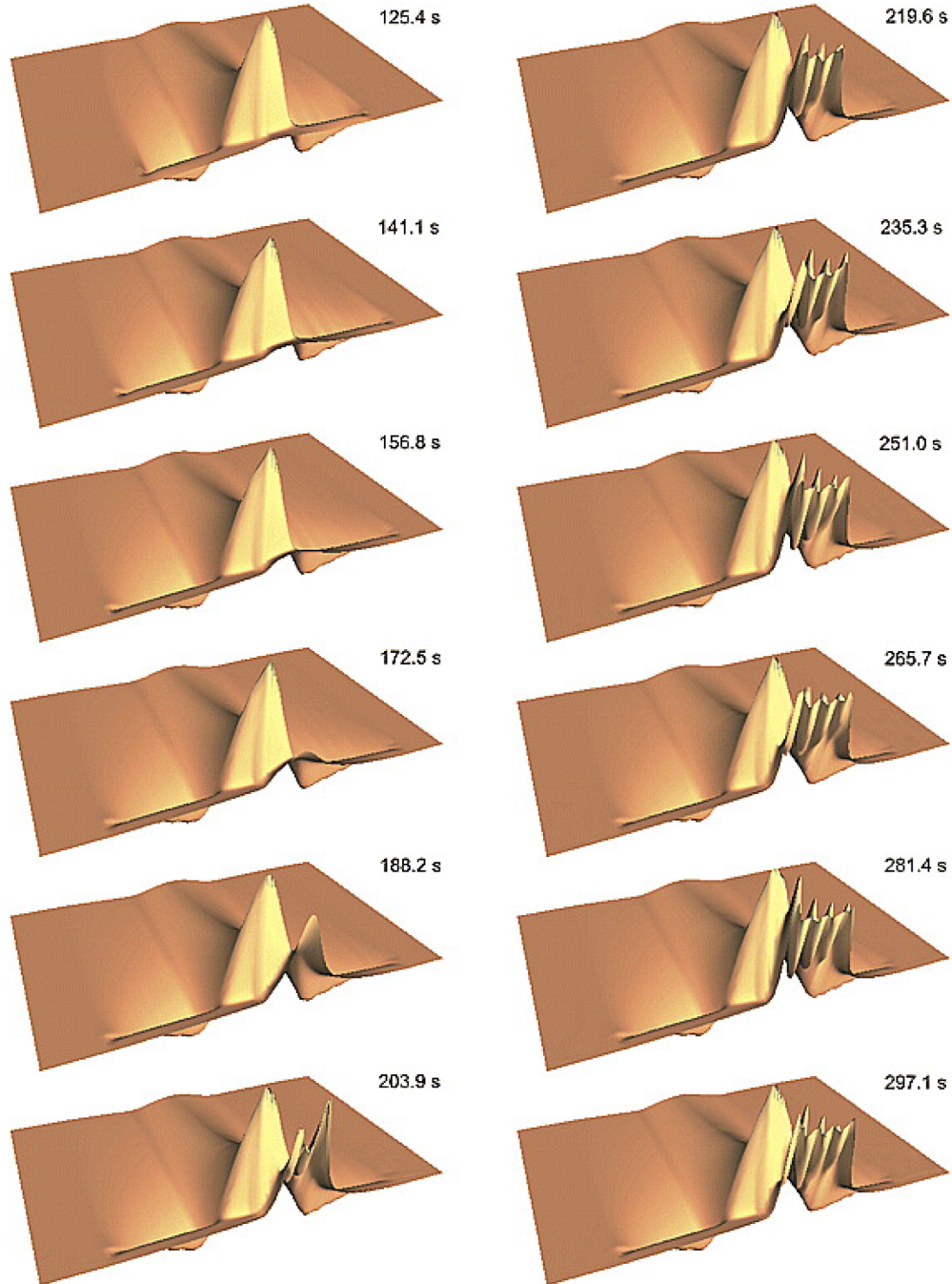


Figure 1.9: Snapshots of perpendicular electric field  $E_{\perp}$  displaying the growth of Alfvén wave amplitude that are excited inside the ionospheric Alfvén resonator. Figures are adapted from *Streltsov and Lotko* [2003].

are theoretically adjacent to the discrete auroral arcs. Figure 1.9 shows the growth of the resonant waves in the IAR inside the MHD model used by *Streltsov and Lotko* [2003].

## 1.4 Ionospheric Feedback Instability

Currently, the ionospheric feedback instability (IFI) is the widely accepted mechanism for the generation of small-scale large amplitude structures at high latitudes. It was first introduced by *Atkinson* [1970] and later investigated further by *Sato* [1978] and *Lysak* [1990, 1991]. The feedback is produced when the magnetic field-aligned currents (a system of an upward and downward currents that are connected through a background current) change the conductivity in the ionosphere by precipitating and removing electrons from it. Conductivity is directly proportional to density. The field-aligned currents are formed at the gradients of the conductivity enhancement. The upward current increases the ionization, and recombination happens in the downward current region. This results in the conductivity peak moving in the direction of the background current as indicated in Figure 1.10.

Qualitative analysis by *Lysak* [1991] has shown that the free source of energy for the instability comes from the reduced Joule dissipation. A consequent study by *Lysak and Song* [2002] concluded that IFI generates structures most effectively when the background conductivity is low and there is a large background electric field present in the ionosphere. Qualitatively, the incident small-scale shear Alfvén wave over-reflects in the presence of a large scale electric field [*Trakhtengertz and Feldstein*, 1984; *Lysak and Song*, 2002]. Over reflection means that the amplitude of the wave

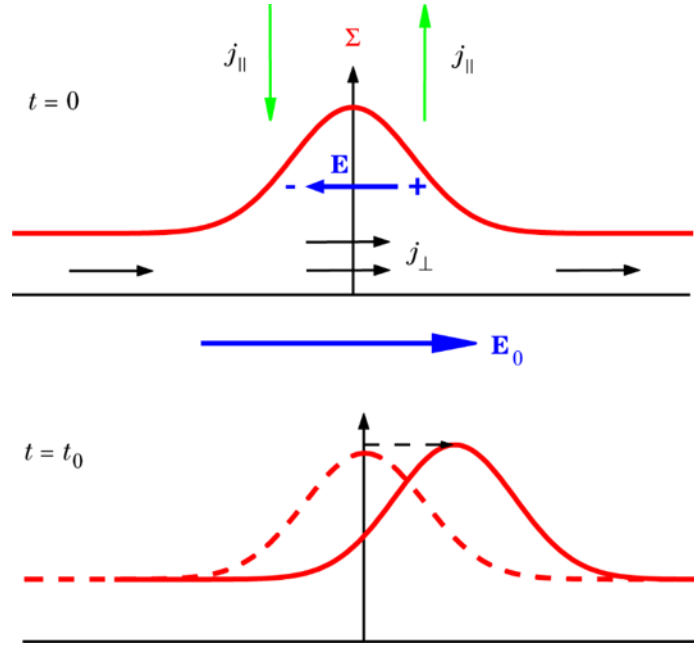


Figure 1.10: Ionospheric feedback mechanism explained. Top panel shows an increase in the background current in the region where a conductivity enhancement is present. This increase in current is the closure of the field-aligned currents that are generated on both sides of the conductivity peak. Bottom panel shows the propagation of the conductivity peak in the direction of the background current. This is a result of recombination happening on the downstream side of the peak and ionization increase on the upstream part of the conductivity peak. Figures are adapted from *Lysak [1990]*.

reflected from the ionosphere is larger than the amplitude of the incident wave. This occurs when the field aligned current in the small-scale wave locally enhances the ionospheric conductivity and reduces the Joule dissipation of the large-scale electric field in this location. The field energy is then released in the form of a magnetic field-aligned current propagating away from the ionosphere. This additional current makes the reflection coefficient greater than 1. When this wave interacts with the active ionosphere multiple times, the wave's amplitude increases significantly. Figure 1.11 shows the feedback cycle.

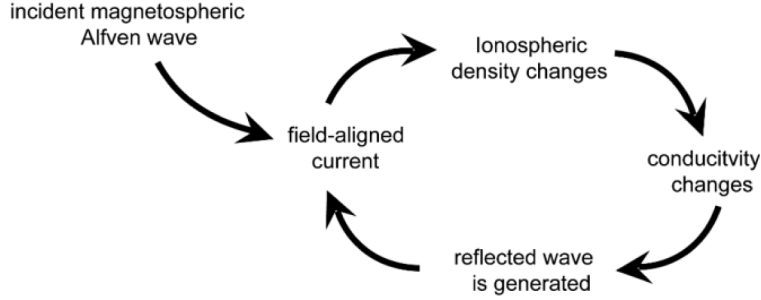


Figure 1.11: Ionospheric feedback instability mechanism explained.

Various linear [*Lysak and Song*, 2002; *Hiraki and Watanabe*, 2011] and nonlinear [*Doe et al.*, 1995; *Streltsov and Lotko*, 2004] models are used to study the dynamics and properties of the IFI in the ionosphere-magnetosphere coupling. These studies show that the intermediate (10-20 km) and small-scale structures ( $\leq 10$  km) can be generated in the ionosphere under the presence of large-scale FACs when the conductivity is low and the background electric field is large ( $> 20$  mV/m). 2D MHD simulations by *Streltsov and Lotko* [2004] show that the small-scale structures are produced in the downward current channels (depleted regions of the FACs). These results suggest that the small-scale ULF structures should be frequently observed in low-orbit satellite measurements passing the discrete auroral arcs. The conditions favorable for the IFI are satisfied in the return current channels associated with the discrete auroral arcs. These return (downward) current channels have relatively low conductivity and large perpendicular electric field. Figure 1.12 shows the numerical output of a simulation where two FACs generated small-scale structures [*Streltsov et al.*, 2010]. One should observe the fact that small-scale structures are produced in the downward current channel.

If IFI generated small-scale structures encounter a sharp gradient in the Alfvén speed in the magnetosphere, they can be reflected and trapped inside the IAR. The

amplitude growth of these waves will be linear initially but after passing a threshold will become nonlinear. In the nonlinear regime the amplitudes of the generated waves are in the order of  $100 \mu\text{A/m}^2$ . Such large amplitude currents can produce density cavities through the ponderomotive force, in the form of a nonlinear Lorentz force  $(\frac{B_y}{v_A^2} \frac{\partial E_x}{\partial t})$  [*Streltsov and Lotko, 2008*]. Simulations by *Streltsov and Karlsson [2008]* show that the ponderomotive force generated in the IAR with IFI creates a cavity in the ionosphere. The density inside of the cavity produced is  $\approx 10\%$  of the initial background value. 3D MHD numerical simulations, performed with the active ionospheric response to the large-scale FACs, show that the IFI plays an important role in the formation of small-scale vortex chains in the discrete auroral arcs [*Jia and Streltsov, 2014*]. The convective nonlinear part of the code shows that the linear discrete auroral arcs can develop a series of curls based on different ionospheric conductivity and background electric field values.

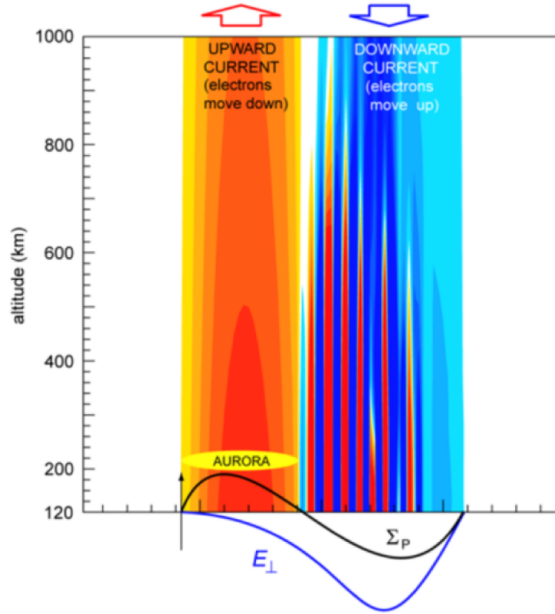


Figure 1.12: Ionospheric feedback instability generating small-scale ULF structures inside the downward current channel adjacent to the discrete aurora. Schematic plots of the perpendicular electric field and ionospheric E-region conductivity are superimposed to indicate the favorable conditions for the IFI mechanism. Adapted from Streltsov *et al.* [2010].

# Chapter 2

## MHD Numerical Model

### 2.1 Magnetospheric Model

This study is based on the numerical reduced two-fluid MHD (RMHD) model that describes the interaction of shear Alfvén waves with the inhomogeneous magnetized plasma in the magnetosphere and ionosphere. A non-reduced (full) MHD model includes the physics of slow (ion-acoustic), intermediate (shear Alfvén), and fast (magnetosonic) waves. A previous work by *Chmyrev et al.* [1988] has shown that the parallel ion motion can be neglected when focusing on the modeling of the nonlinear drift Alfvén waves in a low-pressure plasma. By assuming that only electrons are moving parallel to the background magnetic field, the full MHD model is reduced to a model that has only shear Alfvén mode in it. The model has been previously discussed in several papers devoted to electrodynamic coupling between the ionosphere and magnetosphere at high latitudes [e.g., *Streltsov et al.*, 1998a; *Streltsov and Lotko*, 2008; *Streltsov*, 2011; *Jia and Streltsov*, 2014].

In the high-latitude region, which is the focus region of this study, the plasma is assumed to be magnetized and cold ( $\beta = \frac{p_{gas}}{p_{mag}} = \frac{2\mu_0 p}{B^2} \ll 1$ ). It was shown by *Hasegawa and Uberoi* [1982] that shear Alfvén waves can be developed from the slow mode. Coupling of the shear and compressible waves is ignored near the resonant surfaces due to the fact that the plasma response is mainly magnetically incompressible near the resonant surface [*Hasegawa and Uberoi*, 1982]. Due to this assumption, the magnetospheric part of the model can be described only in terms of three governing equations.

The first equation in the model includes the electron parallel momentum equation

$$n_e \frac{\partial \mathbf{v}_e}{\partial t} + n_e \mathbf{v}_e \cdot \nabla \mathbf{v}_e = -\frac{en_e}{m_e} (\mathbf{E} + v_e \times \mathbf{B}) - \frac{1}{m_e} \nabla p_e - n_e \mathbf{v}_e \nu_e. \quad (2.1)$$

Here subscripts  $e$  and  $i$  refer to electrons and ions, respectively;  $v_e$  is the electron velocity,  $e$  is the elementary electron charge,  $n_0$  is the background quasi-neutral plasma density,  $n_e$  is the electron density,  $m_e$  is the electron mass,  $\nu_e$  is the collision frequency, and  $p_e$  is the thermal pressure.

The assumption that electrons undergo only a  $\mathbf{E} \times \mathbf{B}$  drift perpendicular to the background magnetic field direction is implemented. This simplifies such that only the parallel motion of electrons along the ambient magnetic field is considered:

$$\frac{\partial v_{\parallel e}}{\partial t} + \mathbf{v}_e \cdot \nabla v_{\parallel e} + v_{\parallel e} \nabla_{\parallel} v_{\parallel e} + \frac{e}{m_e} E_{\parallel} + \frac{1}{m_e n_0} \nabla_{\parallel} (n T_e) = -\nu_e v_{\parallel e}. \quad (2.2)$$

Here subscripts  $\parallel$  and  $\perp$  indicate parallel and perpendicular vector components to  $\mathbf{b} = \mathbf{B}_0/B_0$ , respectively;  $T_e$  is the background electron temperature, and  $c$  is the speed of light in vacuum. The collisional resistivity is included in the model because

some studies [e.g. *Borovsky*, 1993; *Lessard and Knudsen*, 2001] suggest that it may cause an absorption of very small-scale ( $\leq 1$  km) waves at altitudes below 1000 km. The effect of the collisional resistivity that slows down the electron motion along the field line plays an important role in the generation of  $E_{\parallel}$  at low altitudes [*Borovsky*, 1993]. It is implemented in the model as

$$\nu_e = \nu_{e0} e^{-(r-r_3)/R_E}, \quad (2.3)$$

where  $r_3 = 600 \text{ km}/R_E$  and  $\nu_{e0}$  is the electron collision frequency at the altitude  $r_3$ .

The second equation that controls the magnetospheric part of the model is the density continuity equation of the disturbed part of the ambient plasma. The plasma is assumed to be quasi-neutral, i.e.  $n = n_e \approx n_i$ , leading to the equation:

$$\frac{\partial n_1}{\partial t} = -\nabla \cdot (nv_{\parallel e}\mathbf{b}) - \mathbf{v}_E \cdot \nabla n. \quad (2.4)$$

Here, the drift velocity is  $\mathbf{v}_E = \mathbf{E}_{\perp} \times \mathbf{B}_0 / B_0^2$ .

The third equation used in the model is the current continuity equation which is coupled with the ion momentum equation. The derivation of this equation starts from the basic current continuity equation:

$$\nabla \cdot \mathbf{j} = 0. \quad (2.5)$$

It has two components: perpendicular and parallel current densities

$$\nabla \cdot (\mathbf{j}_{\perp} + \mathbf{j}_{\parallel}) = 0. \quad (2.6)$$

The assumption that parallel motion of ions can be neglected is implemented in the model as was shown in the paper by *Chmyrev et al.* [1988]. It is assumed that the parallel current is carried only by electrons,  $\mathbf{j}_{\parallel} = j_{\parallel}\mathbf{b}$ , while the perpendicular current is based on the contribution of both species,  $\mathbf{j}_{\perp} = en_0(\mathbf{v}_{\perp i} - \mathbf{v}_{\perp e})$ . The transverse component of current consists of polarization and displacement currents. The polarization term can be obtained from the transverse ion momentum equation:

$$\frac{\partial v_i}{\partial t} + \mathbf{v}_E \cdot \nabla v_i = \frac{e}{m}(E_{\perp} + \mathbf{v}_i \times \mathbf{B}). \quad (2.7)$$

By applying  $\times \mathbf{B}$  on both sides, the following expression is obtained

$$\frac{\partial v_i}{\partial t} \times \mathbf{B} + \mathbf{v}_E \cdot \nabla v_i \times \mathbf{B} = \frac{e}{m}(E_{\perp} \times \mathbf{B} + \mathbf{v}_i \times \mathbf{B} \times \mathbf{B}). \quad (2.8)$$

Knowing that  $\mathbf{v}_i \times \mathbf{B} = \mathbf{E}_{\perp}$  and  $\mathbf{v}_i \times \mathbf{B} \times \mathbf{B} = -\mathbf{v}_i B^2$ , the previous equation is simplified to

$$\frac{\partial \mathbf{E}_{\perp}}{\partial t}/B^2 + \mathbf{v}_E \cdot \nabla \mathbf{E}_{\perp}/B^2 = \frac{e}{m}(E_{\perp} \times \mathbf{B}/B^2 + \mathbf{v}_i). \quad (2.9)$$

By rearranging and moving  $\mathbf{v}_i$  to the left, the following expression is obtained

$$\mathbf{v}_i = \mathbf{v}_E - \frac{m}{eB^2} \left( \frac{\partial \mathbf{E}_{\perp}}{\partial t} + \mathbf{v}_E \cdot \nabla \mathbf{E}_{\perp} \right). \quad (2.10)$$

Lets introduce  $v_A = B_0/\sqrt{\mu_0 n_0 m_i}$  for the Alfvén speed. The electrons are assumed to have only an  $\mathbf{E} \times \mathbf{B}$  drift in the transverse direction, which means that the polarization current can be simplified further

$$\mathbf{j}_{\perp} = ne(\mathbf{v}_i - \mathbf{v}_e) = \frac{mn}{B^2} \left( \frac{\partial \mathbf{E}_{\perp}}{\partial t} + \mathbf{v}_E \cdot \nabla \mathbf{E}_{\perp} \right) = \frac{1}{\mu_0 v_A^2} \left( \frac{\partial \mathbf{E}_{\perp}}{\partial t} + \mathbf{v}_E \cdot \nabla \mathbf{E}_{\perp} \right). \quad (2.11)$$

When using the full derivative form, the polarization current is

$$\mathbf{j}_P = \frac{1}{\mu_0 v_A^2} \frac{d\mathbf{E}_\perp}{dt} \quad (2.12)$$

This general expression is not applicable to the cases when the transverse scale size of the wave is comparable to the ion Larmor radius ( $\rho_i = \sqrt{T_e/m_i}/\omega_{ci}$ ). In such a case, the effective electric field controls the electric drift of the ion guiding center. This electric field is proportional to the electric field in the middle of the Larmour circle by a factor of  $I_0(s)e^{-s}$ . In this case  $I_0$  is a modified Bessel function, and  $s = (\rho_i k_\perp)^2$ . All of this was incorporated into the Fourier transform of the perpendicular current by *Cheng* [1991]:

$$\tilde{\mathbf{j}}_P = \frac{1}{\mu_0 v_A^2} \frac{1 - I_0(s)e^{-s}}{s} \frac{d\tilde{\mathbf{E}}_\perp}{dt}. \quad (2.13)$$

*Streltsov et al.* [1998b] showed that the Padé approximation ( $I_0(s)e^{-s}/s \approx 1/(1+s)$ ) works well for all of the  $s$  values and it can be used to obtain the inverse Fourier transform of the modified polarization current.

The Fourier transform of displacement current,  $\epsilon_0(1 - \rho_i^2 \nabla_\perp^2)^{-1} \frac{d\mathbf{E}_\perp}{dt}$ , is added to the obtained Fourier transform of the polarization current:

$$\tilde{\mathbf{j}}_\perp = \frac{1}{\mu_0 v_A^2} \frac{1}{1+s} \frac{d\tilde{\mathbf{E}}_\perp}{dt} + \epsilon_0 \frac{1}{1+s} \frac{\partial \tilde{\mathbf{E}}_\perp}{\partial t} = \frac{1}{(\mu_0(1+s))} \left( \frac{1}{v_A^2} \frac{d\tilde{\mathbf{E}}_\perp}{dt} + \frac{1}{c^2} \frac{\partial \mathbf{E}_\perp}{\partial t} \right). \quad (2.14)$$

Once this expression is plugged into the original current continuity expression (Eq. 2.6) and the inverse Fourier transform is performed, the following third governing

equation is obtained

$$(1 - \rho_i^2 \nabla_{\perp}^2) \boldsymbol{\nabla} \cdot j_{\parallel} \mathbf{b} + \frac{1}{\mu_0} \boldsymbol{\nabla} \cdot \left[ \left( \frac{1}{v_A^2} + \frac{1}{c^2} \right) \frac{\partial E_{\perp}}{\partial t} + \frac{1}{v_A^2} \mathbf{v}_{\mathbf{E}} \cdot \boldsymbol{\nabla} \mathbf{E}_{\perp} \right] = 0. \quad (2.15)$$

## 2.2 Numerical Implementation of the Magnetospheric Model

The equations introduced in the previous section need to be reformatted in order to be implemented numerically. The background magnetic field is oriented along the  $z$  direction,  $x$  indicates the latitudinal variation, and  $y$  specifies the longitudinal variation. The perturbed magnetic field component is expressed in terms of the vector potential  $\mathbf{b}_{\perp} = \nabla \times (A_{\parallel} \mathbf{z})$  and the perpendicular component of the electric field is  $\mathbf{E}_{\perp} = -\nabla_{\perp} \times \Phi$ . The parallel electric field component is calculated as

$$E_{\parallel} = -\mathbf{b} \cdot \boldsymbol{\nabla} \Phi - \frac{\partial A_{\parallel}}{\partial t}. \quad (2.16)$$

Partial derivatives in the direction parallel to the  $\mathbf{b}$  can be calculated in the following way

$$\nabla_{\parallel} = \mathbf{b} \cdot \nabla = \nabla_z + \frac{(\nabla A_{\parallel} \times \nabla)_z}{B_0}, \quad (2.17)$$

using which the parallel component of electric field becomes

$$E_{\parallel} = - \left( \nabla_z \Phi + \frac{(\nabla A_{\parallel} \times \nabla)_z}{B_0} \nabla \Phi \right) - \frac{\partial A_{\parallel}}{\partial t}. \quad (2.18)$$

It is assumed that the field aligned current is carried by electrons

$$j_{\parallel} = -env_{\parallel e} = \frac{1}{\mu_0} \nabla \times \mathbf{b}_{\perp} = -\frac{1}{\mu_0} \nabla_{\perp}^2 A_{\parallel}. \quad (2.19)$$

Using these equations, the three governing MHD equations (Eq.2.2, 2.4, and 2.15) can be rewritten in the dimensionless form as

$$\frac{\partial}{\partial t} (n_0 A_{\parallel} - \delta \nabla_{\perp}^2 A_{\parallel}) + \delta \nabla_{\perp}^2 A_{\parallel} \frac{d}{dz} \left( \frac{\nabla_{\perp}^2 A_{\parallel}}{n_0} \right) = \nabla_z \Phi + \nu_e \nabla_{\perp}^2 A_{\parallel}, \quad (2.20)$$

$$\frac{dn_1}{dt} = -B_0 \frac{d}{dz} \left( \frac{\nabla_{\perp}^2 A_{\parallel}}{B_0} \right), \quad (2.21)$$

and

$$\frac{\partial}{\partial t} \nabla \cdot \left( \left( \frac{1}{v_A^2} + \frac{1}{c^2} \right) \nabla_{\perp} \Phi \right) - \nabla \cdot \left[ \frac{1}{v_A^2} \mathbf{v}_E \cdot \nabla \mathbf{E}_{\perp} \right] = -B_0 \frac{d}{dz} \left( \frac{\nabla_{\perp}^2 A_{\parallel}}{B_0} \right). \quad (2.22)$$

Where

$$\delta = \frac{m_e B_{0*}^2}{m_i n_* T_{e*}}.$$

Normalization was performed similar to the work of *Chmyrev et al.* [1988]:

$$t_0 = t/\omega_{ci*}; l_{\perp 0} = \frac{c_{s*}}{\omega_{ci*}} l_{\perp}; l_{\parallel 0} = \frac{v_{A*}}{\omega_{ci*}} l_{\parallel}; T_{e0} = T_{e*} T_e;$$

$$\Phi_0 = \frac{T_{e*}}{e} \Phi; A_{\parallel 0} = \frac{T_{e*} c}{e v_{A*}} A_{\parallel}; n_0 = n_* n.$$

Here  $\omega_{ci*}$  is the ion cyclotron gyrofrequency and  $c_{s*}$  is the speed of sound.  $\omega_{ci*}$ ,  $c_{s*}$ ,  $v_{A*}$ ,  $T_{e*}$ ,  $n_*$  are constants that are estimated at the magnetospheric equator at a radial distance that is specific for each simulation. The normalized values used from

this point in the model will omit the subscript, 0, in order to keep the expressions in a more elegant form.

The three governing equations include derivatives that need to be defined explicitly in order for the simulation to work. The scale factors for the coordinate system used in the model can be converted from the spherical system and are defined as

$$h_x = \frac{r^3}{\sqrt{1 + 3\cos^2\theta}}, h_y = r \sin \theta, h_z = \frac{\sin^3\theta}{\sqrt{1 + 3\cos^2\theta}}. \quad (2.23)$$

Once the scaling factors are defined, the differential operators can be defined using these metric factors:

$$\frac{d}{dt} = \frac{\partial}{\partial t} + \frac{1}{B_0}\{\Phi, \dots\}, \quad (2.24)$$

$$\frac{d}{dz} = \frac{\partial}{h_z \partial z} - \frac{1}{B_0}\{A_{\parallel}, \dots\}, \quad (2.25)$$

$$\nabla_z = \frac{\partial}{h_z \partial z}, \quad (2.26)$$

$$\nabla_{\perp}^2 A_{\parallel} = \frac{1}{h_x h_y} \left[ \frac{\partial}{\partial x} \left( \frac{h_y \partial h_z A_{\parallel}}{h_x h_z \partial x} \right) + \frac{\partial}{\partial y} \left( \frac{h_x \partial h_z A_{\parallel}}{h_y h_z \partial y} \right) \right], \quad (2.27)$$

and

$$\nabla \cdot \left( \left( \frac{1}{v_A^2} + \frac{1}{c^2} \right) \nabla_{\perp} \Phi \right) = \frac{1}{h_x h_y h_z} \left[ \frac{\partial}{\partial x} \left( \frac{h_y h_z \partial \Phi}{(v_A^2 + c^2) h_x \partial x} \right) + \frac{\partial}{\partial y} \left( \frac{h_x h_z \partial \Phi}{(v_A^2 + c^2) h_y \partial y} \right) \right]. \quad (2.28)$$

The notation  $\{\alpha, \beta\}$  is introduced to simplify the expressions:

$$\{\alpha, \beta\} = \frac{1}{h_x h_y} \left( \frac{\partial \alpha \partial \beta}{\partial x \partial y} - \frac{\partial \alpha \partial \beta}{\partial y \partial x} \right). \quad (2.29)$$

The second term in Eq.2.22 can be approximated in the differential form in the

following way. Firstly, lets approximate the expression inside of the argument:

$$\begin{aligned}\mathbf{v}_E \cdot \nabla \mathbf{E}_\perp &= \frac{1}{B_0 h_x h_y} \left[ \frac{\partial \Phi}{\partial y} \frac{\partial}{\partial x} \left( \frac{\partial \Phi}{h_x \partial x} \right) - \frac{\partial \Phi}{\partial x} \frac{\partial}{\partial y} \left( \frac{\partial \Phi}{h_x \partial x} \right) \right] \mathbf{e}_x \\ &\quad + \frac{1}{B_0 h_x h_y} \left[ \frac{\partial \Phi}{\partial y} \frac{\partial}{\partial x} \left( \frac{\partial \Phi}{h_y \partial y} \right) - \frac{\partial \Phi}{\partial x} \frac{\partial}{\partial y} \left( \frac{\partial \Phi}{h_y \partial y} \right) \right] \mathbf{e}_y \\ &= -\frac{1}{B_0} \left\{ \Phi, \frac{\partial \Phi}{h_x \partial x} \right\} \mathbf{e}_x - \frac{1}{B_0} \left\{ \Phi, \frac{\partial \Phi}{h_y \partial y} \right\} \mathbf{e}_y = v_x \mathbf{e}_x + v_y \mathbf{e}_y.\end{aligned}\quad (2.30)$$

This expression can be placed back into the second term of the differential form of the ion momentum equation giving

$$\nabla \cdot \left[ \frac{1}{v_A^2} \mathbf{v}_E \cdot \nabla \mathbf{E}_\perp \right] = \frac{1}{h_x h_y h_z} \left( \frac{\partial}{\partial x} \left( \frac{h_y h_z}{h_x v_A^2} v_x \right) + \frac{\partial}{\partial x} \left( \frac{h_x h_z}{h_y v_A^2} v_y \right) \right). \quad (2.31)$$

## 2.3 Numerical Domain

The three dimensional numerical domain used in the model simulates the magnetic flux tube of the Earth's dipole magnetic field at high-latitudes. The flux tube is bounded by the ionosphere in the Northern and Southern Hemispheres. The latitudinal boundaries of the domain are formed by two L magnetic shells. The azimuthal size of the domain is defined by the parameter  $\phi$ . The domain is symmetrical with respect to the magnetospheric equator. The three governing equations defined in the previous section are implemented in the orthogonal dipole coordinates [*Cummings et al.*, 1969]:

$$L = r/\sin^2(\theta), \quad \mu = \cos(\theta)/r^2, \quad \phi = \phi. \quad (2.32)$$

Where  $r$  is the distance to the center of Earth that is normalized by  $R_E = 6371.2\text{km}$  and  $\theta$  is the polar angle. The unit vector  $\mathbf{L}$  is locally perpendicular to the magnetic

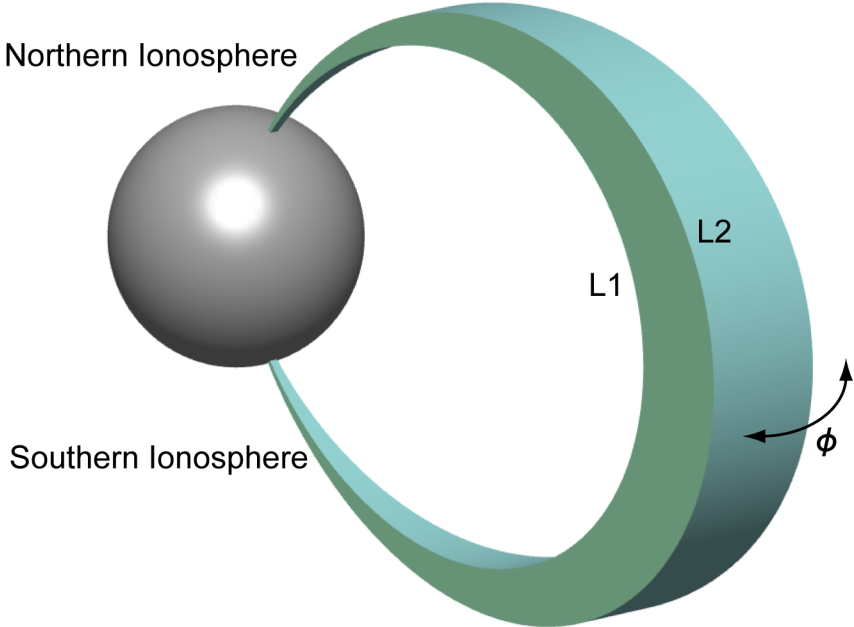


Figure 2.1: Schematic representation of the three-dimensional numerical domain used in the model. The domain approximates a magnetic flux tube that is bound on both sides by the Earth’s ionosphere. It is bounded by two L shells in latitude and extends longitudinally by  $\phi$  degrees.

shell and is in the  $x$  axis; and  $L$  has a constant value along a magnetic field line. The unit vector  $\mu$  is parallel to the local magnetic field,  $z$  axis, and  $\mu$  has a constant value along a line that is perpendicular to the magnetic field line. The unit vector  $\phi$  is locally eastward ( $y$  axis) and is perpendicular to the meridian lines and  $\phi$  measures a longitudinal angle. This setup takes into account the dipole geometry of the background magnetic field. The domain is illustrated in Figure 2.1.

Two dimensional computations are performed in the two-dimensional, axisymmetric ( $\partial/\partial\phi = 0$ ) domain consisting from two parts. One part is the dipole magnetic flux tube that extends from the ionosphere to the equatorial plane and the second part is a cylindrical extension attached to the dipole part in the equatorial plane.

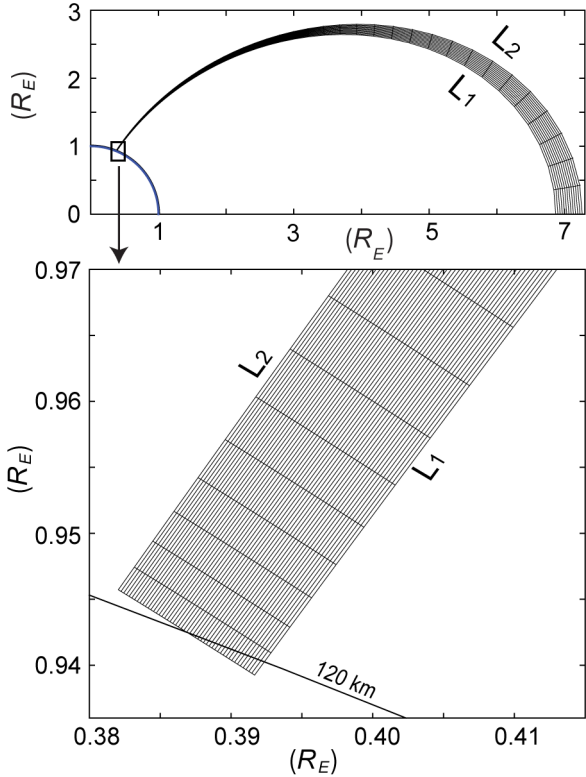


Figure 2.2: (Top.) The dipole part of the computational domain starting at 120 km altitude and ending at the equator. (Bottom.) The zoomed view of the part of the computational domain near the ionosphere. Only every 2<sup>nd</sup> parallel grid line is plotted in the figure.

It has a length of 30.3  $R_E$  and it is used as a “buffer” zone where the wave can propagate before/after it interacts with the ionosphere. The entire domain represents adequately extended in the magnetotail auroral flux tube in the night side magnetosphere. Simulations that require three-dimensions are implemented in a fully dipolar domain.

The computational grid in the dipole part of the domain has 101 steps in the  $L$  direction, 64 steps in the  $\phi$  direction, and 101 steps in the  $\mu$  direction. The grid is uniform in the  $L$  and  $\phi$  directions, and is strongly nonuniform in the  $\mu$  direction.

For example, when the distance between the adjacent nodes in the direction along  $\mathbf{B}_0$  is decreased by a factor of 50 from the equator to the ionosphere, the resulting grid is denser at low altitudes (grid size is 24 km) and is sparser in the equatorial magnetosphere (grid size is 1200 km). This approach allows the model resolve the spatio-temporal properties of the IFI interaction with the FACs in the ionospheric region. Figure 2.2 shows the two-dimensional view of the domain and the zoomed-in view of the ionospheric border of the domain.

## 2.4 Boundary Conditions

Boundary conditions play a very important role in the model. The ionospheric feedback instability is implemented through the usage of the BCs. The active ionospheric boundary conditions act as drivers and trigger the instability with a little perturbation, heating effect or with other driver configurations. These active ionospheric BCs are integrated with the magnetospheric model through the current continuity and density continuity equations.

The ionospheric boundary of the domain is set at an altitude of 120 km. At this altitude FACs change the ionospheric density in the conducting E-region of the ionosphere and the modified conductivity changes the dynamics of the FACs in return [*Trakhtengerts and Feldstein, 1991; Lysak, 1991; Pokhotelov et al., 2000; Streltsov, 2011; Jia and Streltsov, 2014*]. On the poleward-equatorward parts of the domain Dirichlet boundary conditions are implemented. Periodic BCs are set for azimuthal boundaries of the domain. Figure 2.3 schematically shows the BCs that are implemented in the model.

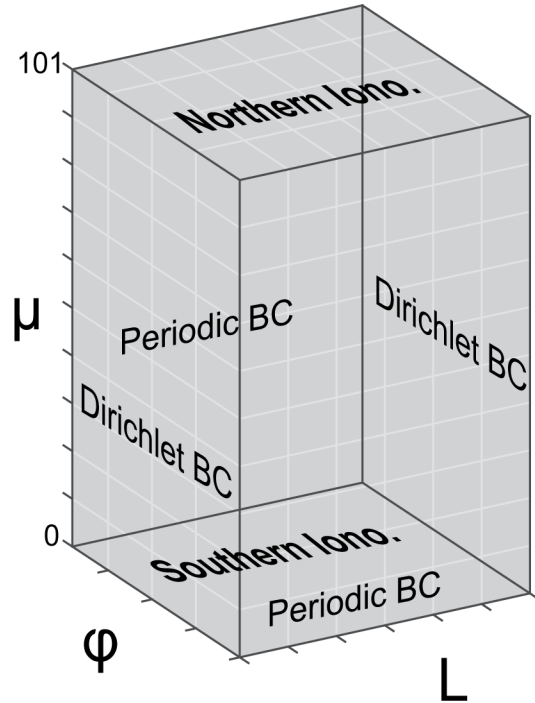


Figure 2.3: Schematic view of the boundary conditions (BC) implemented in the model. Both ionospheres have active boundary conditions. Periodic boundary conditions are applied on the E-W boundaries. Dirichlet boundary conditions are applied on the poleward-equatorward sides of the domain.

The current continuity in a general form is

$$\nabla \cdot \mathbf{j} = 0. \quad (2.33)$$

The simplification of treating the ionosphere as a conducting thin slab is justified by the results of study performed by *Lysak* [1991]. It was shown that the ionospheric current can be integrated by height, with an assumption that there is no current flowing between the ionosphere and neutral atmosphere. With this assumption, the current continuity equation can be modified as

$$\nabla_{\perp} \cdot \mathbf{j}_{\perp} = \pm j_{\parallel}. \quad (2.34)$$

This can be visualized as a field-aligned current flowing into the ionosphere, then flowing perpendicular to the magnetic field (as height integrated current  $\mathbf{j}_{\perp}$ ), and then leaving the ionosphere along a different field line. The sign “+” is used in the Southern Hemisphere, and the sign “−” is used in the Northern Hemisphere. The motion of ions and electrons in the ionosphere is affected by neutrals. Ohm’s Law give the following

$$J_{\perp} = \sigma_P \mathbf{E}_{\perp} - \sigma_H \frac{\mathbf{E}_{\perp} \times \mathbf{B}_0}{B_0} + j_{\parallel} \mathbf{b}. \quad (2.35)$$

In this equation  $\sigma_P$  is the Pedersen conductivity and the first term is the Pedersen current that is oriented along the perpendicular component of the background electric field. The second term is the Hall current term: it flows in the  $\mathbf{E} \times \mathbf{B}$  direction which is at an angle to the Pedersen current.  $\sigma_H$  is the Hall conductivity. The relationship between the plasma conductivity and collisions with the neutrals was investigated by *Kelley* [1989]:

$$\sigma_P = \sum_s \frac{n_s q_s^2}{m_s} \frac{f_s}{f_s^2 + \omega_{cs}^2}, \quad (2.36)$$

$$\sigma_H = - \sum_s \frac{n_s q_s^2}{m_s} \frac{\omega_{cs}}{f_s^2 + \omega_{cs}^2}. \quad (2.37)$$

In which  $n$ ,  $q$ ,  $m$ , and  $f$  define density, charge, mass, and neutral particle collision frequency, respectively, for each species  $s$  which have a gyrofrequency of  $\omega_{cs}$ . By integrating these plasma conductivities, the height integrated versions of them are obtained:

$$\Sigma_P = \int_{-h}^0 \sigma_P dz = neM_P h, \quad (2.38)$$

$$\Sigma_H = \int_{-h}^0 \sigma_H dz = neM_H h. \quad (2.39)$$

Here,  $h = 20$  km is the effective thickness of the E-region,  $M_P = 10^4$  m<sup>2</sup>/sV is the ion Pedersen mobility, and  $M_H$  is ion Hall mobility. The  $M_H$  parameter is proportional to the  $M_P$  [Brekke *et al.*, 1974]. In the model used in this study, the expression  $\Sigma_P = M_P n_E h e / \cos \lambda$  accounts for the tilt angle,  $\lambda$ , between the normal to the ionosphere and the central L-shell (average of the  $L_1$  and  $L_2$ ). By plugging back these expressions into the Eq.2.34, the following expression of the current continuity is obtained

$$\nabla_{\perp} \cdot (\Sigma_P \nabla_{\perp} \Phi) - \mathbf{b} \cdot \nabla_{\perp} \Sigma_H \times \nabla_{\perp} \Phi - \nabla_{\perp} \Sigma_H \cdot (\mathbf{b} \times \nabla_{\perp} \Phi) = \pm j_{\parallel}. \quad (2.40)$$

The effect of the displacement current,  $\epsilon_0 \partial \mathbf{E} / \partial t$ , is negligible in the ULF frequency range. So is the effect of the third term in the last equation as was shown in the study of *Kelley* [1989]. This reduces the current continuity to

$$\nabla_{\perp} \cdot (\Sigma_P \nabla_{\perp} \Phi) - \mathbf{b} \cdot \nabla_{\perp} \Sigma_H \times \nabla_{\perp} \Phi = \pm j_{\parallel}. \quad (2.41)$$

Using the scaling factors introduced previously, the current continuity in the ionosphere can be expressed mathematically as

$$\frac{1}{h_x h_y h_z} \left( \frac{\partial}{\partial x} \left( \frac{h_y h_z}{h_x} \Sigma_P \frac{\partial \Phi}{\partial x} \right) + \frac{\partial}{\partial y} \left( \frac{h_x h_z}{h_y} \Sigma_P \frac{\partial \Phi}{\partial y} \right) \right) + \{\Phi, \Sigma_H\} = \pm j_{\parallel}. \quad (2.42)$$

The other active boundary condition in the ionosphere is the density continuity

equation, in the form that was introduced by *Sato* [1978]:

$$\frac{\partial n}{\partial t} = \frac{j_{\parallel}}{e h} + \alpha(n_0^2 - n^2). \quad (2.43)$$

Where,  $n_0$  is the initial unperturbed height-integrated plasma density,  $\alpha = 3 \times 10^7$  cm<sup>3</sup>/s is the recombination rate showing the rate at which ions and electrons produce neutrals in the ionosphere. It was shown in a study by *Sato* [1978] that  $\alpha$  controls the growth rate of the IFI generated structures.

## 2.5 Background Parameters

The numerical model uses a dipolar background geomagnetic field model which has a form of

$$B_0 = B_* \frac{R_E^3}{r^3} \sqrt{(1 + 3 \sin^2 \theta)} nT \quad (2.44)$$

Here  $B_* = 31000$  nT,  $r$  is the geocentric distance measured in  $R_E = 6371.2$  km.

One of the most important parameters of the model is the initial plasma density distribution. It is modeled as

$$n_0(L, \mu, \phi) = n_{01}(L)n_{02}(\mu)n_{03}(\phi). \quad (2.45)$$

Here  $n_{01}(L)$  provides density distribution profile in the equatorward-poleward direction ( $L$ );  $n_{02}(\mu)$  gives the background plasma density profile along the central magnetic field line; and  $n_{03}(\phi)$  defines the plasma structure in the azimuthal direction. Density cavities defined by these functions were observed by FAST satellite at altitudes above 1000 km [*Chaston et al.*, 2002].

Plasma density profile along the  $\mathbf{B}$  is crucial for the confinement of the IFI generated ULF waves in the IAR. The sharp gradient in the Alfvén speed is modeled through the density along the magnetic field. The following relationship describes the background density along the central magnetic field line

$$n_{02} = \begin{cases} a_1(r - r_1) + a_2, & \text{if } r_1 < r < r_2 \\ b_1 e^{-20(r-r_2)} + b_2 r^{-4} + b_3, & \text{if } r > r_2. \end{cases} \quad (2.46)$$

Where  $r$  is the radial distance to the grid point,  $r_1 = 1 + 120/R_E$ , and  $r_2 = 1 + 320/R_E$ . The constants  $a_1$ ,  $a_2$ ,  $b_1$ ,  $b_2$ , and  $b_3$  are chosen to provide some specific values of the plasma density at the ionospheric E region (altitude of 120 km), F region (altitude of 320 km) and at the equatorial magnetosphere. Simulations show that the density in the ionospheric E and F regions are one of the main parameters of the model and the density in the equatorial magnetosphere is not so important for the development of the IFI inside the IAR. This value controls the value of the eigenfrequency of ULF waves in the global resonator. However, due to the high Alfvén speeds near the equator variation of the plasma density in that region does not affect results significantly.

In the model, the ionospheric density defines the structure of the ambient electric field of the entire numerical domain [Streltsov *et al.*, 2005, 2012]. In a case of a current-free equilibrium, structure of the ambient background electric field,  $E_{0\perp}$ , is defined by the ionospheric density. Due to the assumption that there is no constant parallel electric field present in the magnetosphere, the ionospheric electric field is mapped equipotentially along the background magnetic field in the magnetosphere.

Low-orbit satellites frequently observe density cavities in the vicinity of the bright

discrete auroral arcs [Aikio *et al.*, 2004]. Numerical studies have investigated the formation of these cavities [Streltsov and Karlsson, 2008]. The results suggest that the ponderomotive force, associated with the large-amplitude small-scale Alfvé waves, is responsible for the formation of these cavities. The variation of the ionospheric density is modeled by  $n_{01}(L)$  and  $n_{03}(\phi)$ :

$$n_{01}(L) = \frac{1 + \kappa}{2} + \frac{1 - \kappa}{2} \cos \frac{2\pi(L - L_0)}{L_2 - L_1}, \quad (2.47)$$

and

$$n_{03}(\phi) = 1 - \beta e^{-\gamma^2 r^2}. \quad (2.48)$$

Here  $\kappa$  defines the ratio between the density at the bottom of the cavity to the value at the edge of it. Value  $\kappa = 1$  would indicate a homogeneous plasma distribution in the ionosphere. The size of the cavity is controlled by the parameters  $L_1$  and  $L_2$ . Azimuthal variation of the plasma density is defined by parameters  $\beta$  and  $\gamma$  which control range and amplitude of the distribution, respectively.

Electron and ion temperatures are modeled as

$$T_e = \frac{T_{e*} n_*}{n_0}, \quad T_i = \frac{T_{i*} n_*}{n_0}. \quad (2.49)$$

Where  $T_{e*}$  and  $T_{i*}$  are electron and ion temperatures (in eV) at the magnetospheric equator, and  $n_*$  is the plasma density at the same location. Such an assumption satisfies equilibrium condition  $\nabla_z(n_0 T_e) = 0$ .

## 2.6 Numerical Algorithms

Partial differential equations that are present in the model are solved using a “predictor-corrector” approach to advance the solution in time. A third-order Adams-Bashforth (AB) method is used as a “predictor”, while the third-order Adams-Moulton (AM) method is used as a “corrector” [Burden and Faires, 1991]. The usage of this approach improves the accuracy and makes computations more efficient. At each time step predictor (AB) part of the algorithm calculates the new value of  $A_{\parallel}$  inside the magnetosphere. Using this new value in the corrector (AM) part,  $\Phi$  and  $n$  are updated.

The spatial derivatives are approximated using a centered finite-difference approach. This is due to the fact that the numerical domain is rectangular in geometry.  $\Phi$ ,  $n$  and  $A_{\parallel}$  values are located on nodes that are shifted by a half-step to allow a better resolution without increasing computational costs.  $\Phi$  and  $n$  grid points are split evenly along the  $\mu$  direction making 101 nodes along each magnetic field line and have end-nodes on both ionospheres. At the same time,  $A_{\parallel}$  has its points on a grid that is located in-between of the  $\Phi$  and  $n$  grid-points, making a total of 100 nodes along a magnetic field line. All of them share the same grid system in  $L$  and  $\phi$  directions.

Two Laplacians,  $\nabla_{\perp}^2 A_{\parallel}$  and  $\nabla \cdot \left[ \left( \frac{1}{v_A^2} + \frac{1}{c^2} \right) \nabla_{\perp} \Phi \right]$ , are solved to obtain new values for  $\Phi$  and  $A_{\parallel}$  at each time step. This is implemented by using a discrete Fourier transform in the azimuthal direction. The tridiagonal matrices that are formed in this operation are solved efficiently using a Thomas algorithm [Golub and Loan, 1996].

Active ionospheric boundary condition in the form of current continuity Eq.2.41 is solved to obtain a new value for the electric potential  $\Phi$  at each time steps as

well. This is a second-order convection-diffusion partial differential equation. Once discretized, this equation has five non-zero diagonal in the matrix. Each value of  $\Phi_{i,j}$  is related to its neighbors in a following way:

$$a_L \Phi_{i-1,j} + a_R \Phi_{i+1,j} + a_C \Phi_{i,j} + a_U \Phi_{i,j+1} + a_D \Phi_{i,j-1} = j_{\parallel i,j}. \quad (2.50)$$

Where coefficients in front of each  $\Phi$  value is defined using the metric factors:

$$a_L = \frac{1}{\Delta x^2} \left( \frac{h_y h_z}{h_x} \Sigma_P \right)_{i-1,j} \frac{1}{h_x h_y h_z}_{i,j} - \frac{\Sigma_{H_{i,j+1}} - \Sigma_{H_{i,j-1}}}{h_y \Delta y}, \quad (2.51)$$

$$a_R = \frac{1}{\Delta x^2} \left( \frac{h_y h_z}{h_x} \Sigma_P \right)_{i+1,j} \frac{1}{h_x h_y h_z}_{i,j} + \frac{\Sigma_{H_{i,j+1}} - \Sigma_{H_{i,j-1}}}{h_y \Delta y}, \quad (2.52)$$

$$a_U = \frac{\Sigma_{P_{i,j+1}}}{h_y^2 \Delta y^2} + \frac{\Sigma_{H_{i+1,j}} - \Sigma_{H_{i-1,j}}}{h_x \Delta x}, \quad (2.53)$$

$$a_D = \frac{\Sigma_{P_{i,j-1}}}{h_y^2 \Delta y^2} - \frac{\Sigma_{H_{i+1,j}} - \Sigma_{H_{i-1,j}}}{h_x \Delta x}, \quad (2.54)$$

$$a_C = -(a_L + a_R + a_U + a_D). \quad (2.55)$$

Depending on the model input parameters, the matrix may lose its diagonal dominance in a case when the right-hand side of the last expression becomes larger than the left-hand side. This may happen when  $\Sigma_H$  becomes larger than  $\Sigma_P$ . In order to account for that, the model implements a PETSc package to solve the current continuity equation in the ionosphere. This package contains a GMRES numerical technique that uses the MPI routines to speedup the solving algorithm [Balay *et al.*, 1997]. This PETSc package is implemented on the VEGA cluster and the model is adapted to run on its processors efficiently.

# Chapter 3

## 2D Model: Modeling of MICA Sounding Rocket Observations

*Results presented in this chapter are published in the Journal of Geophysical Research [Tulegenov and Streltsov, (2017), Ionospheric Alfvén resonator and aurora: Modeling of MICA observations, 122, 7530, doi:10.1002/2017JA024181].*

### 3.1 Introduction

Origin and dynamics of small-scale, intense electromagnetic waves with frequencies less than 1 Hz measured, by satellites and sounding rockets in the low-altitude magnetosphere and ionosphere, are questions under investigation in this chapter. The interest in these waves is motivated by their very important role in the electromagnetic coupling between the ionosphere and magnetosphere, particularly, in the high-latitude, auroral region. Among three modes of ultra-low-frequency (ULF) MHD waves, fast or compressible, intermediate or Alfvén, and slow, the small-scale Alfvén

waves are one of the most interesting from the point of view of the magnetosphere-ionosphere coupling. They carry magnetic field-aligned currents and fluxes of the electromagnetic energy from the magnetosphere to the ionosphere. This plays an important role in the exchange of mass, momentum and energy between the ionosphere and magnetosphere at high latitudes. In particular, these waves are responsible for the parallel electron acceleration [*Chaston et al.*, 2002], the heating of the ionosphere, the outflow of the ionospheric ions, and the formation of density disturbances in the ionospheric and magnetospheric plasmas.

A large number of observations performed on the ground [*Aikio et al.*, 2004], through low-orbiting satellites [*Karlsson and Marklund*, 1996; *Marklund et al.*, 1997; *Rother et al.*, 2007], and sounding rockets [*Cohen et al.*, 2013] demonstrate that the small-scale, very intense ULF waves are frequently observed in the vicinity of bright, discrete auroral arcs. This feature suggest that they are associated with a system of magnetic field-aligned currents causing auroras. Some studies suggest that these waves are generated by the magnetic field line resonance. This involves coupling between fast MHD waves and shear Alfvén waves in the equatorial magnetosphere and the formation of the standing pattern of the resonant Alfvén waves between the magnetically conjugate locations in the ionosphere. Other studies suggest that these waves are the result of the phase mixing of shear waves traveling towards the ionosphere from the magnetotail.

Currently one of the most promising hypotheses explaining origin of these waves is the ionospheric feedback instability (IFI) introduced by *Atkinson* [1970]. It occurs when the magnetic field-aligned currents (FACs) change the conductivity in the ionosphere by precipitating or removing electrons from it, causing the variations in the

conductivity to positively “feed back” on the structure and amplitude of the original FACs, increasing their magnitude. This mechanism had been extensively studied during last 40 years and these studies show that the favorable conditions for the IFI development include the low ionospheric conductivity and the large perpendicular electric field in the ionosphere [*Sato*, 1978; *Lysak and Song*, 2002]. Such conditions occur in the regions where downward FACs interact with the conducting E region of the ionosphere [*Doe et al.*, 1995; *Streltsov and Lotko*, 2004; *Paschmann et al.*, 2012].

Qualitatively, the feedback mechanism inside the IAR can be explained in terms of the “over reflection” of small-scale Alfvén waves in the presence of a large-scale electric field in the ionosphere [*Trakhtengertz and Feldstein*, 1984; *Trakhtengerts and Feldstein*, 1991; *Pokhotelov et al.*, 2001; *Lysak and Song*, 2002]. Over reflection means that the amplitude of the Alfvén wave reflected from ionosphere may be larger than the amplitude of the incident wave. That may occur when the field-aligned current in the small-scale wave enhances locally the ionospheric conductivity and thus reduces the Joule dissipation of the large-scale electric field in this location. The field energy is then released in the form of the magnetic field-aligned current propagating from the ionosphere and this contribution of this “additional” current makes the magnitude of the reflected current greater than the magnitude of the incident one. Therefore, multiple interactions of the same wave with the active ionosphere may lead to the increase of the wave amplitude.

To get several reflections from the ionosphere, the waves need to be trapped inside the resonator cavity in the magnetosphere with at least one of its boundaries sitting on the ionosphere. One such resonator is the ionospheric Alfvén resonator (IAR), which is a region in the low-altitude magnetosphere bounded by the conducting bottom of

the ionosphere (ionospheric E-region) and the strong gradient in the Alfvén speed at about 1 Re altitude [*Polyakov and Rapoport*, 1981]. It has eigenfrequencies between 0.1 Hz and 1 Hz [*Trakhtengerts and Feldstein*, 1987; *Lysak*, 1991; *Pokhotelov et al.*, 2000; *Hiraki and Watanabe*, 2011].

Generation of small-scale, intense shear Alfvén waves inside the IAR in the large-scale downward FAC adjacent to the upward FAC associated with the bright discrete auroral arc had been investigated numerically by *Streltsov and Lotko* [2004, 2008]; *Streltsov* [2011]. These studies made several quantitative predictions about the generation mechanism and spatiotemporal properties of these waves. To verify these predictions it was proposed to perform *in situ* measurements of the fields and particles in the vicinity of the discrete aurora by using a sounding rocket launched into the aurora to compare the experimental results with predictions from the numerical model developed by *Streltsov and Lotko* [2008]. Such a rocket experiment, called Magnetosphere-Ionosphere Coupling in the Alfvén Resonator (MICA), took place on 19 February 2012. This chapter presents results from the numerical simulations, confirming that the MICA rocket indeed detected small-scale, intense shear Alfvén waves generated by the IFI inside IAR. Parameters and location of these waves are in good, quantitative agreement with the ones predicted by the numerical model [*Streltsov and Lotko*, 2008].

## 3.2 MICA Data

The Magnetosphere-Ionosphere Coupling in the Alfvén Resonator sounding rocket was launched on 19 February 2012 05:41:06 UT from the Poker Flat Research Range,

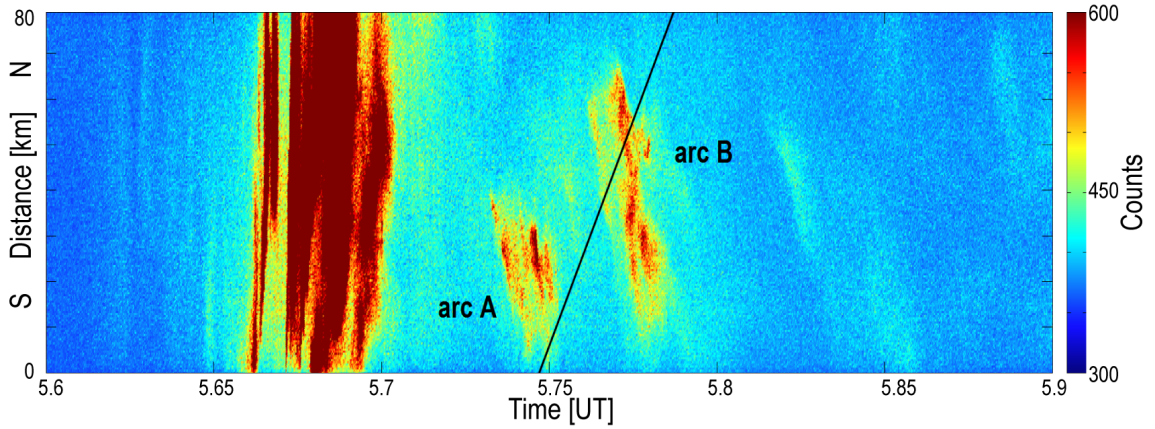


Figure 3.1: Venetie keogram shows the progress of MICA payload through the auroral arcs (adapted from *Lynch et al.* [2015]).

Alaska during active geomagnetic conditions. It reaches the apogee of 325.4 km after 297 seconds from the launch. The goal of the experiment was to measure parameters of the plasma and the electromagnetic field inside, or very close to, the bright discrete auroral arc. The payload, parameters of the flight, and geophysical conditions during the flight are described in detail in several recent papers [e.g., *Zettergren et al.*, 2014; *Lynch et al.*, 2015; *Fernandes et al.*, 2016; *Fisher et al.*, 2016]. The discussion of the experimental data is limited to only those which are directly relevant to the modeling efforts. In particular, all the experimental data used in this chapter are taken from *Lynch et al.* [2015].

During the flight the rocket went close to the discrete auroral arc (arc A) and then passed through another arc (arc B). Figure 3.1 shows the keogram from the Venetie camera of MICA’s progression through the arcs. Figure 3.2 shows an overview of the data measured by MICA. The electric field measurements were recorded from the Cornell University subpayload [*Lundberg et al.*, 2012a,b]. The in-situ electron density measurements were obtained from the Norwegian multineedle Langmuir probe

(mNLP) [Moen *et al.*, 2012]. The optical observations were obtained from the medium-field camera at Venetie. The magnetic field measurement were recorded using Billingsley fluxgate magnetometer (Billingsley TFM100G2).

The rocket passes close to arc A during the interval between 205 and 245 seconds from the launch. It then goes through arc B between 280 and 330 seconds as is seen in the visible auroral intensity at Venetie footprint in Figure 3.2 (fourth panel). After 330 seconds, the auroral activity shows a significant drop. The DC electric field components are shown in the first panel in the geomagnetic coordinate system. The second panel shows the DC magnetic field components that are deflected from IGRF. The cross product of the electric and magnetic field vectors in the form of Poynting flux is shown in the third panel. In the coordinate system used for the MICA data, the cross product of north and east is positive down. This means that magnetic field, Poynting flux and currents are positive pointing downward towards the earth. Comparison of the Poynting flux shown in the third panel in Figure 3.2 and the auroral luminosity shown in the forth panel demonstrates that: 1) no intense small-scale waves were detected by MICA when the rocket flew through the maximums of luminosity associated with arcs A and B; 2) intense small-scale electromagnetic structures had been observed near the edges of arcs A and B. The observed structures have periods of a few seconds, which suggests that these small-scale, large amplitude electromagnetic fluctuations are Alfvén waves trapped inside the IAR.

In this study the main focus is on the dynamics of small-scale FACs observed by the MICA rocket because they are the main participants of the magnetosphere-ionosphere interactions controlled by the IFI. The parallel current density is obtained as the curl of the measured magnetic field [Lynch *et al.*, 2015]. The results below

show the modeling of the small-scale, very intense FAC structures detected in the vicinity of both arcs.

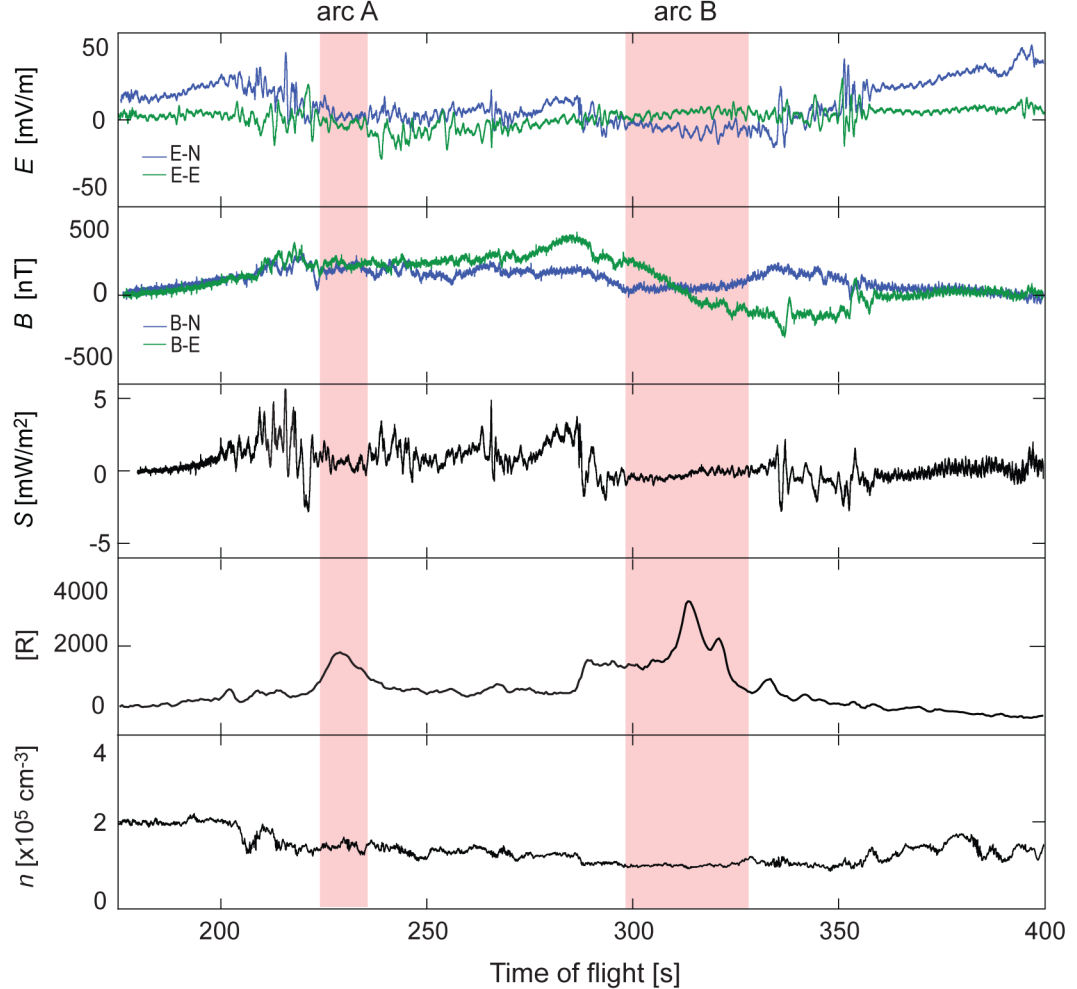


Figure 3.2: Overview of the MICA flight (adapted from *Lynch et al. [2015]*). The first panel shows electric field. The second shows magnetic field. The third panel shows the Poynting flux calculated from  $E$  and  $B$  fields (positive is downward). The fourth panel shows the optical intensity measured by the medium-field camera. And the fifth panel shows the plasma density measured by the mNLP probe.

### 3.3 Numerical Implementation and Boundary Conditions

Computations are performed in the two-dimensional, axisymmetric ( $\partial/\partial\phi = 0$ ) domain consisting from two parts. One part is the dipole magnetic flux tube that extends from the ionosphere to the equatorial plane and the second part is a cylindrical extension attached to the dipole part in the equatorial plane. It has a length of  $30.3 R_E$  and it is used as a “buffer” zone where the wave can propagate before/after it interacts with the ionosphere. The entire domain represents an adequate extension of the auroral flux tube in the night side magnetosphere.

In the model the background magnetic field is directed from the ionosphere, as is the case in the southern hemisphere. In such a configuration, the upward current which is pointed along the field is positive and the downward current is negative.

Figure 3.3 shows the dipole part of the domain used in the simulation of the Arc B event: the lateral boundaries of the domain are set at  $L = 6.87$  and  $L = 7.27$  magnetic shells. Only every  $2^{nd}$  parallel grid line is plotted in the figure. Figure 3.3 also shows, with a red line, the MICA rocket trajectory mapped into the computational domain using the 11<sup>th</sup> generation of the IGRF model [Finlay *et al.*, 2010].

In this study, fields and currents calculated by the model are compared with the corresponding quantities measured by the MICA rocket. The numerical data is interpolated on the trajectory of the virtual rocket “flying” through the computational domain with the velocity, along the trajectory, matching the corresponding parameters of the real rocket. This interpolation will be done both in time and space in order to match the time and location of the data obtained by the MICA rocket.

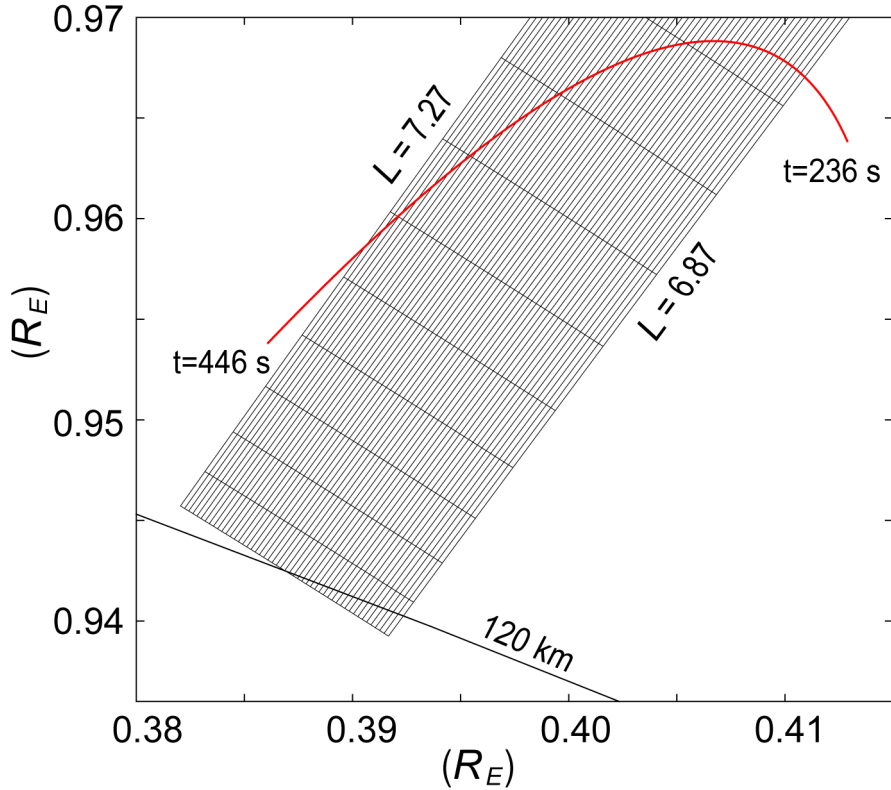


Figure 3.3: The zoomed view of the part of the computational domain near the ionosphere with the MICA trajectory on it. Adapted from *Tulegenov and Streltsov [2017]*.

The following relationship describes the background density profile along the central magnetic field line as (in the case of arc B event, the central magnetic field line is  $L = 7.07$ )

$$n_0 = \begin{cases} a_1(r - r_1) + a_2, & \text{if } r_1 < r < r_2 \\ b_1 e^{-20(r-r_2)} + b_2 r^{-4} + b_3, & \text{if } r > r_2. \end{cases} \quad (3.1)$$

Here  $r$  is the radial distance to the grid point where  $r_1 = 1 + 120/R_E$ , and  $r_2 = 1 + 320/R_E$ . The constants  $a_1$ ,  $a_2$ ,  $b_1$ ,  $b_2$ , and  $b_3$  are chosen to provide some specific values of the plasma density at the ionospheric E region (altitude of 120 km),

F region (altitude of 320 km) and at the equatorial magnetosphere.

Values of the coefficients in Eq. 3.1 were chosen from several test runs of simulations with the goal to reproduce dynamics, spatial structure and amplitude of the observed small-scale structures with the numerical results. For example, in the simulations of waves observed near the arc B, values of constants in Eq. 3.1 were chosen to provide  $n_E = 5.0 \times 10^4 \text{ cm}^{-3}$ ,  $n_F = 3.0 \times 10^5 \text{ cm}^{-3}$  and  $n_{eq} = 10 \text{ cm}^{-3}$ . These values are close to the density values observed by the MICA mNLP probe.

Simulations are started by specifying large-scale magnetic-field aligned currents on the magnetospheric boundary of the domain. Structure and amplitude of the magnetospheric currents define the dynamics of the small-scale FACs observed in the vicinity of arc A and arc B by the MICA rocket. Because the structure, location and dynamics of these small-scale FACs are different, the amplitude and structure of the large-scale magnetospheric currents driving IFI are different as well.

For example, optical observations show that the MICA rocket traversed arc B but did not traverse arc A. It only ‘‘touched’’ it near the edge, and to model the MICA rocket flight near the arc A, a full 3D model is needed. To model this passage of the rocket through the arc the 2D model is used and it is assumed that the rocket went through arc A. The MICA observations performed in the vicinity of arc A are modeled using a system of two downward and one upward FACs defined at the equatorial boundary of the domain as

$$j_{\parallel A} = j_A(t) \begin{cases} \cos(2\pi(l - 6.745)/\ell_A), & \text{if } |l - 6.745| \leq \ell_A/2 \\ 0, & \text{if } |l - 6.745| > \ell_A/2 \end{cases} \quad (3.2)$$

Here  $\ell_A = 0.4(6.88 - 6.61)$ ,  $L = 6.61$  and  $L = 6.88$  are the lateral boundaries

of the domain, and  $j_A(t)$  linearly increases from 0 to 120 nA/m<sup>2</sup> during the first 19 seconds of simulations, then remaining constant after that. This linear “ramp-phase” provides a gradual increase in the amplitude of the wave propagating from the equator toward the ionosphere.

The observations performed in the vicinity of arc B are modeled using one upward and one downward FACs defined on the equatorial boundary of the domain as

$$j_{\parallel B} = j_B(t) \begin{cases} \sin(2\pi(l - 7.07)/\ell_B), & \text{if } |l - 7.07| \leq \ell_B/2 \\ 0, & \text{if } |l - 7.07| > \ell_B/2 \end{cases} \quad (3.3)$$

Here  $\ell_B = 0.6(7.27 - 6.87)$ ,  $L = 6.87$  and  $L = 7.27$  are the lateral boundaries of the domain, and  $j_B(t)$  linearly increases from 0 to 50 nA/m<sup>2</sup> during the first 19 seconds of simulations and remains constant after that.

### 3.4 Results and Discussions

From the modelling studies of interactions between the system of large-scale magnetic field-aligned currents and the high-latitude ionosphere performed by *Streltsov and Lotko* [2004, 2008] and *Streltsov and Karlsson* [2008], it is known that the intense, small-scale structures first appear at the boundary between the upward and downward currents and propagate into the downward current channel. These dynamics are explained by the fact that these structures are generated by the strong gradients in the ionospheric plasma density caused by the precipitation/removal of electrons by FACs, and they propagate in the direction of the perpendicular electric field induced by the large-scale currents in the ionosphere. This field moves the ionospheric ions

across the magnetic field from the location where the electrons are removed by the downward FAC to the location where they are precipitated by the upward FAC. Therefore, the intense, small-scale currents produced by the IFI are expected to be observed in the downward current channels adjacent to the upward current channel associated with the strong electron precipitation causing discrete auroral arcs.

In application to the small-scale structures observed near arc A and arc B, this simple physical picture of the development of the ionospheric feedback instability provides some insight on the structure of large-scale currents driven the instability. In particular, the small-scale structures have been observed on both edges of arc A and only on one edge of arc B. These features suggest that the small-scale currents observed near arc A are the result of interactions between the ionosphere with the system of two large-scale downward and one upward FACs (given by Eq. 3.2) and the small-scale waves observed near the B, which are the result of interactions between the ionosphere and one downward and one upward FACs (given by Eq. 3.3).

Numerical results of modeling small-scale structures observed near arc B is done first. Figure 3.4 shows six snapshots of  $j_{\parallel}$  obtained from the simulations at time  $t = 370, 400, 430, 480, 530$ , and  $580$  s. Trajectory of the MICA rocket is plotted in each panel for reference. These snapshots show that the pair of upward and downward currents with an amplitude of  $9 \mu\text{A}/\text{m}^2$  reach the ionosphere from the magnetospheric boundary at  $t = 370$  s. The currents increase in amplitude in the next 8-10 s and the ionospheric feedback instability starts to produce small scale currents at the boundary between the two large-scale FACs. The instability starts to grow in size and propagate along the downward current region. At time  $t = 390$  s the amplitudes of small-scale currents start to saturate at the value of  $273 \mu\text{A}/\text{m}^2$ . Panels corresponding to  $t = 480$ ,

530, and 580 s illustrate how the small-scale structures “populate” the downward current channel as time proceeds.

Figure 3.5 shows a snapshot of  $j_{\parallel}$  from the same simulation taken at  $t = 600$  s at the entire dipole part of the domain: from the ionosphere to the altitude (or the length along the  $L = 7.07$  magnetic field line) of  $5 \times 10^4$  km. The profile of the Alfvén speed is shown in the figure with a solid black line. The figure confirms that the small-scale currents are indeed trapped between the ionosphere and the sharp gradient in the Alfvén speed, which provides the upper boundary of the ionospheric Alfvén resonator.

The linear theory postulates that the ionospheric feedback instability occurs when  $u_d k_{\perp} > \omega$ , where  $u_d = M_P E_{\perp}$  is the ion drift velocity in the ionosphere,  $k_{\perp}$  is the perpendicular wavenumber, and  $\omega$  is the angular wave frequency [Trakhtengertz and Feldstein, 1984; Trakhtengertz and Feldstein, 1991; Lysak and Song, 2002]. In the simulations illustrated in Figure 3.4 these parameters at  $t = 400$  s are  $k_{\perp} = 2\pi/2.25 \times 10^{-3}$  m $^{-1}$ ,  $E_{\perp} = 128$  mV/m, and  $\omega = 2\pi 0.39$  s $^{-1}$ . Once these parameters are plugged into the threshold inequality, it can be noticed that the necessary condition is satisfied with  $128$  mV/m  $> 87.7$  mV/m.

The ionospheric feedback instability in the ionospheric Alfvén resonator also can be characterized by the growth rate. An analytical expression for the linear growth rate  $\gamma$  is derived by Lysak [1991] and Pokhotelov *et al.* [2000, 2001] as  $\gamma_L = \sqrt{\alpha_P \eta_{1m}/2}$ , where  $\alpha_P = \Sigma_P \mu_0 V_{AI}$ ,  $V_{AI} = 1214$  km/s is the Alfvén speed in the resonator, and  $\eta_{1m}$  is the root of  $J_1(\eta) = 0$ . The first three roots of  $J_1(\eta)$  are 0, 3.8, and 7. At time  $t = 400$  s  $\gamma_{simulation} = 1.58$ , and  $\Sigma_P = 0.383$  mho gives a  $\gamma_L = 1.43$ . This confirms that the ionospheric feedback instability generates small-scale structures inside the

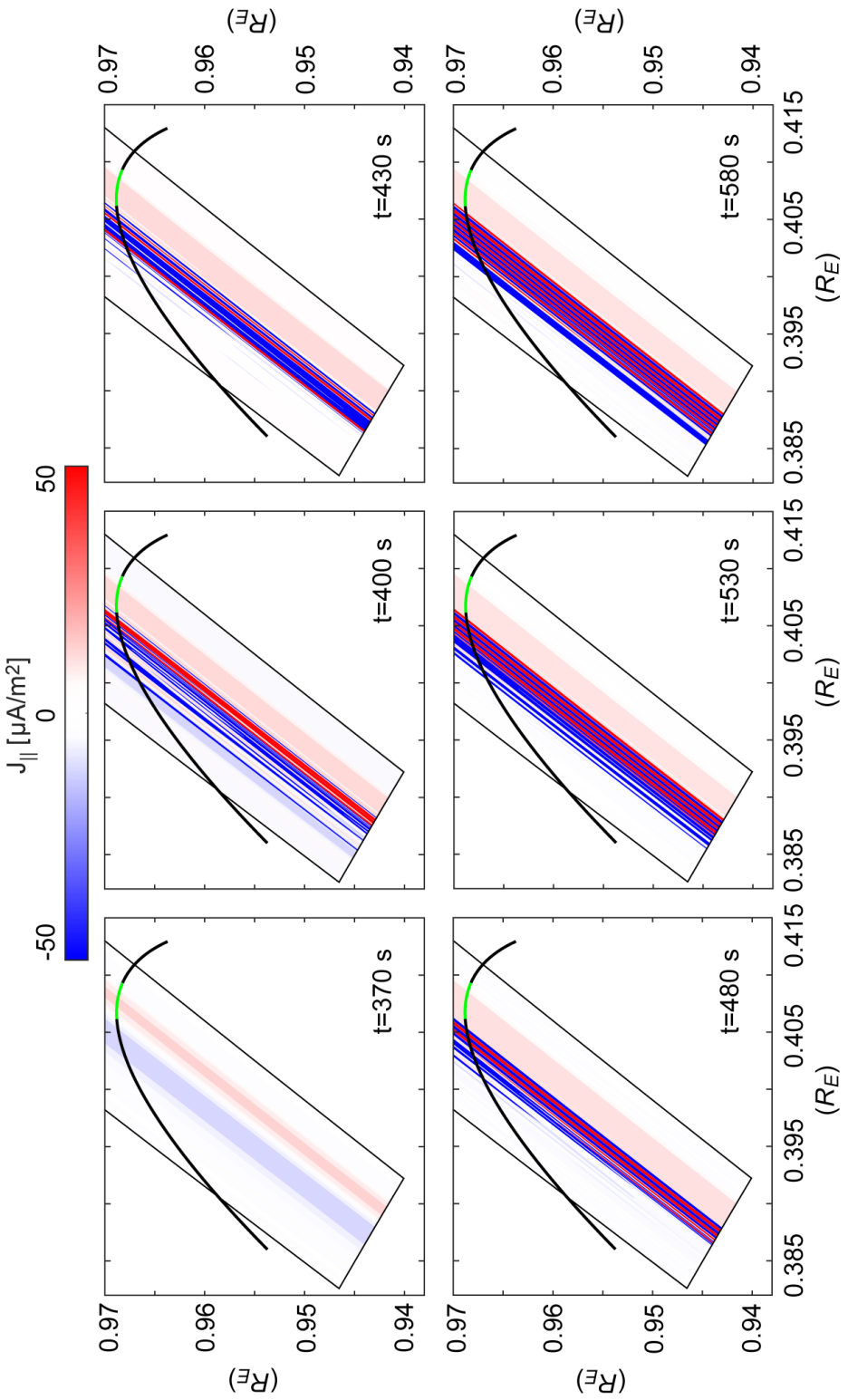


Figure 3.4: Dynamics of the ionospheric feedback instability caused by the pair of downward and upward FACs associated with the arc B. Adapted from Tulegenov and Streltsov [2017].

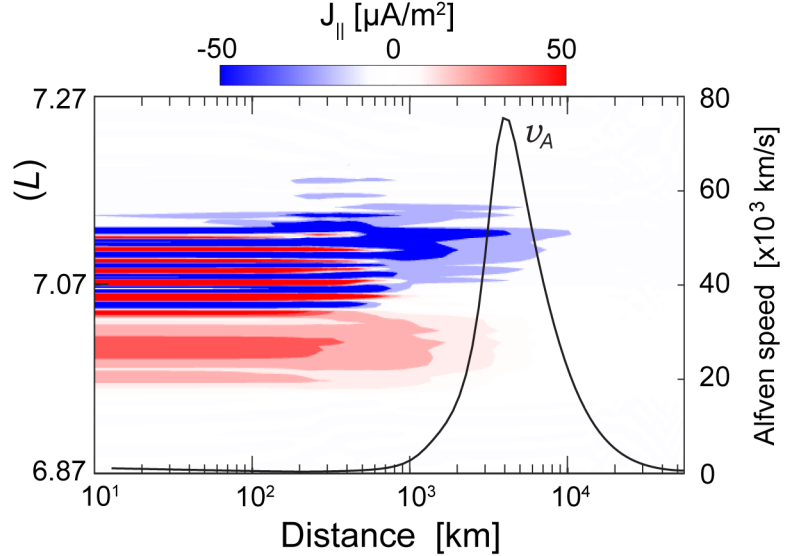


Figure 3.5: ULF current density structures generated in the IAR in the downward channel at  $t = 600$  s. The red color corresponds to the upward currents and the blue color corresponds to the downward currents. The Alfvén speed profile shown with a black line. Adapted from *Tulegenov and Strelets [2017]*.

IAR. To make a quantitative, detailed, comparison between numerical results and the MICA observations, the simulated data had been interpolated in space and in time onto the rocket trajectory mapped onto the computational domain. In other word, a “virtual” MICA rocket had been launched into the simulation domain with the parameters (velocity and location) matching the parameters of the real rocket. Figure 3.6 shows the comparison between the fine-scale density of FACs calculated from the curl of the MICA magnetic field data [*Lynch et al., 2015*] and the parallel current density measured by the virtual MICA “flying” through the simulations. The pink box in this figure marks the location/time of arc B. The fine-scale MICA current density measurements have a moving window average width of 1.6 s.

To make the comparison between the numerical results and the observations more quantitative, the power spectral density (PSD) of the parallel current density is cal-

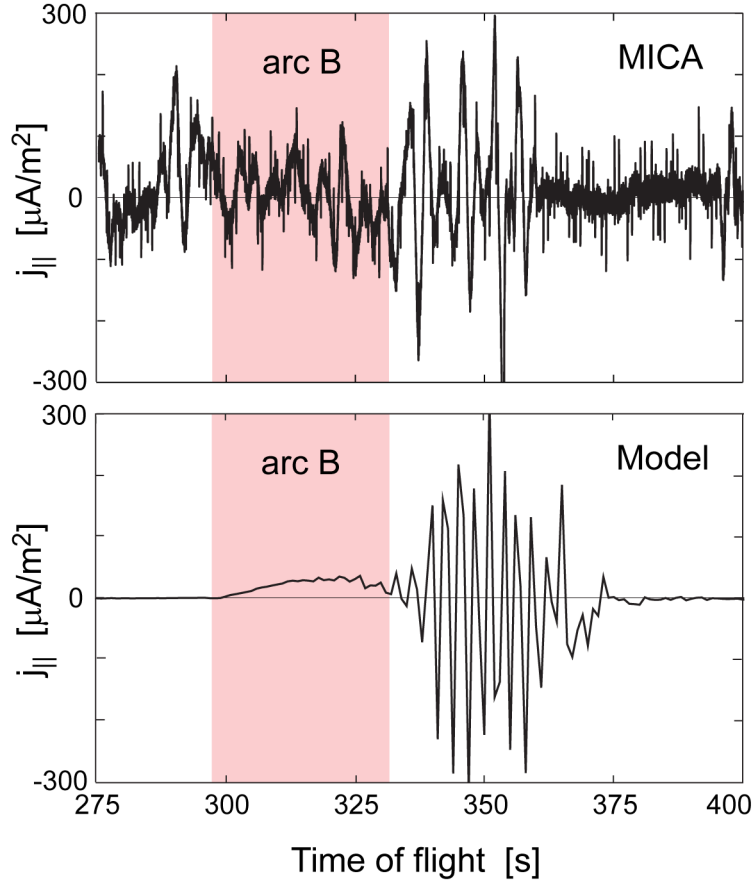


Figure 3.6: (Top.) Parallel current density derived from the magnetic field measurements performed by the MICA rocket (adapted from *Lynch et al. [2015]*). The fine-scaled current density is smoothed using unweighted moving average with a window of 1.6 s. (Bottom.) The parallel current density along the trajectory of the virtual MICA rocket "flying" through the simulations. The shaded area corresponds to rocket going through the auroral arc B. Adapted from *Tulegenov and Streltsov [2017]*.

culated for both the model and experimental output. The current is obtained from the magnetic field detected by the MICA rocket and from the magnetic field obtained in the simulations. These PSDs are shown in the right panel in Figure 3.7. It shows that most of the power in the simulated signal is in the frequency range from 0.30 Hz to 0.45 Hz, which are typical values for the eigenfrequencies of IAR at high latitudes

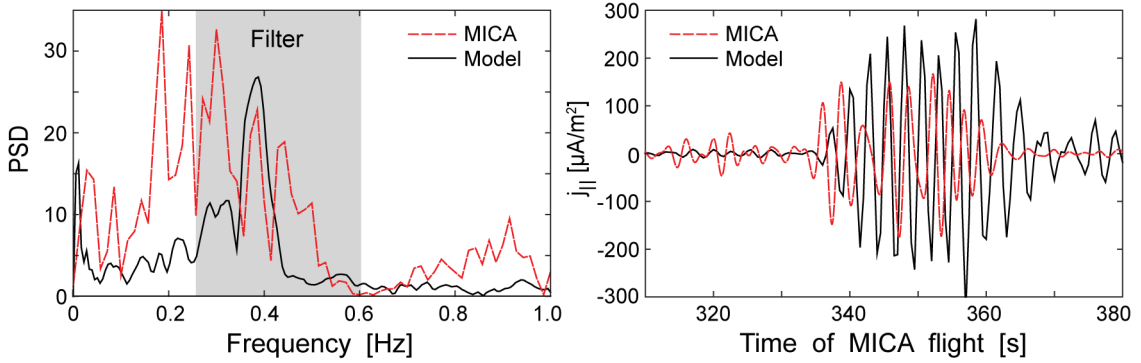


Figure 3.7: Left panel shows the power spectral density (PSD) of  $j_{\parallel}$  measured by the MICA rocket near the arc B (dashed red line) and the PSD of  $j_{\parallel}$  "measured" by the virtual MICA rocket in the corresponding simulation (solid black line). Right panel shows both  $j_{\parallel}$  in the time domain after filtering them with a bandpass filter with a passing frequency range from 0.25 Hz to 0.60 Hz. Adapted from *Tulegenov and Streltsov [2017]*.

[e.g. *Streltsov and Lotko, 2008*]. It should be mentioned here that the model produces and maintains stable, intense, small-scale current structures inside the IAR through 800 s of simulation.

MICA signal has most of its power in the frequency range from 0.18 Hz to 0.50 Hz and the peak of PSD of MICA data matches the peak in PSD of simulated data at 0.38 Hz. The fact that the PSD of the MICA data is broader than PSD of the simulated currents is quite normal, because the MICA signal contains contributions from many different physical processes occurring in the real space environment which are not included in the reduced MHD model implemented here. To make a better comparison between measured and simulated currents, both signals shown in Figure 3.6 had been filtered by the bandpass filter in the frequency range from 0.25 Hz to 0.60 Hz (This interval is marked in the left frame in Figure 3.7 with the gray rectangle). The right panel in Figure 3.7 shows the filtered MICA signal with a red, dashed line and the filtered signal from the simulation with a solid black line. Comparison

between two plots shown in the right panel in Figure 3.7 confirms that the physical model presented in this paper produces a reasonable agreement in spatial structure, dynamics and amplitude between the numerical results and MICA data related to arc B.

Simulations had also been performed with the goal to model small-scale currents observed by MICA near arc A. The main difference between these structures and the ones observed near arc B is that they occur on both edges of the upward current channel associated with the arc. In this case the system of two downward and one upward currents given by Eq. 3.3 had been used to drive the instability. The two downward channels can be easily recognized in the observations by the presence of intense small-scale current structures in them. The amplitude and the spatial sizes of the driver and the computational domain are given previously in this chapter. The virtual rocket had been flown through the simulations along the trajectory of the real rocket mapped into the simulation domain. The simulated parallel current density had been compared with the parallel current density calculated from MICA data that was obtained by *Lynch et al.* [2015]. One of the main parameters affecting this comparison is the moment of time when the virtual rocket was “launched” into the simulation.

The best case comparison between the numerical results and observations related to arc A is shown in Figure 3.8. There, the simulated parallel current density is shown with the solid black line and the one obtained from the observations is shown with a dashed red line. Both signals had been filtered with the bandpass filter in a frequency range from 0.20 Hz to 0.70 Hz. Figure 3.8 again demonstrates a good, quantitative agreement between the numerical results and the results derived from the observa-

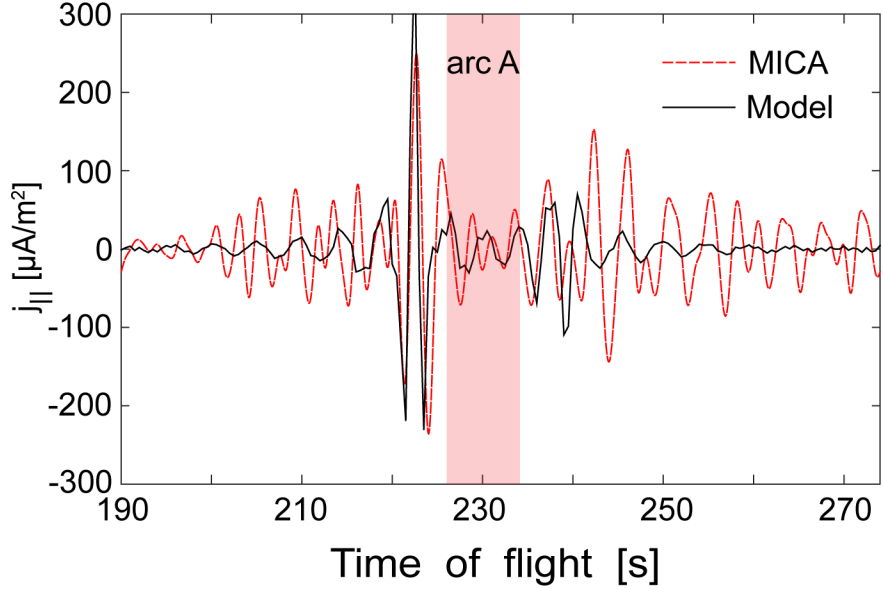


Figure 3.8: The parallel current density measured by the MICA rocket near the arc A (dashed, red line) and the parallel current density "measured" by the virtual MICA rocket in the corresponding simulations (solid black line). Both  $j_{\parallel}$  are filtered with a bandpass filter with a passing frequency range from 0.20 Hz to 0.70 Hz. Adapted from *Tulegenov and Streltsov [2017]*.

tions. After a good quantitative agreement between measured and simulated current densities has been achieved, a comparison between the electric and magnetic fields is done next. The top panel in Figure 3.9 shows the two components of the measured electric field and the perpendicular component of electric field from the simulation. The bottom panel shows the two components of the measured magnetic field and the perpendicular component of magnetic field from the simulation. The same bandpass filter had been applied to the model output. Qualitatively, the observed and the simulated fields are in a good agreement with each other, although they are not identical. One of the main reasons for the differences between measured and simulated results is that the measurements had been performed on the spinning payload flying through the 3D structures. So the electric and the magnetic fields detected by MICA have

two perpendicular components. The simulated fields have only one perpendicular component because they are obtained from the 2D model. Obviously, this fact will lead to the difference between how these fields obtained in simulations and measured on the rocket should look like in the time domain. However, the spectral properties of these fields (frequencies and wave numbers) will be close to each other, as it was demonstrated in the case of the parallel current density.

### 3.5 Chapter Conclusion

The results from the modeling study of small-scale, intense current structures observed by the MICA sounding rocket in the close vicinity of discrete auroral arcs are presented in this chapter and in the associated paper *Tulegenov and Streltsov* [2017]. The goal of this study was to verify the hypothesis given by *Streltsov and Lotko* [2008], that the small-scale large amplitude structures can be generated by the ionospheric feedback instability driven by a system of large-scale magnetic field-aligned currents interacting with the ionosphere. This hypothesis also predicts that the small-scale current structures should be observed on the boundaries between upward and downward currents and inside populate the downward current channels adjacent to the bright discrete auroral arcs.

Simulations of the reduced 2D MHD model derived in the dipole magnetic field geometry with the background parameters matching the MICA sounding rocket in-situ observations confirm this hypothesis. In particular, results from simulations reproduce spatial structure, frequency, and amplitude of the small-scale, intense magnetic field-aligned currents observed by MICA rocket at the edges of two bright, discrete

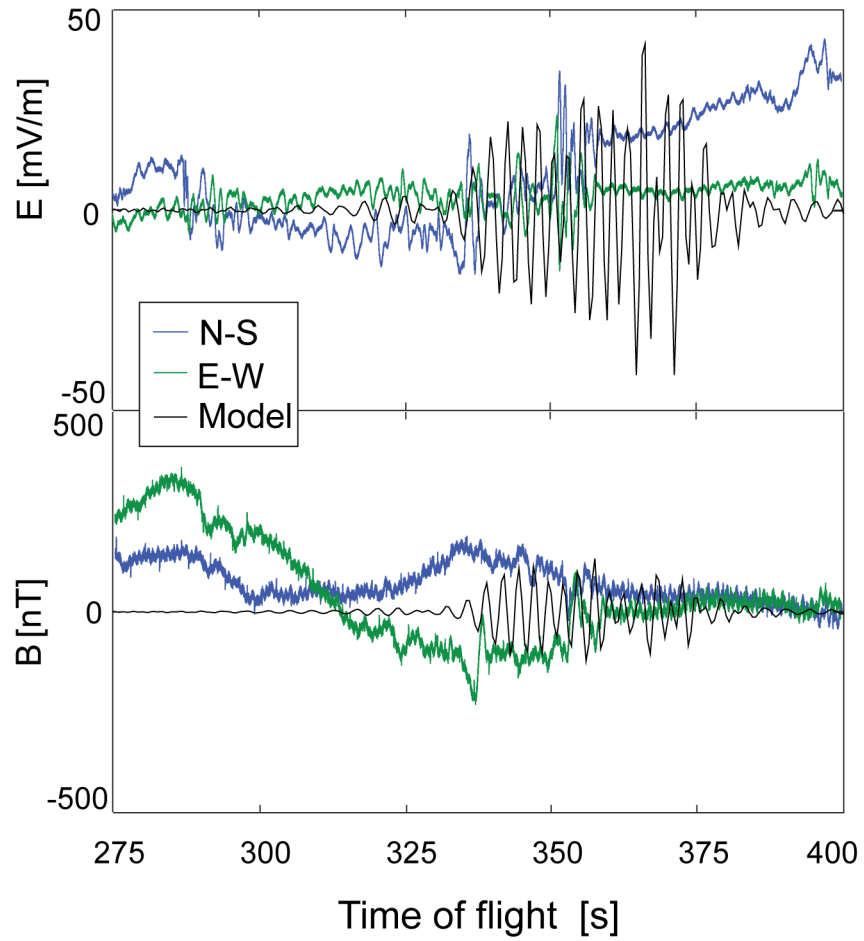


Figure 3.9: (Top.) In-situ electric fields in geomagnetic coordinates in blue and green (adapted from *Lynch et al. [2015]*). Black corresponds to the perpendicular component of the electric field from the simulations. The model output is filtered with a bandpass filter with a passing frequency range from 0.25 Hz to 0.60 Hz. (Bottom.) In-situ magnetic fields in geomagnetic coordinates in blue and green (adapted from *Lynch et al. [2015]*). Black corresponds to the perpendicular component of the magnetic field from the simulations. The model output is filtered with a bandpass filter with a passing frequency range from 0.25 Hz to 0.60 Hz. Adapted from *Tulegenov and Streltsov [2017]*.

auroral arcs.

Simulations also demonstrate that the important condition for the existence of a periodic system of small-scale FACs with an amplitude  $> 100 \mu\text{A}/\text{m}^2$  is the trapping

of these currents inside the ionospheric Alfven resonator. Parameters of the plasma inside the resonator (in particular, the magnitude of the plasma density inside the ionospheric E and F regions) together with the amplitude of the large-scale currents producing the aurora and driving the instability define spatiotemporal features of small-scale currents. In conclusion, simulations presented in this chapter confirm that the MICA project achieved the scientific goals formulated in their proposal. It is a significant contribution in the experimental verification of the importance of the ionospheric feedback instability for the generation of large-amplitude small-scale structures inside the ionospheric Alfven resonator in the auroral zone.

# Chapter 4

## 3D Model: Artificial Aurora

*Results presented in this chapter are published in the Journal of Geophysical Research [Tulegenov et al., (2019), Artificial aurora produced by HAARP, 124, doi:10.1029/2019JA026607].*

### 4.1 Introduction

Experiments involving ionospheric heating with high-frequency (HF) electromagnetic waves have been conducted on several heating facilities in Europe, Russia, and the USA for more than 60 years. They demonstrate many interesting linear and nonlinear effects observed on the ground, in the ionosphere, and in the magnetosphere of the Earth. Comprehensive reviews of these experiments and their results are given by Gurevich [2007] and Streltsov et al. [2018].

One particular direction of these experiments is a generation of artificial luminous structures in the ionosphere. Actually, the creation of an artificial luminosity was the main goal of one of the first heating facilities constructed in the Soviet Union

in 1961 [Gurevich, 2007]. A comprehensive review of early experiments focusing on an excitation of optical emissions at the EISCAT and HAARP facilities is given by *Kosch et al.* [2007].

In general, the heating can be conducted with O-mode or X-mode waves. The more frequently used is the O-mode heating. Usually, the frequency of the O-mode pump-wave is chosen close to the maximum frequency of the F2 ionospheric region, and the electrons in this region are energized via an anomalous absorption mechanism. This is a “local” heating, and all the effects observed in this case are produced by the increase in the electron temperature at this altitude. This heating can create various luminous structures (in particular, rings and solid spots) [*Bernhardt et al.*, 1988, 1989; *Pedersen et al.*, 2009] and artificial ionization layers, which have been studied by *Mishin et al.* [2004, 2005, 2016]; *Kosch et al.* [2005]; *Pedersen et al.* [2010].

Another approach to the ionospheric modification is the heating with X-mode HF waves. The X-mode HF waves can interact with the electrons through the cyclotron resonance, and this heating is used to change the temperature of the bulk population of electrons in the ionospheric D and E regions. The variations in the electron temperature change the Hall and Pedersen conductances in the ionosphere. And if there is an electric field in the ionosphere, then the changes in the conductances cause changes in the Hall and Pedersen currents flowing in the ionosphere, which, in turn, generate magnetic field-aligned currents (FACs) flowing into the magnetosphere. This is a so-called Getmantsev’s effect [*Getmantsev et al.*, 1974], which was introduced in 1974 and extensively used after that for the generation of ULF and VLF waves in the high-latitude ionosphere-magnetosphere system. The auroral and subauroral zones are particularly favorable for this mechanism because, normally, there is a large-

scale electric field in the ionosphere associated with the electrojet [Gurevich, 2011; Stubbe and Kopka, 1977; Stubbe *et al.*, 1981; Robinson *et al.*, 1998]. The injection of ELF/VLF waves into the magnetosphere via modulated heating of the electrojet by HAARP has been extensively studied by Papadopoulos *et al.* [2003], Golkowski *et al.* [2008]; Golkowski *et al.* [2011], and Cohen *et al.* [2010].

If the frequency of the ULF wave generated with heating matches one of the eigenfrequencies of the global magnetospheric resonator, then this wave can form a standing pattern along the magnetic field line between the conjugate hemispheres. In this case, a large-amplitude ULF wave can be generated by a relatively small ionospheric disturbance modulated with the eigenfrequency of the resonator e.g., [Streltsov *et al.*, 2005]. The large-amplitude ULF Alfvén waves may have a parallel electric field due to kinetic or inertial wave dispersion [Hasegawa, 1976; Goertz and Boswell, 1979], anomalous resistivity [Mozer, 2011], plasma turbulence [Jasperse *et al.*, 2010], mirror force [Nakamura, 2000], etc. This electric field can accelerate electrons along an ambient magnetic field into the ionosphere and cause bright, discrete auroral forms. The causal connection between magnetic field-aligned currents carried by shear Alfvén waves and natural luminous auroral structures has been convincingly demonstrated in many studies reviewed by Stasiewicz *et al.* [2000]. At the same time, there are still not many successful experiments reported in the literature, where the heating of the ionosphere with X-mode waves simultaneously produces disturbances in the magnetic field and the artificial airglow. This study reproduces with 3D MHD simulations results from one of the first successful experiments devoted to this problem.

## 4.2 The HAARP Heating Experiment

The experiment was conducted at HAARP on March 12, 2013 from 06:45 to 08:00 UT (corresponding to March 11, 2013, 22:45-24:00 Alaskan Daylight Time). During the experiment, HAARP transmitted X-mode electromagnetic waves with a frequency of 4.57 MHz in the direction of the local magnetic zenith (or in the direction of the ambient magnetic field). It has been shown in many studies, e.g., [Rietveld *et al.*, 2003; Honary *et al.*, 2011; Streltsov *et al.*, 2018], that heating in the magnetic zenith is the most efficient for changing the electron temperature in the ionosphere. The size of the heated spot at the altitude of 120 km for the 3 dB beamwidth of 4.57 MHz vertical beam is  $\approx 20\text{km}$ . The spot does not change its location during the entire experiment. The total power of the HAARP transmitter was 3.6 MW. The effective radiated power (ERP) of the transmitter is 1023 MW for the 4.57 MHz wave. The change in the beam direction from vertical to the MZ ( $\approx 14.4^\circ$  at HAARP magnetic latitude) may cause insignificant ( $\approx 3\%$ ) change in the size of the heating spot in the ionosphere and small variation in the ERP.

The HF signal has been modulated with a 0.9 mHz (556 s ON/OFF) frequency. This frequency was chosen from the observations of large-amplitude ULF waves detected with the fluxgate magnetometer in Gakona, Alaska, during several experimental campaigns at HAARP in the years 2011-2013 [Guido *et al.*, 2014]. These observations frequently demonstrate waves with frequencies of 0.75 mHz and 0.9 mHz during the periods of strong geomagnetic disturbances. These frequencies are at the low end of the so-called “magic” frequencies, sometimes attributed to shear Alfvén waves standing inside the global magnetic field resonator [Samson *et al.*, 1992; Fenrich *et al.*, 1995].

During the experiment, three components of the magnetic field have been measured with the HAARP fluxgate magnetometer in Gakona. The blue line in Figure 4.1a shows the D-component of the magnetic field, measured by the fluxgate magnetometer in Gakona on March 12, 2013 from 05:30 to 09:30 UT. The black line in Figure 4.1a shows the low-frequency ( $< 0.7$  mHz) part of the signal, and Figure 4.1b shows the high frequency ( $> 0.7$  mHz) part. The vertical red lines in Figures 4.1a and 4.1b mark the time of the beginning and the ending of the experiment. The time when the transmitter was ON is marked with pink boxes in Figure 4.1b.

Figure 4.1c shows the power spectral density (PSD) of the signal shown in Figure 4.1b in the frequency range from 0 to 5 mHz. Figure 4.1c shows that the main power of the signal is in the frequency of modulation 0.9 mHz, and Figure 4.1b shows very good correlation in phase and frequency between the periodicity of the heater's ON/OFF intervals and the oscillations of the magnetic field measured on the ground. The H-component of the magnetic field measured by the magnetometer during this time interval also reveals oscillations with the frequency of 0.9 mHz (not shown in the paper). These results suggest that X-mode heating indeed generates ULF waves and magnetic field-aligned currents, as was previously suggested by *Blagoveshchenskaya et al.* [2001] and *Streltsov et al.* [2012].

Figure 4.2 shows three sets of 630.0 nm optical images taken during the experiment by the HAARP telescope. The telescope can take images in 427.8 nm, 557.7 nm, 630.0 nm, and 777.4 nm wavelengths. The first set of images was taken during the time interval 06:45:00 - 06:54:15 UT, when the heater was ON. This set contains images with a bright luminous spot in the center. The second set of images was taken during time interval 06:54:15 - 07:03:31 UT, when the heater was turned OFF and no

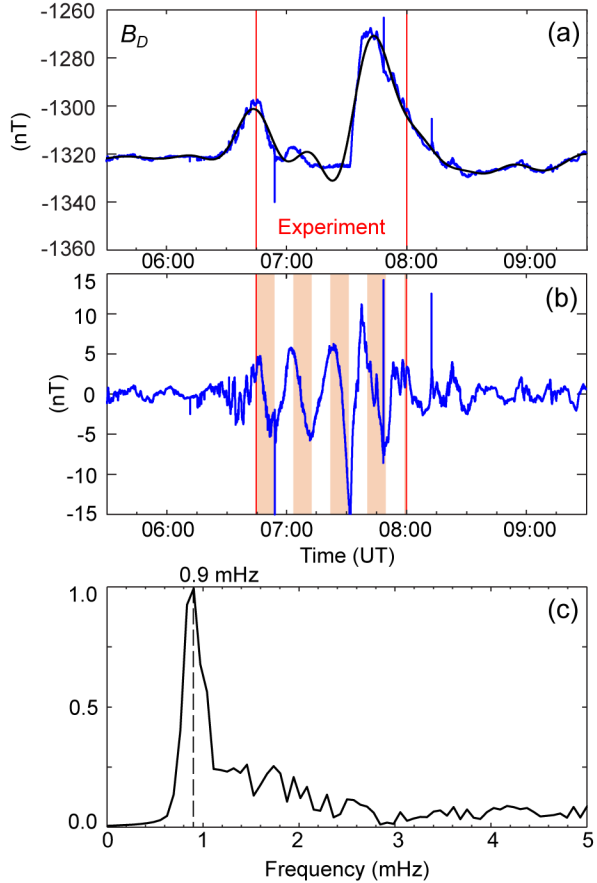


Figure 4.1: (a) The blue line shows the D-component of the magnetic field,  $B_D$ , measured by the fluxgate magnetometer in Gakona on 03/12/2013. The black line shows the low-frequency ( $\leq 0.7$  mHz) part of the signal; (b) high-frequency ( $\geq 0.7$  mHz) part of the  $B_D$  shown in panel (a); (c) normalized power spectral density (PSD) of  $B_D$  shown in panel (b). Adapted from *Tulegenov et al. [2019]*.

luminosity was observed. The third set of images was taken during the time interval 07:03:31 - 07:12:46 UT, when the heater was ON, and this set again shows a luminous spot in the ionosphere. Thus, the observations with 630.0 nm filter demonstrate optical emissions during the first two (out of total four) time intervals when the heater was ON. Observations with 557.7 nm filter demonstrate optical emissions during the same time intervals as well, although the structures of the emissions in 557.7 nm

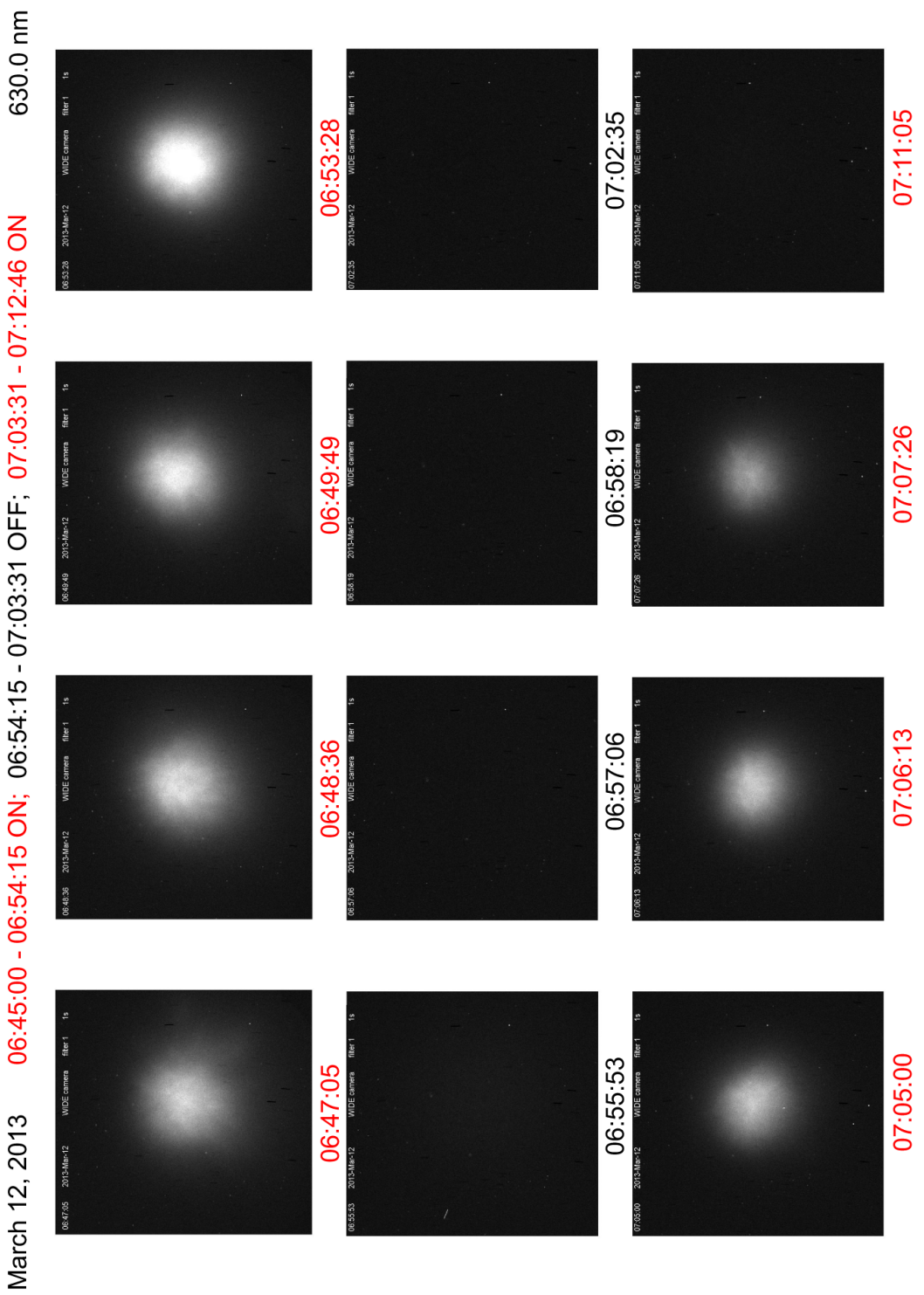


Figure 4.2: Series of images of the artificial aurora created by HAARP in 630.0 nm wavelength. Adapted from *Tulegenov et al. [2019]*.

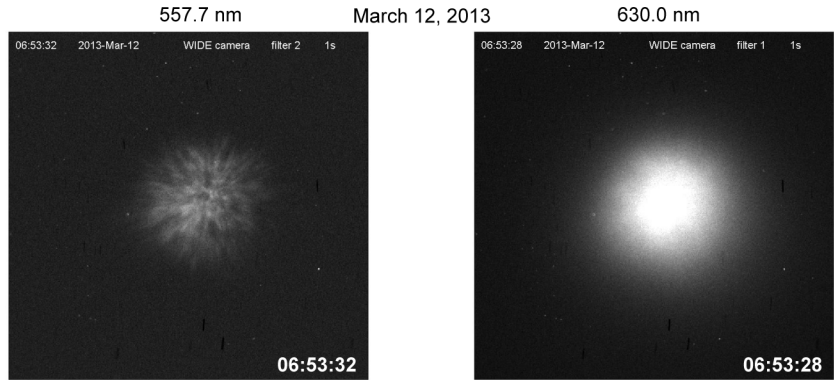


Figure 4.3: Images of the artificial aurora created by HAARP in 557.7 nm wavelength (left) and 630.0 nm wavelength (right). Adapted from *Tulegenov et al.* [2019].

wavelength are different compared to the ones observed in 630.0 nm wavelength. For comparison, Figure 4.3 shows two high resolution images in 630.0 nm and 557.7 nm wavelengths at times 06:53:28 and 06:53:32 UT correspondingly. The main difference between these two images is that 630.0 nm luminosity is relatively smooth and 557.7 nm image is more “structured” as was observed previously by *Pedersen et al.* [2010].

### 4.3 Numerical Implementation and Boundary Conditions

The 3D MHD model described previously is used to investigate the proposed theory. The constant heating of the ionosphere by HAARP is modeled by solving the highly integrated density continuity equation with the reduced recombination in the northern ionosphere

$$\frac{\partial n}{\partial t} = \frac{j_{\parallel}}{e h} + \alpha (n_0^2 - (1 - H)n^2). \quad (4.1)$$

$H$  specifies the heating. It is chosen as  $H = 0.5 e^{-(\rho/\rho_0)^2}$ , where  $\rho$  is the distance in the ionosphere from the location of the maximum of the heater beam, and  $\rho_0 = 10$  km is a half-width of the beam. Experiments with HF X-mode heating have shown that the density can be enhanced by up to 70% relative to the background [Blagoveshchenskaya *et al.*, 2015]. It is assumed that the heater modifies the density by 20%, which is well within the reported values.

The model equations are written in the orthogonal dipole coordinates  $(L, \phi, \mu)$ , where  $L = r \sin^2 \theta$ ,  $\mu = \cos \theta / r^2$ , and  $r$ ,  $\theta$ , and  $\phi$  are standard spherical coordinates. Computations have been performed in the three-dimensional dipole magnetic flux tube bounded by the ionosphere in the Northern and Southern Hemispheres. The latitudinal boundaries of the domain are formed by  $L = 4.75$  and  $L = 5.05$  magnetic shells. The azimuthal size of the domain is  $\phi \approx 1^\circ$ .

The magnitude of the large scale  $E_\perp$  is based on the digisonde drift velocities presented in Figure 4.4. Using the two components of the electron drift velocity we calculate the resultant  $E_\perp$ . The amplitude of the electric field during the first two periods of the heating was peaking at 6.5 mV/m at 06:50 UT. After 07:15 UT, the magnitude of the large-scale  $E_\perp$  decreases and reaches a minimum of 2.85 mV/m at 07:45 UT.

The profile of the background density along  $L = 4.90$  magnetic field line (corresponding to the location of HAARP) is defined as:

$$n_0 = \begin{cases} a_1(r - r_1) + a_2, & \text{if } r_1 < r < r_2 \\ b_1 e^{-20(r-r_2)} + b_2 r^{-4} + b_3, & \text{if } r > r_2. \end{cases} \quad (4.2)$$

Here  $r$  is the radial distance to point on the field line,  $r_1 = 1 + 120/R_e$ , and

$r_2 = 1 + 320/R_e$ . The constants  $a_1$ ,  $a_2$ ,  $b_1$ ,  $b_2$  and  $b_3$  are parameters that satisfy a density of  $1.25 \times 10^4 \text{ cm}^{-3}$  at E region altitude of 120 km,  $1.5 \times 10^5 \text{ cm}^{-3}$  at F region altitude of 320 km and  $129 \text{ cm}^{-3}$  in the equatorial magnetosphere.

One of the main parameters in the model is the density in the ionospheric *E* region. That density defines the conductivities of the ionosphere, which are supposed to be modified by the heating. Data from the HAARP digisonde, shown in Figure 4.5, demonstrate that this density is quite low. At least, it is below the threshold which can be detected by the digisonde. Because the digisonde can detect densities starting from  $1.25 \times 10^4 \text{ cm}^{-3}$  (corresponding to the plasma frequency of 1 MHz), it was decided to choose this value for the magnitude of the background density in the simulations. This value of the density provides  $\Sigma_P = 0.4 \text{ mho}$ .

## 4.4 Results and Discussion

The experiment conducted at HAARP on March 12, 2013, brings two equally important and interesting results. First, it demonstrates, for the first time, that heating of the ionosphere with X-mode HF waves can generate bright luminous structures in 557.7, 630.0, and 777.4 nm wavelengths. On the other hand, there were no luminous structures observed in the 427.8 nm wavelength (higher energy blue line). Figure 4.2 shows three sets of optical images in 630.0 nm wavelength taken with the HAARP telescope during the experiments. It is worth mentioning here that normally, the airglow has been observed in the ionosphere above HAARP only during the O-mode heating [Kosch *et al.*, 2005].

Of course, the X-mode heater transmissions always contain some level of contam-

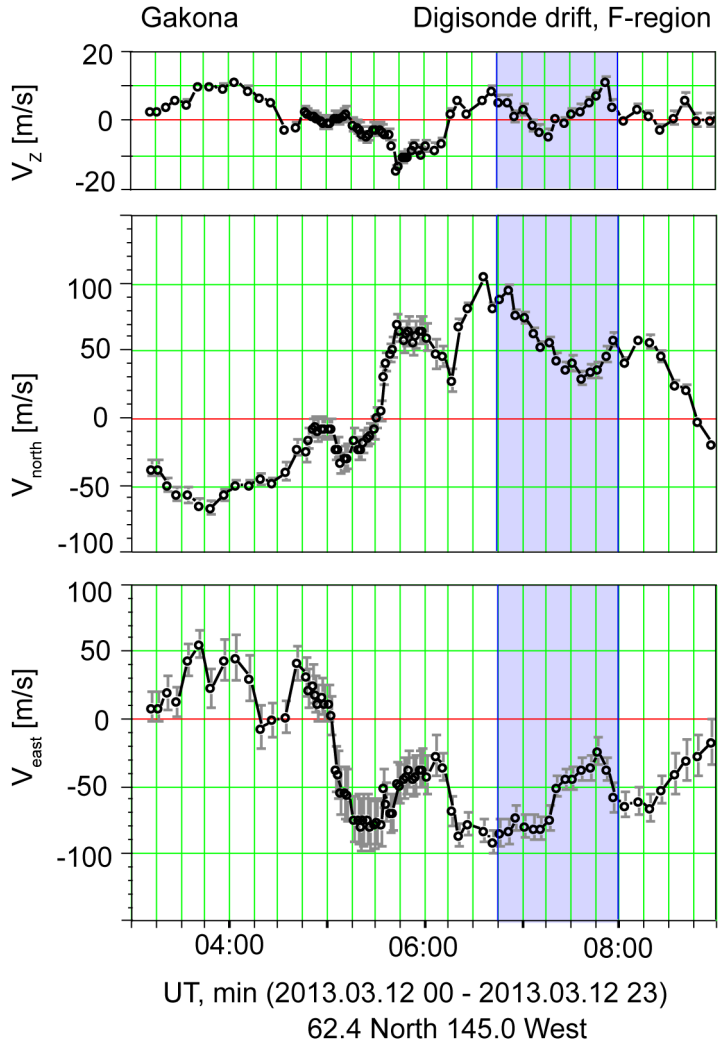


Figure 4.4: Electric field in the ionosphere above HAARP during the experiment. Adapted from *Tulegenov et al. [2019]*.

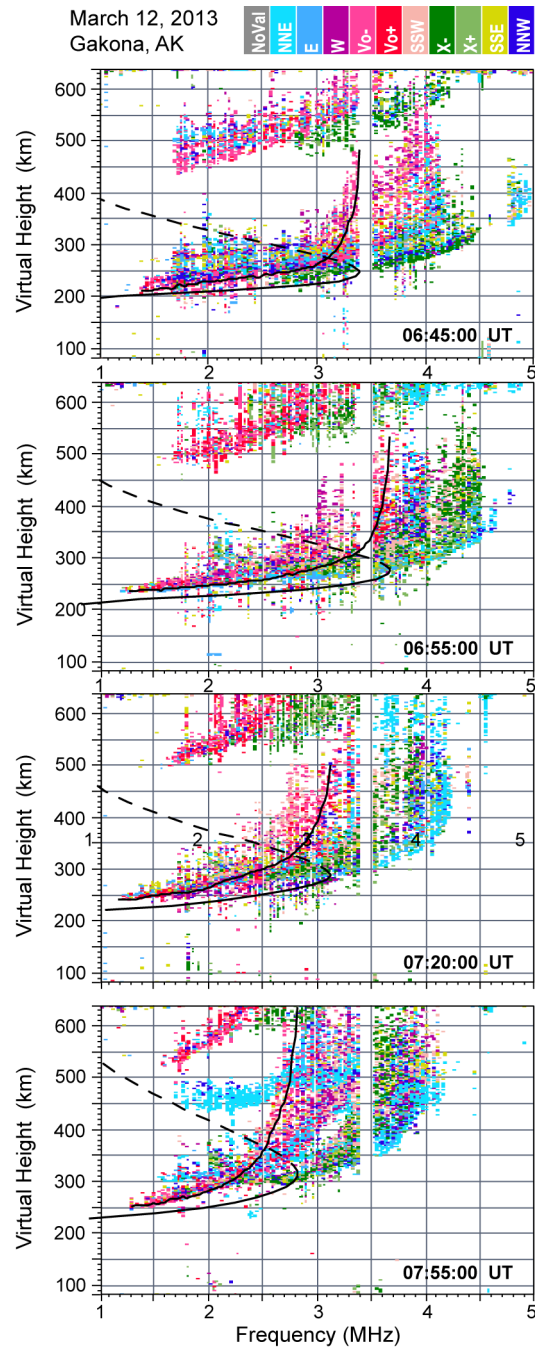


Figure 4.5: Ionospheric density above HAARP during the experiment. Adapted from Tulegenov *et al.* [2019].

inating O-mode polarization. However, the HAARP array controls and monitors the currents on each dipole independently and can maintain very high isolation between polarizations. In this case, the measured O-mode component was at least 25 dB below the X-mode level. Furthermore, the sequence of ionograms presented in Figure 4.5 shows that the highest frequency reflected by O-mode transmission, including the considerable frequency spread, was no greater than 4 MHz, well below the heating frequency of 4.57 MHz used in this experiment, while  $f_{xF2}$  exceeded the heating frequency prior to 07:20 UT.

Second, the 03/12/2013 experiment generates oscillations in the magnetic field with the frequency perfectly matching the frequency of heating modulations. These observations are shown in Figure 4.1b, which gave a strong reason to conclude that, during the experiment, HAARP indeed produces magnetic field-aligned currents flowing into the magnetosphere. This conclusion is also supported by *Streltsov and Pedersen* [2011], who showed with 3D MHD simulations that some luminous structures (in particular, rings and solid spots) produced by HAARP in the O-heating experiments can be interpreted in terms of ULF waves and field-aligned currents.

In this study, the next step is done in the development of the numerical model used by *Streltsov and Pedersen* [2011] by including the Hall conductivity in the ionosphere and using a more realistic heating mechanism. Namely, the model assumes that the heating decreases the recombination coefficient in the ionospheric E region, and the decrease in the recombination increases the density. The model is simulated based on the geomagnetic conditions observed during the experiment, and the results of the simulations are shown in Figures 4.6 and 4.7.

Specifically, in the simulations, the heating changes the plasma density in the E

region in the Northern Hemisphere according to Eq.4.1. Modification of the ionospheric density changes the conductivity, which generates field-aligned currents, if the large-scale electric field exists in the ionosphere according to the Eq.2.41. Figure 4.6 shows a snapshot of the field aligned current density inside the 3D domain at the time  $t=158.5$  s after the heating has begun. In full agreement with *Streltsov and Pedersen* [2011], the simulations demonstrate that such constant heating leads to a rapid formation of two field-aligned currents that are closed through the ionosphere in both hemispheres. The structure of the currents obtained in the simulations is different from the structure of currents shown by *Streltsov and Pedersen* [2011]. Namely, in the simulation runs performed for this study, the heating produces two current channels standing side-by-side, and in the simulations by *Streltsov and Pedersen* [2011], the currents form an axisymmetric structure. This difference is explained by the different models for the heating used in these two studies.

The FAC flows from the Southern to the Northern Hemisphere in one channel (shown with red in Figures 4.6 and 4.7) and flows in the opposite direction along the adjacent channel (shown with blue). It is assumed that these FACs may cause some parallel electric field in the current channels (due to the dispersive effect, double layer formation, anomalous resistivity, or any other mechanisms that depend on the amplitude and the transverse size of FAC), which can accelerate electrons into the ionosphere and produce artificial aurora. Figure 4.7 shows snapshots of the parallel current density and the plasma density in the ionosphere at  $t = 158.5$  s. Specifically, Figures 4.7a and 4.7c show plasma and current densities produced by the heating in the ionosphere with  $E_{\perp} = 6.5$  mV/m,  $\Sigma_P = 0.4$  mho, and  $\Sigma_H = 2\Sigma_P$ . Figures 4.7b and 4.7d show plasma and current densities produced by the heating in the

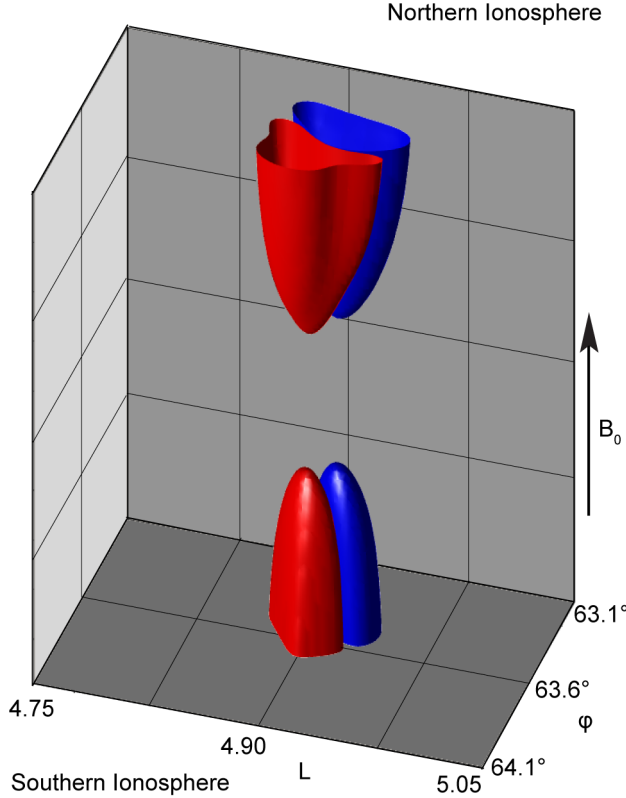


Figure 4.6: Snapshot of the parallel current density  $j_{\parallel}$  taken from the 3D simulation at  $t = 158.5$  s with  $\Sigma_H/\Sigma_P=2$ . Here isosurfaces of  $j_{\parallel} = -0.002 \mu\text{A}/\text{m}^2$  (blue) and  $j_{\parallel} = 0.002 \mu\text{A}/\text{m}^2$  (red) are shown. Adapted from *Tulegenov et al. [2019]*.

ionosphere with  $E_{\perp} = 6.5 \text{ mV/m}$ ,  $\Sigma_P = 0.4 \text{ mho}$ , and  $\Sigma_H = 0$  (no Hall current). The contour lines from Figures 4.7a and 4.7c are also shown in Figures 4.7b and 4.7d, to demonstrate relation between density enhancements produced by the heating and the structure and location of the corresponding field-aligned currents.

Figure 4.7 demonstrates that there are two important effects associated with adding a Hall conductivity into the model. First, the Hall conductivity increases the magnitude of the generated field-aligned current by 50%. This result follows directly from the eq. 2.41. Second, the Hall conductivity rotates the FAC system around the center of the heating spot. This is in the agreement with Eq. 2.41 which states that

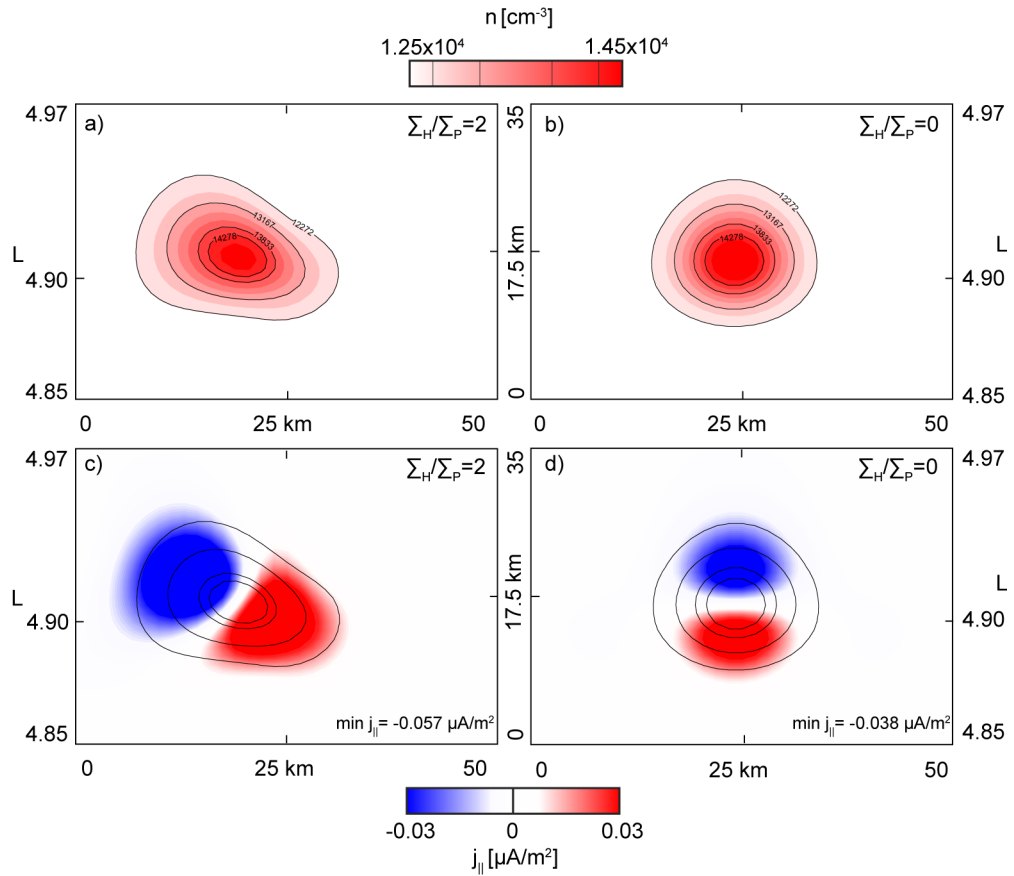


Figure 4.7: Panels a) and b) are snapshots of ionospheric density  $n$  from the numerical model at  $t=158.5$  s under different ionospheric conditions: a) with  $\Sigma_H/\Sigma_P=2$  and b) with  $\Sigma_H/\Sigma_P=0$ . Panels c) and d) are the snapshots of ionospheric  $j_{\parallel}$  at  $t=158.5$  s with  $\Sigma_H/\Sigma_P=2$  and  $\Sigma_H/\Sigma_P=0$ , respectively. The 3D simulations are performed with  $E_{\perp} = 6.5$  mV/m. The contour lines from panels a) and c) are mapped to panels b) and d) correspondingly, to demonstrate the relation between density enhancements produced by the heating and the structure and location of the corresponding field-aligned currents. Adapted from Tulegenov *et al.* [2019].

FACs are generated in the direction of the resultant ionospheric conductivity [Jia and Streltsov, 2014]. This happens because the field-aligned current is closed through the ionosphere by the combination of Pedersen and Hall currents. The Pedersen current is parallel to the background electric field, which is in the north-south direction in

the simulations, and the Hall current is perpendicular to it. Therefore, when the Hall conductivity is equal to zero, the field aligned current is closed by the Pedersen current only, and this current is aligned with the electric field in the direction from  $L = 4.75$  to  $L = 5.05$ . When the Hall conductivity is two times larger than the Pedersen conductivity, FACs are closed in the ionosphere at some angle to the direction of the background electric field.

Another interesting effect observed in the simulations is that the maximum of the downward (red) and upward (blue) field aligned currents do not coincide with the maximum of the density disturbances or the maximum of the heating power. This happens because the currents are formed by the gradients in  $(\Sigma_P \mathbf{E}_\perp + \Sigma_H \mathbf{E}_\perp \times \mathbf{b})$  (see Eq. 2.41), and when the background electric field is uniform, these gradients are produced by the density gradients only. Therefore, simulations predict that when the large-scale electric field in the ionosphere is relatively uniform, the bright luminous spot produced by the heating should be observed not exactly where the heating has a maximum power, but in the close vicinity. The exact location and the orientation of the luminous structure relative to the heating spot and the orientation of the background electric field depend on the relation between Pedersen and Hall conductivities. This conclusion is consistent with the observations which frequently show some offset between the heating and the maximum of the luminosity in heating experiments [Pedersen *et al.*, 2009; Grach *et al.*, 2016].

## 4.5 Chapter Conclusion

The reasonable agreement between the observations and results of 3D simulations lead to the conclusion that the luminous spots and disturbances in the magnetic field detected during the 03/12/2013 HAARP experiment may be related to the magnetic field-aligned currents produced by the heating of the ionosphere with the X-mode HF waves. It is also heavily emphasized that the complete physical model of the coupled and rapidly changing magnetosphere-ionosphere system during X- or O-mode heating is much more complicated and includes many physical effects which are not taken into account in the current model. In particular, the model does not resolve the vertical structure of the ionospheric E region and does not include any electro-chemistry of photo-ionization mechanism in the ionosphere. It also does not include any mechanisms producing the parallel electric field in the field-aligned currents in the magnetosphere, as well as the effects of the electron precipitation in the upward currents on the ionospheric density. Therefore, more advanced and comprehensive models of the ionosphere-magnetosphere system are necessary to unambiguously explain the results from this particular experiment.

The generation of the field-aligned currents by changing the ionospheric conductivity in the presence of the large-scale electric field in the ionosphere is one of the most basic and robust results produced by the heating. And these field-aligned currents will always contribute to the energization of the ionosphere by delivering Poynting and particle fluxes into it. Hence, it is concluded that the mechanism, considered in this Chapter and in the associated paper *Tulegenov et al. [2019]*, should always be taken into account, together with other (local ionospheric) mechanisms, in the experiments involving artificial modification of the ionosphere (D and E regions).

# Chapter 5

## 3D Model: Efficient method of generating ULF/ELF waves

*Results presented in this chapter are published in the Geophysical Research Letters [Tulegenov and Streltsov, (2019), Effects of the Hall conductivity in ionospheric heating experiments, doi:10.1029/2019GL083340].*

### 5.1 Introduction

Shear Alfvén waves carrying magnetic field-aligned currents (FACs) are one of the major participants in the redistribution of electromagnetic power, particle density, mass, and momentum between the ionosphere and magnetosphere at high latitudes [Inan *et al.*, 1985; Lysak, 1991; Chaston, 2003; Streltsov and Lotko, 2008]. That fact makes these waves an object of intensive experimental and theoretical study, and a large number of experiments devoted to the artificial excitation of these waves in the magnetosphere from the ground-based facilities have been conducted in Europe, Rus-

sia, and the USA for more than 60 years. Comprehensive reviews of these experiments and their results can be found in *Gurevich* [2007] and *Streltsov et al.* [2018].

One of the most well-known and widely used methods of generation of ULF waves from the ground is heating the ionosphere with X-mode high-frequency (HF) waves. These waves increase the bulk temperature of the electron population in the ionospheric D and E regions. The variations in the electron temperature change the Hall and Pedersen conductances in the ionosphere. Ionospheric conductivity is directly proportional to the ions' mobility. Studies and observations show that the ion mobility decreases by a factor of 1.4 or 2.0 when the ions are heated threefold or sevenfold by the perpendicular electric field, respectively [*Aikio et al.*, 2004; *Paschmann et al.*, 2012]. If there is a large-scale electric field in the ionosphere, then the changes in the conductances cause changes in the Hall and Pedersen currents flowing in the ionosphere, which, in turn, generate magnetic field-aligned current flowing into the magnetosphere. This is a so-called Getmantsev's effect [*Getmantsev et al.*, 1974], which was introduced in 1974 and extensively used after that in the high-latitude ionosphere-magnetosphere system. The auroral and subauroral zones are particularly favorable for this mechanism because, normally, there is a large-scale electric field in the ionosphere associated with the electrojet [*Stubbe and Kopka*, 1977; *Gurevich*, 2011; *Stubbe et al.*, 1981; *Robinson et al.*, 1998].

If the frequency of the generated ULF waves matches one of the eigenfrequencies of the global magnetospheric resonator (formed by the entire magnetic flux tube and bounded by the ionosphere), then these waves can form a standing pattern along the magnetic field line between the conjugate hemispheres and reach large amplitudes after some time. Simulations by *Streltsov et al.* [2005]; *Streltsov* [2011] show that

a large-amplitude (in the order of 50 nT) ULF wave can be generated even by a relatively small ionospheric disturbance modulated with the eigenfrequency of the resonator.

Because the HF power available for the ionospheric modification from ground transmitters is always limited, there are many theoretical and experimental studies devoted to the efficiency of how this power is used [Streltsov *et al.*, 2018]. Two of the most efficient methods described in the literature include “beam-painting” and geometric modulation techniques. The beam painting technique, suggested by *Papadopoulos et al.* [1989, 1990], means that the beam focuses in a small spot, which moves rapidly across some area in the ionosphere to heat electrons inside this area. The entire process is modulated with the frequency of the generated wave. The geometric modulation means that instead of heating one spot (or some area) in the ionosphere and turning the transmitter ON and OFF with the wave period, the transmitter sends a constant beam of HF power and moves it in the ionosphere along some particular geometrical path. The injection of ELF/VLF waves into the magnetosphere by the modulated heating of the electrojet by the High Altitude Active Research Program (HAARP) facility in Alaska has been extensively studied by *Papadopoulos et al.* [2003], *Golkowski et al.* [2008]; *Golkowski et al.* [2011], and *Cohen et al.* [2010].

*Streltsov and Pedersen* [2010] proposed a modification to the geometric modulation technique. They suggest to move the heating spot in the ionosphere in the direction of the background electric field with the phase speed of the feedback-unstable ULF wave. This suggestion was based on numerical simulations of the two-fluid MHD model describing active ionospheric response (aka feedback) on the structure and am-

plitude of magnetospheric field-aligned currents interacting with the ionosphere and modifying conductivity by precipitating electrons in it. The ionospheric feedback mechanism has been studied for almost 50 years [Atkinson, 1970]. The basic idea is that the ULF FAC changes the ionospheric conductivity (almost twofold from 2.0 mho to less than 0.5 mho) by precipitating/removing electrons into/from the E layer, and the variation in the conductivity “feed back” on the structure and amplitude of the incident FAC. When the large-scale electric field exists in the ionosphere, the feedback may work in a constructive way and increase the amplitude of the ULF waves and the density disturbances on the ionosphere, which lead to instability.

*Streltsov and Pedersen* [2010] used the X-mode heating to trigger and enhance the ionospheric feedback instability by synchronizing the heating regime with the dynamics of the most feedback-unstable ULF mode. This idea had been implemented during 2014 BRIOCHE research campaign at HAARP and did not produce any positive results. There are several possible reasons why these particular experiments were not successful. Among them could be: the absence of the electrojet, the high density of the ionosphere above the HAARP, unknown information about ionospheric parameters in the magnetically conjugate location, etc. However, there is one particular shortage in the *Streltsov and Pedersen* [2010] model, which may significantly compromise the applicability of the numerical results to real experiments. This shortage comes from the fact that the numerical model used was two-dimensional (with a one-dimensional ionosphere) and did not include effects of the Hall current in the ionosphere. At the same time, the importance of the Hall current for the ionospheric feedback mechanism has been emphasized in almost every classical paper about the instability [e.g. *Atkinson*, 1970; *Sato*, 1978; *Miura et al.*, 1982; *Trakhtengerts and*

*Feldstein, 1991; Borisov and Stubbe, 1997; Pokhotelov et al., 2000].*

## 5.2 Numerical Implementation and Boundary Conditions

The goal of this study is to eliminate the aforementioned shortage and investigate the effects of the Hall current on the dynamics of the magnetosphere-ionosphere interactions involving the ionospheric feedback mechanism triggered and controlled by the artificial ionospheric heating. This study is based on a 3D reduced two-fluid MHD (RMHD) model described in the previous chapter.

The ionospheric part consists of the modified density continuity equation

$$\frac{\partial n}{\partial t} = \frac{j_{\parallel}}{eh} + \alpha (n_0^2 - (1 - H)n^2). \quad (5.1)$$

Effect of the X-mode HF heating is modeled via a decrease in the coefficient of the recombination in the *E*-region. It is specified by the function  $H(\rho)$ , which is chosen as  $H(\rho) = 0.1 e^{-(\rho/\rho_0)^2}$ . Here  $\rho$  is the distance in the ionosphere from the center of the heated spot (where the heater power maximizes), and  $\rho_0 = 10$  km is a half-width of the heated spot beam. The maximum amplitude of  $H$  at  $\rho = 0$  is 0.1, which means that the heating changes the coefficient of the recombination by 10%.

The latitudinal boundaries of the domain are formed by the  $L = 4.6$  and  $L = 5.2$  magnetic shells. The azimuthal size of the domain is  $\phi = 1.91^\circ$ .

The background parameters of the model are similar to the typical parameters of the ionosphere-magnetosphere system considered in other studies, e.g., [Streltsov

and Pedersen, 2010]. The background density along the  $L = 4.9$  magnetic field line, whose ionospheric footprint corresponds to the HAARP location, is defined as:

$$n_0 = \begin{cases} a_1(r - r_1) + a_2, & \text{if } r_1 < r < r_2 \\ b_1 e^{-20(r-r_2)} + b_2 r^{-4} + b_3, & \text{if } r > r_2. \end{cases} \quad (5.2)$$

Here  $r$  is the radial distance to point on the field line,  $r_1 = 1 + 100/R_e$ , and  $r_2 = 1 + 220/R_e$ . The constants  $a_1$ ,  $a_2$ ,  $b_1$ ,  $b_2$  and  $b_3$  are parameters that satisfy a density of  $1.00 \times 10^4 \text{ cm}^{-3}$  at E region altitude of 100 km,  $2.63 \times 10^5 \text{ cm}^{-3}$  at F region altitude of 220 km and  $129 \text{ cm}^{-3}$  in the equatorial magnetosphere. The density of  $1.00 \times 10^4 \text{ cm}^{-3}$  in the E region provides the height-integrated Pedersen conductivity of 0.32 mho. Inside the computational domain the density is assumed to be homogeneous in the direction perpendicular to the ambient magnetic field. This is a reasonable assumption due to the relatively small perpendicular size of the domain (0.6  $L$  shell in the  $L$  direction and less than  $2^\circ$  in the  $\phi$  direction).

The background electric field in the domain is defined as  $E_0 = -\nabla\Phi$ , where  $\Phi$  is the electric potential. In the ionosphere, the potential  $\Phi$  is chosen to provide a uniform electric field with a magnitude 20 mV/m pointed in the north-south direction. This electric potential remains constant along the ambient magnetic field lines, so there is not any background parallel electric field (or the parallel potential drop) present in the magnetosphere. This field is comparable with the the background electric field considered in 2D simulations of the ionospheric heating by Streltsov and Pedersen [2010].

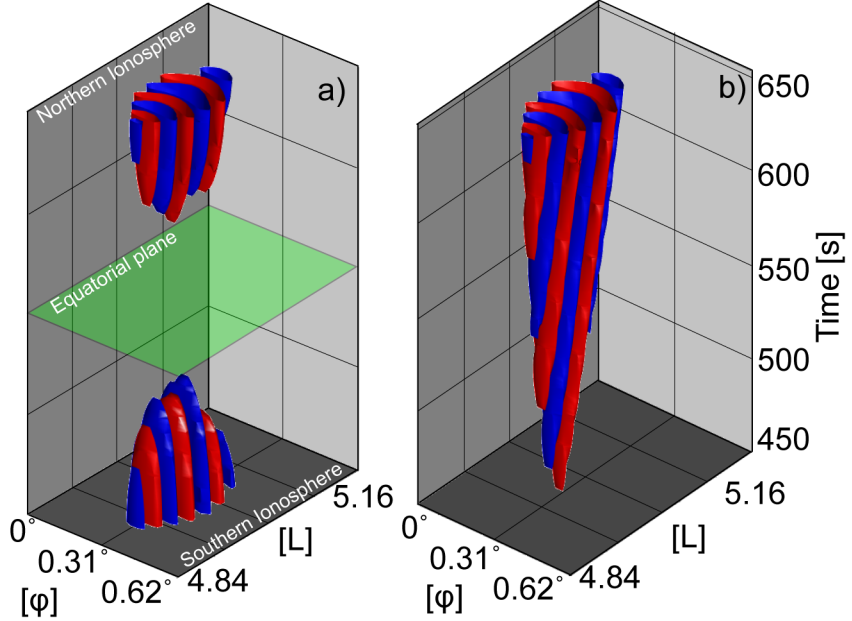


Figure 5.1: Isosurfaces of  $j_{\parallel} = -0.1 \mu\text{A/m}^2$  (blue) and  $j_{\parallel} = 0.1 \mu\text{A/m}^2$  (red) are shown from the 3D MHD simulation with  $\Sigma_H/\Sigma_P = 0$ . (a) The snapshot of the parallel current density,  $j_{\parallel}$ , generated by heating the Northern ionosphere at a fixed location at  $t = 651$  s. (b) Time evolution of  $j_{\parallel}$  on the Northern ionosphere generated by heating the Northern ionosphere at a fixed location. Adapted from *Tulegenov and Streltsov [2019]*.

### 5.3 Results and Discussion

Firstly, the main results from the 2D simulations by *Streltsov and Pedersen [2010]* are verified using a 3D model output. Namely, that the movement of the heating spot in the ionosphere with the phase velocity of the feedback-unstable mode leads to a generation of larger amplitude waves in a shorter time, than the heating of some stationary location in the ionosphere. To verify this result the 3D code is run with  $\Sigma_H = 0$ . In the first run, the heating was focused on a stationary spot in the ionosphere. The results from this run are shown in Figure 5.1. In particular, Figure 5.1a shows a snapshot of the parallel current density  $j_{\parallel}$ , inside the 3D domain, at time

$t = 651$  s after the beginning of heating. Figure 1a shows the surfaces of  $j_{\parallel} = 0.1 \mu\text{A}/\text{m}^2$  in red and surfaces of  $j_{\parallel} = -0.1 \mu\text{A}/\text{m}^2$  in blue. Figure 1b shows the temporal dynamics of  $j_{\parallel}$  measured at an altitude of 100 km in the Northern Hemisphere. Again, the red color is used to show the surfaces of  $j_{\parallel} = 0.1 \mu\text{A}/\text{m}^2$  and the blue color is used to show the surfaces of  $j_{\parallel} = -0.1 \mu\text{A}/\text{m}^2$ . Figure 5.1 illustrates development of the ionospheric feedback instability driven by the uniform 20 mV/m electric field and triggered by the constant heating of the ionosphere.

The results from this run had been used to estimate the phase velocity of the feedback-unstable waves in the ionosphere. Comparison of  $j_{\parallel}$  in the ionosphere in several instances in time, shows that the waves generated by the instability propagate in the direction of the background electric field (in this case it is the  $L$  direction) with a phase speed of  $\approx 100$  m/s. This value is equal to the phase velocity calculated from the linear dispersion relation given for the most unstable mode by *Sato* [1978], which for the parameters used in this study is  $\omega/k_{\perp} = M_P E_{\perp 0}/2 = 100$  m/s.

To model the moving of the heating spot in the ionosphere, we make the  $H$  function in Eq. 5.1 depending on time, namely,  $H = H(v_L t + L_0, v_{\phi} t + \phi_0)$ , where  $v_L$  and  $v_{\phi}$  are the wave front's phase velocity components estimated from the simulation with stationary heating spot in the ionosphere. In case  $\Sigma_H = 0$ , the  $L$ -component of the phase velocity in the ionosphere is 100 m/s and  $v_{\phi} = 0$ . Figure 5.2 illustrates a comparison between  $j_{\parallel}$  obtained in the simulations with a stationary heating spot (left panels) and with a moving heating spot (right panels). In particular, Figures 5.2c and 5.2d show time evolution of  $j_{\parallel}$ , in the Northern Hemisphere ionosphere, at a 2D longitudinal cut through the computational domain at  $L = 4.9$  from  $t = 400$  s to  $t = 651$  s after the heater was turned on. Figures 5.2a and 5.2b show magnitudes

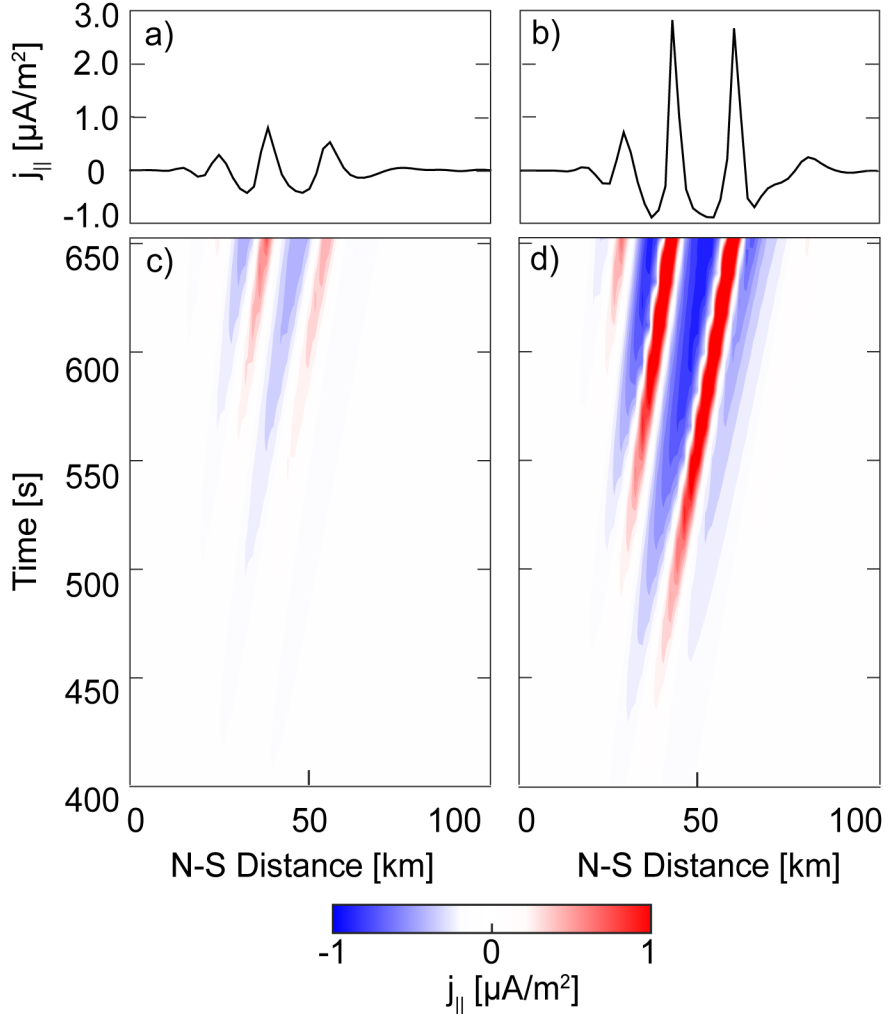


Figure 5.2: Panels a) and c) are the simulation output where the heater was heating a fixed location in the Northern ionosphere. Panels b) and d) are the simulation output in a case where the heating spot was moving in the direction of background  $E_{\perp}$  with velocity of 100 m/s. Panels c) and d) show the time evolution of FACs on the Northern ionosphere along the direction of background electric field from  $L = 4.84$  to  $L = 5.16$  in a case when  $\Sigma_H/\Sigma_P = 0$ . Panels a) and b) show the amplitude of the FACs at  $t = 651$  s. Adapted from *Tulegenov and Streltsov [2019]*.

of  $j_{\parallel}$  in the ionosphere in the northern hemisphere at  $t = 651$  s.

Figure 5.2 demonstrates that the ULF waves are generated faster when the heater moves along the  $E_{\perp}$ . The amplitudes of the waves generated by moving the heat-

ing spot are  $\approx 3$  times larger than those generated by heating a fixed spot in the ionosphere. These results confirm the conclusion made by *Streltsov and Pedersen* [2010], that without Hall current in the ionosphere the instability indeed develops more rapidly when the heating spot moves along the direction of the background electric field at the phase velocity of the wave front.

Next, 3D simulations are performed for the case when the instability is initiated by the heating of a stationary spot in the ionosphere when the Hall conductivity is not equal to zero. Figure 5.3 shows the structure and magnitude of  $j_{\parallel}$  in the Northern Hemisphere ionosphere at time  $t = 356$  s in simulations with  $\Sigma_P = 0.32$  mho and a)  $\Sigma_H/\Sigma_P = 0$ , b)  $\Sigma_H/\Sigma_P = 0.5$ ; c)  $\Sigma_H/\Sigma_P = 1.0$ ; d)  $\Sigma_H/\Sigma_P = 1.5$ ; and e)  $\Sigma_H/\Sigma_P = 2.0$ . It shows two effects. First, the amplitude of  $j_{\parallel}$  increases with the increase of  $\Sigma_H$ . This effect follows directly from the ionospheric current continuity (Eq. 2.41), which shows that the magnitude of  $j_{\parallel}$  in the ionosphere is proportional to  $\Sigma_P$ ,  $\Sigma_H$ , and  $E_{\perp}$ . Therefore, if one of these three parameters increases and two other remain constant, then  $j_{\parallel}$  is expected to increase as well.

The second effect shown in Figure 5.3 is that the feedback-unstable waves propagate across the magnetic field in the direction that makes an angle with the background  $E_{\perp}$  (which is in the N-S direction in all these simulations). This angle increases with an increase in  $\Sigma_H/\Sigma_P$ . This effect is also expected and it has been previously reported by *Jia and Streltsov* [2014] from the simulations of discrete auroral arcs produced by the ionospheric feedback mechanism involving the Hall conductivity. This can be explained by the fact that in the magnetosphere-ionosphere coupled system, the magnetic field-aligned currents are closed in the ionosphere by Hall and Pedersen currents. Larger Hall conductivity provides a greater contribution from the Hall term,

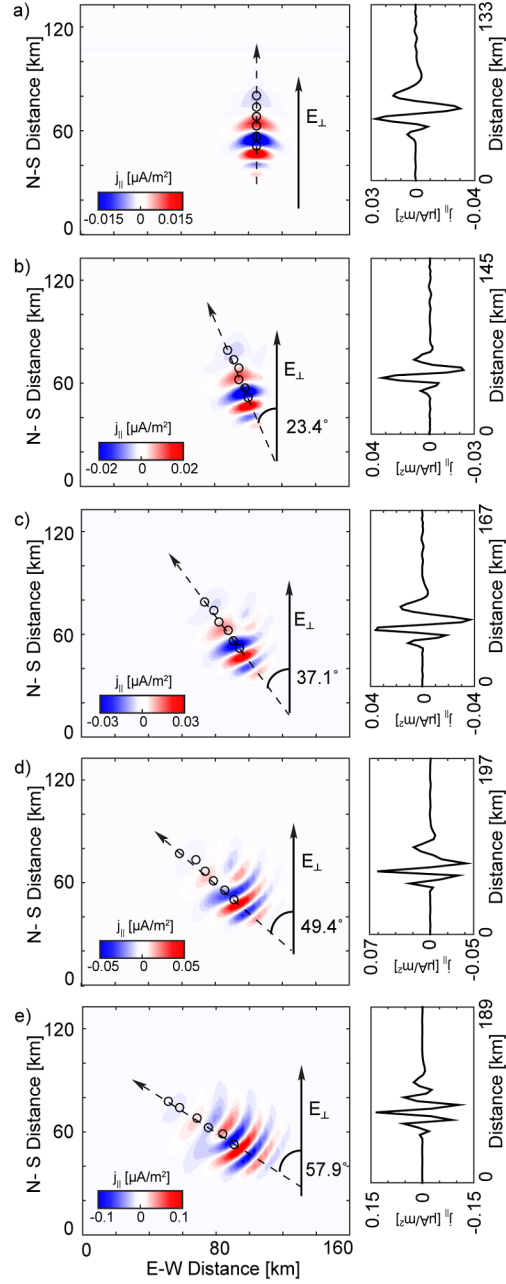


Figure 5.3: Snapshots of  $j_{\parallel}$  on the Northern ionosphere at  $t = 356$  s under different ionospheric conditions: (a)  $\Sigma_H/\Sigma_P = 0$ ; (b)  $\Sigma_H/\Sigma_P = 0.5$ ; (c)  $\Sigma_H/\Sigma_P = 1.0$ ; (d)  $\Sigma_H/\Sigma_P = 1.5$ ; and (e)  $\Sigma_H/\Sigma_P = 2.0$ . The line plots in each panel show the amplitude of FAC along the dashed arrow. The black circles indicate the propagation in time of the first wave fronts. The time step between circles is 59.43 seconds. Adapted from Tulegenov and Streltsov [2019].

and the entire current system changes its orientation with increase in  $\Sigma_H/\Sigma_P$ .

The angles between the wave phase velocity and the background electric field observed in the simulations for different values of  $\Sigma_H/\Sigma_P$  are  $0^\circ$ ,  $23.4^\circ$ ,  $37.1^\circ$ ,  $49.4^\circ$ , and  $57.9^\circ$ . The corresponding angles calculated analytically as  $\arctan(\Sigma_H/\Sigma_P)$  are  $0^\circ$ ,  $26.6^\circ$ ,  $45.0^\circ$ ,  $56.3^\circ$ , and  $63.4^\circ$ . The analytical and numerical sets of angles show the same dependency on the  $\Sigma_H/\Sigma_P$  ratio but they are different in magnitudes. The possible explanation of the differences between the corresponding values is that the angle calculated as  $\arctan(\Sigma_H/\Sigma_P)$  assumes that the electric field is constant. This assumption does not work when the amplitude of the feedback-unstable waves reaches larger value. At this stage, the amplitude of the electric field produced in the ionosphere by the waves becomes comparable with the amplitude of the background field: so the amplitude and the orientation of the total field in the ionosphere differ from the background/initial field.

To evaluate the effect of the moving heating spot on the development of the instability, a simulation was performed with the heating spot moving in the ionosphere with a velocity estimated from the simulations with stationary heating. Thus, the circles in Figure 5.3 indicate locations of the first wavelength of the generated wave in time. Figure 5.4 shows  $j_{\parallel}$  in the Northern ionosphere obtained from the simulations with  $\Sigma_H/\Sigma_P = 2.0$  at time  $t = 356$  s (a) when the heating spot is fixed in space and (b) when the heating spot moves at the angle of  $57.9^\circ$  to the background  $E_{\perp}$  with a velocity  $v_L = 133$  m/s and  $v_{\phi} = 83.4$  m/s, which correspond to the phase velocity of the first wave front. Figure 5.4 demonstrates that, similar to the case with no Hall current, the ULF waves are generated more efficiently (they reach larger amplitude faster), when the ionospheric feedback mechanism is “enhanced” by the

moving heating spot in the ionosphere with the wave phase velocity.

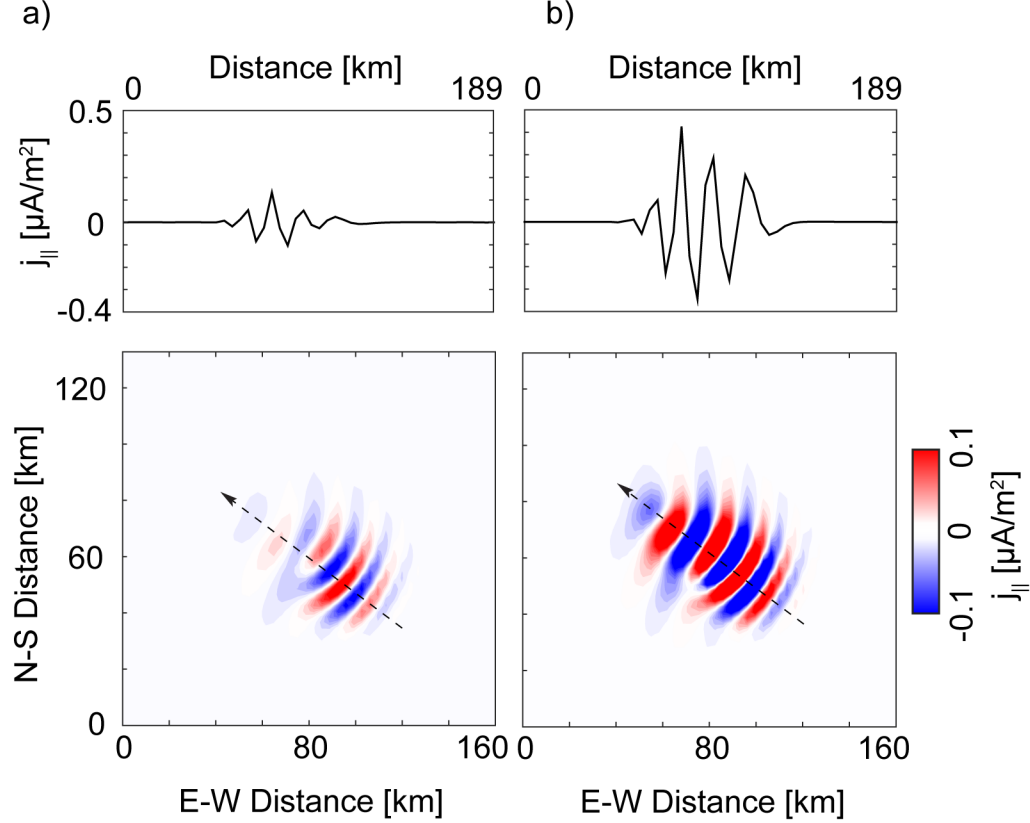


Figure 5.4: The snapshots of the  $j_{\parallel}$  at  $t = 356$  s on the Northern ionosphere from simulations with  $\Sigma_H/\Sigma_P = 2.0$  under different heating methods: (a) fixed heating spot; (b) moving heating spot. The line plots in both panels show the amplitude of FAC along the dashed arrow. Adapted from *Tulegenov and Streltsov [2019]*.

## 5.4 Chapter Conclusion

These findings may provide a possible explanation of the failure of the experiments with the “directional” heating, described in this study and in the associated paper *Tulegenov and Streltsov [2019]*, in the 2014 BRIOCHE HAARP campaign: These experiments were based on 2D simulations not taking into account the Hall current

in the ionosphere. The effect of this current is quite significant, particularly, when  $\Sigma_H/\Sigma_P = 2.0$ . It may also explain the more efficient wave generation observed in some experiments with the geometric modulation of heating reported by *Cohen et al.* [2008, 2010]. The results suggest that the heating is more efficient when the heating spot moves with a velocity which is close to the phase velocity of the feedback unstable waves. The heater must move in the direction of the total ionospheric current. Possibly, such an agreement between the velocity of the heating spot and the phase speed of the generated waves happened during some of experiments with geometric modulation of the ionosphere.

# Chapter 6

## Conclusions and Future Work

### 6.1 Conclusions

The work presented in this dissertation uses the variations of the non-linear reduced magnetohydrodynamic 3D model that was presented in Chapter 2. The results presented in Chapters 3-5 have been published in three papers:

1. Tulegenov and Streltsov, (2017), Ionospheric Alfvén resonator and aurora: Modeling of MICA observations, *Journal of Geophysical Research: Space Physics*, 122, 7530, doi:10.1002/2017JA024181;
2. Tulegenov et al., (2019), Artificial aurora produced by HAARP, *Journal of Geophysical Research: Space Physics*, 124, doi:10.1029/2019JA026607;
3. Tulegenov and Streltsov, (2019), Effects of the Hall conductivity in ionospheric heating experiments, *Geophysical Research Letters*, doi:10.1029/2019GL083340.

The results of this dissertation paper has also been presented in various national and

international conferences and workshops:

1. Tulegenov, B., and A.V. Streltsov, Ionospheric feedback instability in the ionospheric Alfvén resonator at high latitudes: Modeling and observations, (talk), USNC-URSI National Radio Science Meeting, Boulder, CO, January 4-7, 2017;
2. Tulegenov, B., and A.V. Streltsov, ULF Waves in the ionospheric Alfvén resonator: Observations and simulations (poster), UN/USA Workshop on the International Space Weather Initiative, Boston College, MA, 31 July-4 August, 2017;
3. Tulegenov, B., and A.V. Streltsov, ULF waves in the ionospheric Alfvén resonator: Observations and simulations (H42-2 talk), URSI General Assembly and Scientific Symposium, Montreal, Canada, 19-26 August, 2017;
4. Tulegenov, B., and A.V. Streltsov, ULF Waves in the ionospheric Alfvén resonator: Modeling of MICA observations, (SM41A-2676 poster), AGU Fall Meeting, New Orleans, LA, December 11-15, 2017;
5. Tulegenov, B., and A.V. Streltsov, Ionospheric feedback instability in the Alfvén resonator at high latitudes: 3D modeling, (talk), USNC-URSI National Radio Science Meeting, Boulder, CO, January 4-7, 2018;
6. Tulegenov, B., and A.V. Streltsov, Ionospheric feedback instability in the Alfvén resonator at high latitudes: 3D modelling, (SM51G-2812 poster), AGU Fall Meeting, Washington, D.C., December 10-14, 2018;
7. Tulegenov, B., and A.V. Streltsov, E. Kendall, M. McCarrick, I. Galkin, Excitation and modeling of artificial aurora at HAARP, (talk), USNC-URSI National

Radio Science Meeting, Boulder, CO, January 9-12, 2019;

8. Tulegenov, B., and A.V. Streltsov, Effects of the Hall conductivity in the ionospheric heating experiments, (poster), GEM Workshop, Santa Fe, NM, June 25, 2019.

Specific drivers and boundary conditions were designed for each of the scientific tasks discussed in Chapters 3-5. The first study (discussed in Chapter 3) focused on proving the existence of small-scale large-amplitude structures next to the auroral arc. The second study (discussed in Chapter 4) demonstrated that the contribution of FACs generated with the HF heating is significant for the production of artificial auroras. The third study (discussed in Chapter 5) focused on improving the efficiency of HF heating in generating ULF structures. The main conclusions from these studies are presented in the paragraphs below.

Presence of the small-scale large amplitude dispersive Alfvén waves in the downward current channel associated with bright discrete auroral arc was confirmed numerically and experimentally in Chapter 3 and the associated paper *Tulegenov and Streltsov [2017]*. An experimental confirmation of the hypothesis presented by *Streltsov and Lotko [2008]* (that the small-scale intense current structures will be formed in a region where a return field-aligned current associated with the discrete auroral arc) was obtained through the MICA sounding rocket experiment that was launched into the discrete auroral arc region. 2D reduced MHD simulations based on the numerical model derived in Chapter 2 were performed using the MICA measurements as input parameters. The output produced confirmed the hypothesis that the IFI mechanism is responsible for the generation of small-scale large amplitude Alfvén waves under the presence of large-scale current structures in the auroral ionosphere. Numerical

results reproduced the frequency, spatial structure and the amplitudes of the small-scale large amplitude FACs that were measured by MICA rocket as it passed next to one discrete auroral arc and through another arc. It is also shown that these intense structures are confined and amplified inside the ionospheric Alfvén resonator. Spatio-temporal characteristics of these small-scale currents depend on the plasma inside the resonator (in particular, the magnitude of the plasma density inside the ionospheric E and F regions) together with the amplitude of the large-scale currents producing the aurora and driving the instability. Simulations presented in this chapter confirm that the MICA project achieved the goals formulated in their proposal and made a significant contribution in the experimental verification of the importance of the ionospheric feedback instability inside the ionospheric Alfvén resonator in the auroral zone.

Chapter 4 and the associated paper *Tulegenov et al. [2019]* present results from the 03/12/2013 HAARP experiment, where the ionosphere was heated with the X-mode HF waves and bright luminous spots in the ionosphere were observed together with the disturbances of the magnetic field on the ground. It is demonstrated with 3D MHD simulations that these effects are consistent with the structure and dynamics of the magnetic field-aligned currents generated by the variation in the ionospheric density when the large-scale electric field exists in the ionosphere. Simulations reveal that the X-mode heating of the ionosphere generates field-aligned currents with maximum intensity shifted relative to the center of the heating spot, as was observed in many experiments. Effects of the Hall conductivity on the structure of the generated currents were investigated: the simulations reveal that Hall conductivity 1) increases the amplitude of the generated field-aligned currents and 2) changes the location and

the orientation of the current flowing into the ionosphere relative to the direction of the background electric field. Results from the 3D simulations show a reasonable agreement with the observations. The main conclusion from the work done is that the field-aligned currents certainly contribute to the total energization of the ionosphere, and should be taken into account together with other, pure ionospheric mechanisms, to explain results of experiments involving modification of the ionospheric D and E regions.

There were two major findings determined in Chapter 5 and the associated paper *Tulegenov and Streltsov [2019]*. The first one is that the Hall conductivity indeed plays an important role in the generation of large-amplitude ULF waves by the ionospheric feedback mechanism driven by the electric field in the ionosphere. Our simulations confirm results from earlier studies that the Hall conductivity 1) increases the growth rate of the instability and 2) changes the direction of propagation of the feedback unstable waves relative to the background electric field in the ionosphere. The second conclusion is that the efficiency of generation of ULF waves by the ionospheric HF heating can be increased significantly by moving the heating spot with a phase velocity of the feedback unstable waves taking into account the presence of the Hall current in the ionosphere. The amplitude and direction of this velocity can be estimated during the experiment from the observations of plasma density, temperature, and the ion drift speed with phase radars (if they are available) and digisonds, and from 3D numerical simulations, performed in advance for various possible combinations of the background parameters.

## 6.2 Future Work

The science introduced in this dissertation can be expanded upon in a number of different ways. The numerical model used in this study could be expanded to include the effect of multiple species, namely  $O^+$ ,  $O_2^+$ ,  $H^+$ , and  $e^-$ . Currently it only incorporates two species: electrons and protons. Another improvement to the model would be the introduction of the ion Joule heating effect. This heating is caused by the electric field of the large-amplitude ULF waves. The model could also incorporate the effect of the collisionless transverse ion energization and associated upward lifting force by the mirror force. Once introduced, the model would be able to explore in detail the mechanism for transporting heavy ions into the equatorial magnetosphere, cavity formation, and ion heating. The new model would also explore the effects of this ion outflow on the spatio-temporal properties of the global and ionospheric Alfvén resonators. The developed model could be used to study non-linear MI coupling in the auroral zone and to model observational events selected from the ground-based optical, satellite (ICON, MMS, THEMIS, Cluster, to name a few), and sounding rocket experiments.

# Bibliography

- Aikio, A. T., K. Mursula, S. Buchert, F. Forme, O. Amm, G. Marklund, M. Dunlop, D. Fontaine, A. Vaivads, and A. Fazakerley (2004), Temporal evolution of two auroral arcs as measured by the Cluster satellite and coordinated ground-based instruments, *Annales Geophysicae*, 22(12), 4089–4101, doi:10.5194/angeo-22-4089-2004.
- Angelopoulos, V., J. A. Chapman, F. S. Mozer, J. D. Scudder, C. T. Russell, K. Tsuruda, T. Mukai, T. J. Hughes, and K. Yumoto (2002), Plasma sheet electromagnetic power generation and its dissipation along auroral field lines, *Journal of Geophysical Research: Space Physics*, 107(A8), SMP 14–1–SMP 14–20, doi: 10.1029/2001JA900136.
- Archer, M. O., H. Hietala, M. D. Hartinger, F. Plaschke, and V. Angelopoulos (2019), Direct observations of a surface eigenmode of the dayside magnetopause, *Nature Communications*, 10(1), 615, doi:10.1038/s41467-018-08134-5.
- Atkinson, G. (1970), Auroral arcs: Result of the interaction of a dynamic magnetosphere with the ionosphere, *Journal of Geophysical Research*, 75(25), 4746–4755, doi:10.1029/ja075i025p04746.
- Balay, S., W. D. Gropp, L. C. McInnes, and B. F. Smith (1997), Efficient Management

of Parallelism in Object-Oriented Numerical Software Libraries, in *Modern Software Tools for Scientific Computing*, pp. 163–202, Birkhäuser Boston, Boston, MA, doi: 10.1007/978-1-4612-1986-6\_8.

Belyaev, P., S. Polyakov, V. Rapoport, and V. Trakhtengerts (1990), The ionospheric Alfvén resonator, *Journal of Atmospheric and Terrestrial Physics*, 52(9), 781–788, doi:10.1016/0021-9169(90)90010-K.

Bernhardt, P. A., L. M. Duncan, and C. A. Tepley (1988), Artificial Airglow Excited by High-Power Radio Waves, *Science*, 242(4881), 1022–1027, doi: 10.1126/science.242.4881.1022.

Bernhardt, P. A., C. A. Tepley, and L. M. Duncan (1989), Airglow enhancements associated with plasma cavities formed during Ionospheric Heating Experiments, *Journal of Geophysical Research*, 94(A7), 9071, doi:10.1029/ja094ia07p09071.

Blagoveshchenskaya, N., V. A. Kornienko, T. D. Borisova, B. Thidé, M. J. Kosch, M. T. Rietveld, E. V. Mishin, R. Y. Luk'yanova, and O. A. Troshichev (2001), Ionospheric HF pump wave triggering of local auroral activation, *Journal of Geophysical Research: Space Physics*, 106(A12), 29,071–29,089, doi:10.1029/2001ja900002.

Blagoveshchenskaya, N., T. Borisova, T. Yeoman, I. Häggström, and A. Kalishin (2015), Modification of the high latitude ionosphere F region by X-mode powerful HF radio waves: Experimental results from multi-instrument diagnostics, *Journal of Atmospheric and Solar-Terrestrial Physics*, 135, 50–63, doi:10.1016/j.jastp.2015.10.009.

Boehm, M. H., C. W. Carlson, J. P. McFadden, J. H. Clemons, and F. S. Mozer (1990), High-resolution sounding rocket observations of large-amplitude Alfvén waves, *Journal of Geophysical Research*, 95(A8), 12,157, doi:10.1029/JA095iA08p12157.

Borisov, N., and P. Stubbe (1997), Excitation of longitudinal (field-aligned) currents

- by modulated HF heating of the ionosphere, *Journal of Atmospheric and Solar-Terrestrial Physics*, 59(15), 1973–1989, doi:10.1016/S1364-6826(97)00019-9.
- Borovsky, J. E. (1993), Auroral arc thicknesses as predicted by various theories, *Journal of Geophysical Research: Space Physics*, 98(A4), 6101–6138, doi:10.1029/92JA02242.
- Bösinger, T. (2002), Spectral properties of the ionospheric Alfvén resonator observed at a low-latitude station (  $L = 1.3$ ), *Journal of Geophysical Research*, 107(A10), 1281, doi:10.1029/2001JA005076.
- Brekke, A., J. R. Doupinik, and P. M. Banks (1974), Incoherent scatter measurements of E region conductivities and currents in the auroral zone, *Journal of Geophysical Research*, 79(25), 3773–3790, doi:10.1029/JA079i025p03773.
- Burden, R., and J. Faires (1991), *Numerical Analysis*, International Thomson Publishing.
- Chaston, C. C. (2003), Properties of small-scale Alfvén waves and accelerated electrons from FAST, *Journal of Geophysical Research*, 108(A4), 8003, doi:10.1029/2002JA009420.
- Chaston, C. C., J. W. Bonnell, C. W. Carlson, M. Berthomier, L. M. Peticolas, I. Roth, J. P. McFadden, R. E. Ergun, and R. J. Strangeway (2002), Electron acceleration in the ionospheric Alfvén resonator, *Journal of Geophysical Research: Space Physics*, 107(A11), 1413, doi:10.1029/2002JA009272.
- Chen, L., and A. Hasegawa (1974), A theory of long-period magnetic pulsations: 1. Steady state excitation of field line resonance, *Journal of Geophysical Research*, 79(7), 1024–1032, doi:10.1029/JA079i007p01024.
- Cheng, C. Z. (1991), A kinetic-magnetohydrodynamic model for low-frequency phenom-

ena, *Journal of Geophysical Research*, 96(A12), 21,159, doi:10.1029/91JA01981.

Chmyrev, V. M., S. V. Bilichenko, O. A. Pokhotelov, V. A. Marchenko, V. I. Lazarev, A. V. Streltsov, and L. Stenflo (1988), Alfvén vortices and related phenomena in the ionosphere and the magnetosphere, *Physica Scripta*, 38(6), 841–854, doi: 10.1088/0031-8949/38/6/016.

Cohen, I. J., M. R. Lessard, S. R. Kaepller, S. R. Bounds, C. A. Kletzing, A. V. Streltsov, J. W. Labelle, M. P. Dombrowski, S. L. Jones, R. F. Pfaff, D. E. Rowland, B. J. Anderson, H. Korth, and J. W. Gjerloev (2013), Auroral Current and Electrodynamics Structure (ACES) observations of ionospheric feedback in the Alfvén resonator and model responses, *Journal of Geophysical Research: Space Physics*, 118(6), 3288–3296, doi:10.1002/jgra.50348.

Cohen, M. B., U. S. Inan, and M. A. Golkowski (2008), Geometric modulation: A more effective method of steerable ELF/VLF wave generation with continuous HF heating of the lower ionosphere, *Geophysical Research Letters*, 35(12), n/a–n/a, doi: 10.1029/2008GL034061.

Cohen, M. B., U. S. Inan, M. Gołkowski, and M. J. McCarrick (2010), ELF/VLF wave Generation via ionospheric HF heating: Experimental comparison of amplitude modulation, beam painting, and geometric modulation, *Journal of Geophysical Research: Space Physics*, 115(2), n/a–n/a, doi:10.1029/2009JA014410.

Cummings, W. D., R. J. O'Sullivan, and P. J. Coleman (1969), Standing Alfvén waves in the magnetosphere, *Journal of Geophysical Research*, 74(3), 778–793, doi: 10.1029/ja074i003p00778.

Doe, R. A., J. F. Vickrey, and M. Mendillo (1995), Electrodynamic model for the formation of auroral ionospheric cavities, *Journal of Geophysical Research*, 100(A6),

9683, doi:10.1029/95ja00001.

Dombeck, J., C. Cattell, J. R. Wygant, A. Keiling, and J. Scudder (2005), Alfvén waves and Poynting flux observed simultaneously by Polar and FAST in the plasma sheet boundary layer, *Journal of Geophysical Research*, 110(A12), A12S90, doi: 10.1029/2005JA011269.

Dungey, J. W. (1955), Electrodynamics of the Outer Atmosphere, *Tech. rep.*, London: The Physical Society, Cambridge.

Fenrich, F. R., J. C. Samson, G. Sofko, and R. A. Greenwald (1995), ULF high- and low- m field line resonances observed with the Super Dual Auroral Radar Network, *Journal of Geophysical Research: Space Physics*, 100(A11), 21,535–21,547, doi: 10.1029/95ja02024.

Fernandes, P. A., K. A. Lynch, M. Zettergren, D. L. Hampton, T. A. Bekkeng, I. J. Cohen, M. Conde, L. E. Fisher, P. Horak, M. R. Lessard, R. J. Miceli, R. G. Michell, J. Moen, and S. P. Powell (2016), Measuring the seeds of ion outflow: Auroral sounding rocket observations of low-altitude ion heating and circulation, *Journal of Geophysical Research A: Space Physics*, 121(2), 1587–1607, doi:10.1002/2015JA021536.

Figueiredo, S., G. T. Marklund, T. Karlsson, T. Johansson, Y. Ebihara, M. Ejiri, N. Ivchenko, P.-A. Lindqvist, H. Nilsson, and A. Fazakerley (2005), Temporal and spatial evolution of discrete auroral arcs as seen by Cluster, *Annales Geophysicae*, 23(7), 2531–2557, doi:10.5194/angeo-23-2531-2005.

Finlay, C. C., S. Maus, C. D. Beggan, T. N. Bondar, A. Chambodut, T. A. Chernova, A. Chulliat, V. P. Golovkov, B. Hamilton, M. Hamoudi, R. Holme, G. Hulot, W. Kuang, B. Langlais, V. Lesur, F. J. Lowes, H. Lühr, S. Macmillan, M. Mandea, S. McLean, C. Manoj, M. Menvielle, I. Michaelis, N. Olsen, J. Rauberg, M. Rother,

- T. J. Sabaka, A. Tangborn, L. Tøffner-Clausen, E. Thébault, A. W. Thomson, I. Wardinski, Z. Wei, and T. I. Zvereva (2010), International Geomagnetic Reference Field: The eleventh generation, *Geophysical Journal International*, 183(3), 1216–1230, doi:10.1111/j.1365-246X.2010.04804.x.
- Fisher, L. E., K. A. Lynch, P. A. Fernandes, T. A. Bekkeng, J. Moen, M. Zettergren, R. J. Miceli, S. Powell, M. R. Lessard, and P. Horak (2016), Including sheath effects in the interpretation of planar retarding potential analyzer's low-energy ion data, *Review of Scientific Instruments*, 87(4), 043,504, doi:10.1063/1.4944416.
- Getmantsev, G., N. Zuikov, D. Kotik, L. Mironenko, N. Mityakov, V. Rapoport, Y. Sazonov, V. Trakhtengerts, and V. Eidman (1974), Combination frequencies in the interaction between high-power short-wave radiation and ionospheric plasma, *ZhETF Pis. Red.*, 20, 101.
- Goertz, C. K., and R. W. Boswell (1979), Magnetosphere-ionosphere coupling, *Journal of Geophysical Research*, 84(A12), 7239, doi:10.1029/JA084iA12p07239.
- Gołkowski, M., U. S. Inan, A. R. Gibby, and M. B. Cohen (2008), Magnetospheric amplification and emission triggering by ELF/VLF waves injected by the 3.6 MW HAARP ionospheric heater, *Journal of Geophysical Research: Space Physics*, 113(10), doi: 10.1029/2008JA013157.
- Golkowski, M., M. B. Cohen, D. L. Carpenter, and U. S. Inan (2011), On the occurrence of ground observations of ELF/VLF magnetospheric amplification induced by the HAARP facility, *Journal of Geophysical Research: Space Physics*, 116(4), n/a–n/a, doi:10.1029/2010JA016261.
- Golub, G. H., and C. F. V. Loan (1996), *Matrix Computations*, The John Hopkins University Press, Baltimore.

- Grach, S. M., E. N. Sergeev, E. V. Mishin, and A. V. Shindin (2016), Dynamic properties of ionospheric plasma turbulence driven by high-power high-frequency radiowaves, *Physics-Uspekhi*, 59(11), 1091–1128, doi:10.3367/UFNe.2016.07.037868.
- Guido, T., B. Tulegenov, and A. V. Streltsov (2014), Large-amplitude ULF waves at high latitudes, *Journal of Atmospheric and Solar-Terrestrial Physics*, 119, 102–109, doi:10.1016/j.jastp.2014.07.006.
- Gurevich, A. V. (2007), Nonlinear effects in the ionosphere, *Physics-Uspekhi*, 50(11), 1091–1121, doi:10.1070/pu2007v050n11abeh006212.
- Gurevich, A. V. (2011), Nonlinear phenomena in the ionosphere, *Uspekhi Fizicheskikh Nauk*, 120(10), 319, doi:10.3367/ufnr.0120.197610f.0319.
- Hasegawa, A. (1976), PARTICLE ACCELERATION BY MHD SURFACE WAVE AND FORMATION OF AURORA., *J Geophys Res*, 81(28), 5083–5090, doi: 10.1029/JA081i028p05083.
- Hasegawa, A., and C. Uberoi (1982), The Alfvén wave, *Tech. rep.*, U.S. Department of Energy.
- Hiraki, Y., and T. Watanabe (2011), Feedback instability analysis for dipole configuration with ionospheric and magnetospheric cavities, *Journal of Geophysical Research: Space Physics*, 116(11), n/a–n/a, doi:10.1029/2011JA016721.
- Honary, F., N. Borisov, M. Beharrell, and A. Senior (2011), Temporal development of the magnetic zenith effect, *Journal of Geophysical Research: Space Physics*, 116(6), n/a–n/a, doi:10.1029/2010JA016029.
- Inan, U. S., H. C. Chang, R. A. Helliwell, W. L. Imhof, J. B. Reagan, and M. Walt (1985), Precipitation of radiation belt electrons by man-made waves: A comparison

between theory and measurement, *Journal of Geophysical Research: Space Physics*, 90(A1), 359–369, doi:10.1029/JA090iA01p00359.

Jasperse, J. R., B. Basu, E. J. Lund, and N. Grossbard (2010), The self-consistent parallel electric field due to electrostatic ion-cyclotron turbulence in downward auroral-current regions of the Earth's magnetosphere. IV, *Physics of Plasmas*, 17(6), 062,904, doi:10.1063/1.3443713.

Jia, N., and A. V. Streltsov (2014), Ionospheric feedback instability and active discrete auroral forms, *Journal of Geophysical Research: Space Physics*, 119(3), 2243–2254, doi:10.1002/2013JA019217.

Johansson, T., S. Figueiredo, T. Karlsson, G. Marklund, A. Fazakerley, S. Buchert, P.-A. Lindqvist, and H. Nilsson (2004), Intense high-altitude auroral electric fields - temporal and spatial characteristics, *Annales Geophysicae*, 22(7), 2485–2495, doi: 10.5194/angeo-22-2485-2004.

Johansson, T., T. Karlsson, G. Marklund, S. Figueiredo, P.-A. Lindqvist, and S. Buchert (2005), A statistical study of intense electric fields at 47 RE geocentric distance using Cluster, *Annales Geophysicae*, 23(7), 2579–2588, doi:10.5194/angeo-23-2579-2005.

Johansson, T., G. Marklund, T. Karlsson, S. Liléo, P.-A. Lindqvist, A. Marchaudon, H. Nilsson, and A. Fazakerley (2006), On the profile of intense high-altitude auroral electric fields at magnetospheric boundaries, *Annales Geophysicae*, 24(6), 1713–1723, doi:10.5194/angeo-24-1713-2006.

Karlsson, T., and G. T. Marklund (1996), A statistical study of intense low-altitude electric fields observed by Freja, *Geophysical Research Letters*, 23(9), 1005–1008, doi: 10.1029/96GL00773.

Karlsson, T., G. T. Marklund, S. Figueiredo, T. Johansson, and S. Buchert (2004),

Separating spatial and temporal variations in auroral electric and magnetic fields by Cluster multipoint measurements, *Annales Geophysicae*, 22(7), 2463–2472, doi: 10.5194/angeo-22-2463-2004.

Keiling, A., J. R. Wygant, C. Cattell, M. Temerin, F. S. Mozer, C. A. Kletzing, J. Scudder, C. T. Russell, W. Lotko, and A. V. Streltsov (2000), Large Alfvén wave power in the plasma sheet boundary layer during the expansion phase of substorms, *Geophysical Research Letters*, 27(19), 3169–3172, doi:10.1029/2000GL000127.

Kelley, M. C. (1989), *The Earth's Ionosphere*, Elsevier, doi:10.1016/B978-0-12-404013-7.X5001-1.

Kepko, L., H. E. Spence, and H. J. Singer (2002), ULF waves in the solar wind as direct drivers of magnetospheric pulsations, *Geophysical Research Letters*, 29(8), 39–1–39–4, doi:10.1029/2001GL014405.

Keskinen, M. J., H. G. Mitchell, J. A. Fedder, P. Satyanarayana, S. T. Zalesak, and J. D. Huba (1988), Nonlinear evolution of the kelvin-helmholtz instability in the high-latitude ionosphere, *Journal of Geophysical Research: Space Physics*, 93(A1), 137–152, doi:10.1029/JA093iA01p00137.

Kivelson, M. G., and D. J. Southwood (1985), Resonant ULF waves: A new interpretation, *Geophysical Research Letters*, 12(1), 49–52, doi:10.1029/GL012i001p00049.

Kosch, M. J., T. Pedersen, J. Hughes, R. Marshall, E. Gerken, A. Senior, D. Sentman, M. McCarrick, and F. T. Djuth (2005), Artificial optical emissions at HAARP for pump frequencies near the third and second electron gyro-harmonic, *Annales Geophysicae*, 23(5), 1585–1592, doi:10.5194/angeo-23-1585-2005.

Kosch, M. J., T. Pedersen, E. Mishin, S. Oyama, J. Hughes, A. Senior, B. Watkins, and B. Bristow (2007), Coordinated optical and radar observations of ionospheric pumping

- for a frequency pass through the second electron gyroharmonic at HAARP, *Journal of Geophysical Research: Space Physics*, 112(6), n/a–n/a, doi:10.1029/2006JA012146.
- Lessard, M. R., and D. J. Knudsen (2001), Ionospheric reflection of small-scale Alfvén waves, *Geophysical Research Letters*, 28(18), 3573–3576, doi:10.1029/2000GL012529.
- Lotko, W., A. V. Streltsov, and C. W. Carlson (1998), Discrete auroral arc, electrostatic shock and suprathermal electrons powered by dispersive, anomalously resistive field line resonance, *Geophysical Research Letters*, 25(24), 4449–4452, doi:10.1029/1998GL900200.
- Lundberg, E. T., P. M. Kintner, S. P. Powell, and K. A. Lynch (2012a), Multipayload interferometric wave vector determination of auroral hiss, *Journal of Geophysical Research: Space Physics*, 117(2), n/a–n/a, doi:10.1029/2011JA017037.
- Lundberg, E. T., P. M. Kintner, K. A. Lynch, and M. R. Mella (2012b), Multi-payload measurement of transverse velocity shears in the topside ionosphere, *Geophysical Research Letters*, 39(1), n/a–n/a, doi:10.1029/2011GL050018.
- Lynch, K. A., D. L. Hampton, M. Zettergren, T. A. Bekkeng, M. Conde, P. A. Fernandes, P. Horak, M. Lessard, R. Miceli, R. Michell, J. Moen, M. Nicolls, S. P. Powell, and M. Samara (2015), MICA sounding rocket observations of conductivity-gradient-generated auroral ionospheric responses: Small-scale structure with large-scale drivers, *Journal of Geophysical Research A: Space Physics*, 120(11), 9661–9682, doi:10.1002/2014JA020860.
- Lysak, R. L. (1990), Electrodynamic coupling of the magnetosphere and ionosphere, *Space Science Reviews*, 52(1-2), 33–87, doi:10.1007/BF00704239.
- Lysak, R. L. (1991), Feedback instability of the ionospheric resonant cavity, *Journal of Geophysical Research: Space Physics*, 96(A2), 1553–1568, doi:10.1029/90ja02154.

- Lysak, R. L., and Y. Song (1996), Coupling of kelvin-helmholtz and current sheet instabilities to the ionosphere: A dynamic theory of auroral spirals, *Journal of Geophysical Research: Space Physics*, 101(A7), 15,411–15,422, doi:10.1029/96JA00521.
- Lysak, R. L., and Y. Song (2002), Energetics of the ionospheric feedback interaction, *Journal of Geophysical Research: Space Physics*, 107(A8), SIA 6–1–SIA 6–13, doi: 10.1029/2001JA000308.
- Mann, I. R., A. N. Wright, and P. S. Cally (1995), Coupling of magnetospheric cavity modes to field line resonances: A study of resonance widths, *Journal of Geophysical Research*, 100(A10), 19,441, doi:10.1029/95JA00820.
- Marklund, G., L. Blomberg, C.-G. Fälthammar, and P.-A. Lindqvist (1994), On intense diverging electric fields associated with black aurora, *Geophysical Research Letters*, 21(17), 1859–1862, doi:10.1029/94GL00194.
- Marklund, G., T. Karlsson, and J. Clemons (1997), On low-altitude particle acceleration and intense electric fields and their relationship to black aurora, *Journal of Geophysical Research A: Space Physics*, 102(A8), 17,509–17,522, doi:10.1029/97JA00334.
- Mishin, E. V., W. J. Burke, and T. Pedersen (2004), On the onset of HF-induced airglow at HAARP, *Journal of Geophysical Research: Space Physics*, 109(A2), doi: 10.1029/2003JA010205.
- Mishin, E. V., W. J. Burke, and T. Pedersen (2005), HF-induced airglow at magnetic zenith: Theoretical considerations, *Annales Geophysicae*, 23(1), 47–53, doi: 10.5194/angeo-23-47-2005.
- Mishin, E. V., B. Watkins, N. Lehtinen, B. Eliasson, T. Pedersen, and S. Grach (2016), Artificial ionospheric layers driven by high-frequency radiowaves: An assessment, *Journal of Geophysical Research A: Space Physics*, 121(4), 3497–3524, doi:

10.1002/2015JA021823.

- Miura, A., S. Ohtsuka, and T. Tamao (1982), Coupling instability of the shear Alfvén wave in the magnetosphere with the ionospheric ion drift wave, 2. Numerical analysis, *Journal of Geophysical Research*, 87(A2), 843, doi:10.1029/JA087iA02p00843.
- Moen, J., K. Oksavik, T. Abe, M. Lester, Y. Saito, T. A. Bekkeng, and K. S. Jacobsen (2012), First in-situ measurements of HF radar echoing targets, *Geophysical Research Letters*, 39(7), n/a–n/a, doi:10.1029/2012GL051407.
- Mozer, F. S. (2011), Anomalous Resistivity and Parallel Electric Fields, pp. 125–136, doi:10.1007/978-94-010-1503-5\_2.
- Nakamura, T. K. (2000), Parallel electric field of a mirror kinetic Alfvén wave, *Journal of Geophysical Research: Space Physics*, 105(A5), 10,729–10,737, doi:10.1029/1999ja900494.
- Papadopoulos, K., A. S. Sharma, and C. L. Chang (1989), On the efficient operation of a plasma ELF antenna driven by modulation of ionospheric currents, *Comments Plasma Phys. Controlled Fusion*, 12(1), 1–17.
- Papadopoulos, K., C. L. Chang, P. Vitello, and A. Drobot (1990), On the efficiency of ionospheric ELF generation, *Radio Science*, 25(6), 1311–1320, doi:10.1029/RS025i006p01311.
- Papadopoulos, K., T. Wallace, M. McCarrick, G. M. Milikh, and X. Yang (2003), On the efficiency of ELF/VLF generation using HF heating of the auroral electrojet, *Plasma Physics Reports*, 29(7), 561–565, doi:10.1134/1.1592554.
- Paschmann, G., S. Haaland, and R. Treumann (2012), *Auroral Plasma Physics*, 500 pp., Springer Netherlands, doi:10.1007/978-94-007-1086-3.

- Pedersen, T., B. Gustavsson, E. Mishin, E. MacKenzie, H. C. Carlson, M. Starks, and T. Mills (2009), Optical ring formation and ionization production in high-power HF heating experiments at HAARP, *Geophysical Research Letters*, 36(18), L18,107, doi: 10.1029/2009GL040047.
- Pedersen, T., B. Gustavsson, E. Mishin, E. Kendall, T. Mills, H. C. Carlson, and A. L. Snyder (2010), Creation of artificial ionospheric layers using high-power HF waves, *Geophysical Research Letters*, 37(2), n/a–n/a, doi:10.1029/2009GL041895.
- Pokhotelov, O. A., D. Pokhotelov, A. Streltsov, V. Khruschev, and M. Parrot (2000), Dispersive ionospheric Alfvén resonator, *Journal of Geophysical Research: Space Physics*, 105(A4), 7737–7746, doi:10.1029/1999ja900480.
- Pokhotelov, O. A., V. Khruschev, M. Parrot, S. Senchenkov, and V. P. Pavlenko (2001), Ionospheric Alfvén resonator revisited: Feedback instability, *Journal of Geophysical Research: Space Physics*, 106(A11), 25,813–25,824, doi:10.1029/2000ja000450.
- Polyakov, S. V., and V. O. Rapoport (1981), The ionospheric Alfvén resonator, *Geomagn. Aeron.*, 21(5), 610–614.
- Radoski, H. R. (1967), A note on oscillating field lines, *Journal of Geophysical Research*, 72(1), 418, doi:10.1029/JZ072i001p00418.
- Rankin, R., B. G. Harrold, J. C. Samson, and P. Frycz (1993), The nonlinear evolution of field line resonances in the earth's magnetosphere, *Journal of Geophysical Research: Space Physics*, 98(A4), 5839–5853, doi:10.1029/92JA01606.
- Rankin, R., F. Fenrich, and V. T. Tikhonchuk (2000), Shear AlfvéN waves on stretched magnetic field lines near midnight in Earth's magnetosphere, *Geophysical Research Letters*, 27(20), 3265–3268, doi:10.1029/2000GL000029.

Rietveld, M. T., M. J. Kosch, N. F. Blagoveshchenskaya, V. A. Kornienko, T. B. Leyser, and T. K. Yeoman (2003), Ionospheric electron heating, optical emissions, and striations induced by powerful HF radio waves at high latitudes: Aspect angle dependence, *Journal of Geophysical Research: Space Physics*, 108(A4), 1141, doi: 10.1029/2002JA009543.

Robinson, T. R., G. Bond, P. Eglitis, F. Honary, and M. T. Rietveld (1998), RF heating in a strong auroral electrojet, *Advances in Space Research*, 21(5), 689–692, doi: 10.1016/S0273-1177(97)01004-1.

Rother, M., K. Schlegel, and H. Lühr (2007), CHAMP observation of intense kilometer-scale field-aligned currents, evidence for an ionospheric Alfvén resonator, *Annales Geophysicae*, 25(7), 1603–1615, doi:10.5194/angeo-25-1603-2007.

Ruohoniemi, J. M., R. A. Greenwald, K. B. Baker, and J. C. Samson (1991), HF radar observations of Pc 5 field line resonances in the midnight/early morning MLT sector, *Journal of Geophysical Research: Space Physics*, 96(A9), 15,697–15,710, doi: 10.1029/91JA00795.

Russell, A. J. B., and A. N. Wright (2010), Resonant absorption with 2D variation of field line eigenfrequencies, *Astronomy and Astrophysics*, 511, A17, doi:10.1051/0004-6361/200912669.

Samson, J. C., T. J. Hughes, F. Creutzberg, D. D. Wallis, R. A. Greenwald, and J. M. Ruohoniemi (1991), Observations of a detached, discrete arc in association with field line resonances, *Journal of Geophysical Research: Space Physics*, 96(A9), 15,683–15,695, doi:10.1029/91JA00796.

Samson, J. C., D. D. Wallis, T. J. Hughes, F. Creutzberg, J. M. Ruohoniemi, and R. A. Greenwald (1992), Substorm intensifications and field line resonances in

the nightside magnetosphere, *Journal of Geophysical Research*, 97(A6), 8495, doi: 10.1029/91JA03156.

Samson, J. C., L. L. Cogger, and Q. Pao (1996), Observations of field line resonances, auroral arcs, and auroral vortex structures, *Journal of Geophysical Research: Space Physics*, 101(A8), 17,373–17,383, doi:10.1029/96JA01086.

Sato, T. (1978), A theory of quiet auroral arcs, *Journal of Geophysical Research*, 83(A3), 1042, doi:10.1029/JA083iA03p01042.

Seyler, C. E. (1990), A mathematical model of the structure and evolution of small-scale discrete auroral arcs, *Journal of Geophysical Research*, 95(A10), 17,199, doi: 10.1029/JA095iA10p17199.

Southwood, D. (1974), Some features of field line resonances in the magnetosphere, *Planetary and Space Science*, 22(3), 483–491, doi:10.1016/0032-0633(74)90078-6.

Stasiewicz, K., P. Bellan, C. Chaston, C. Kletzing, R. Lysak, J. Maggs, O. Pokhotelov, C. Seyler, P. Shukla, L. Stenflo, A. Streltsov, and J.-E. Wahlund (2000), Small scale Alfvénic structure in the aurora, *Space Science Reviews*, 92(3-4), 423–533, doi: 10.1023/A:1005207202143.

Streltsov, A. V. (2011), Effect of heavy ions on coupling between density structures and electromagnetic waves in the auroral zone, *Journal of Geophysical Research: Space Physics*, 116(10), n/a–n/a, doi:10.1029/2011JA016550.

Streltsov, A. V., and T. Karlsson (2008), Small-scale, localized electromagnetic waves observed by Cluster: Result of magnetosphere-ionosphere interactions, *Geophysical Research Letters*, 35(22), L22,107, doi:10.1029/2008GL035956.

Streltsov, A. V., and W. Lotko (2003), Small-scale electric fields in downward

auroral current channels, *Journal of Geophysical Research*, 108(A7), 1289, doi: 10.1029/2002JA009806.

Streltsov, A. V., and W. Lotko (2004), Multiscale electrodynamics of the ionosphere-magnetosphere system, *Journal of Geophysical Research: Space Physics*, 109(A9), A09,214, doi:10.1029/2004JA010457.

Streltsov, A. V., and W. Lotko (2008), Coupling between density structures, electromagnetic waves and ionospheric feedback in the auroral zone, *Journal of Geophysical Research: Space Physics*, 113(5), n/a–n/a, doi:10.1029/2007JA012594.

Streltsov, A. V., and T. R. Pedersen (2010), An alternative method for generation of ULF waves by ionospheric heating, *Geophysical Research Letters*, 37(14), n/a–n/a, doi:10.1029/2010GL043543.

Streltsov, A. V., and T. R. Pedersen (2011), Excitation of zero-frequency magnetic field-aligned currents by ionospheric heating, *Annales Geophysicae*, 29(6), 1147–1152, doi:10.5194/angeo-29-1147-2011.

Streltsov, A. V., W. Lotko, J. R. Johnson, and C. Z. Cheng (1998a), Small-scale, dispersive field line resonances in the hot magnetospheric plasma, *Journal of Geophysical Research: Space Physics*, 103(A11), 26,559–26,572, doi:10.1029/98ja02679.

Streltsov, A. V., W. Lotko, J. R. Johnson, and C. Z. Cheng (1998b), Small-scale, dispersive field line resonances in the hot magnetospheric plasma, *Journal of Geophysical Research: Space Physics*, 103(A11), 26,559–26,572, doi:10.1029/98JA02679.

Streltsov, A. V., W. Lotko, and G. M. Milikh (2005), Simulation of ULF field-aligned currents generated by HF heating of the ionosphere, *Journal of Geophysical Research: Space Physics*, 110(A4), doi:10.1029/2004JA010629.

- Streltsov, A. V., T. R. Pedersen, E. V. Mishin, and A. L. Snyder (2010), Ionospheric feedback instability and substorm development, *Journal of Geophysical Research: Space Physics*, 115(A7), doi:10.1029/2009JA014961.
- Streltsov, A. V., C. L. Chang, J. Labenski, G. Milikh, A. Vartanyan, and A. L. Snyder (2011), Excitation of the ionospheric Alfvén resonator from the ground: Theory and experiments, *Journal of Geophysical Research: Space Physics*, 116(10), n/a–n/a, doi: 10.1029/2011JA016680.
- Streltsov, A. V., N. Jia, T. R. Pedersen, H. U. Frey, and E. D. Donovan (2012), ULF waves and discrete aurora, *Journal of Geophysical Research: Space Physics*, 117(A9), n/a–n/a, doi:10.1029/2012JA017644.
- Streltsov, A. V., J.-J. Berthelier, A. A. Chernyshov, V. L. Frolov, F. Honary, M. J. Kosch, R. P. McCoy, E. V. Mishin, and M. T. Rietveld (2018), Past, Present and Future of Active Radio Frequency Experiments in Space, *Space Science Reviews*, 214(8), 118, doi:10.1007/s11214-018-0549-7.
- Stubbe, P., and H. Kopka (1977), Modulation of the polar electrojet by powerful HF waves, *Journal of Geophysical Research*, 82(16), 2319–2325, doi: 10.1029/JA082i016p02319.
- Stubbe, P., H. Kopka, and R. L. Dowden (1981), Generation of ELF and VLF waves by polar electrojet modulation: Experimental results, *Journal of Geophysical Research*, 86(A11), 9073, doi:10.1029/JA086iA11p09073.
- Sugiura, M., and C. R. Wilson (1964), Oscillation of the geomagnetic field lines and associated magnetic perturbations at conjugate points, *Journal of Geophysical Research*, 69(7), 1211–1216, doi:10.1029/JZ069i007p01211.
- Trakhtengerts, V. Y., and A. Y. Feldstein (1987), About excitation of small-scale elec-

tromagnetic perturbations in ionospheric Alfvén resonator, *Geomagn. Aeron.*, 2(7), 315.

Trakhtengerts, V. Y., and A. Y. Feldstein (1991), Turbulent Alfvén boundary layer in the polar ionosphere: 1. Excitation conditions and energetics, *Journal of Geophysical Research*, 96(A11), 19,363, doi:10.1029/91ja00376.

Trakhtengertz, V. Y., and A. Y. Feldstein (1984), Quiet auroral arcs: Ionosphere effect of magnetospheric convection stratification, *Planetary and Space Science*, 32(2), 127–134, doi:10.1016/0032-0633(84)90147-8.

Tulegenov, B., and A. V. Streltsov (2017), Ionospheric Alfvén resonator and aurora: Modeling of MICA observations, *Journal of Geophysical Research: Space Physics*, 122(7), 7530–7540, doi:10.1002/2017JA024181.

Tulegenov, B., and A. V. Streltsov (2019), Effects of the Hall Conductivity in Ionospheric Heating Experiments, *Geophysical Research Letters*, 46(12), 6188–6194, doi: 10.1029/2019gl083340.

Tulegenov, B., A. V. Streltsov, E. Kendall, M. McCarrick, and I. Galkin (2019), Artificial Aurora Produced by HAARP, *Journal of Geophysical Research: Space Physics*, pp. 3255–3265, doi:10.1029/2019ja026607.

Walker, A. D. M., J. M. Ruohoniemi, K. B. Baker, R. A. Greenwald, and J. C. Samson (1992), Spatial and temporal behavior of ULF pulsations observed by the Goose Bay HF Radar, *Journal of Geophysical Research*, 97(A8), 12,187, doi:10.1029/92JA00329.

Watanabe, T., H. Oya, K. Watanabe, and T. Sato (1993), Comprehensive Simulation Study on Local and Global Development of Auroral Arcs and Field-Aligned Potentials, *Journal of Geophysical Research*, 98(A12), 21,391–21,407, doi: 10.1029/93JA01769.

- Wygant, J. R., A. Keiling, C. A. Cattell, M. Johnson, R. L. Lysak, M. Temerin, F. S. Mozer, C. A. Kletzing, J. D. Scudder, W. Peterson, C. T. Russell, G. Parks, M. Brittnacher, G. Germany, and J. Spann (2000), Polar spacecraft based comparisons of intense electric fields and Poynting flux near and within the plasma sheet-tail lobe boundary to UVI images: An energy source for the aurora, *Journal of Geophysical Research: Space Physics*, 105(A8), 18,675–18,692, doi:10.1029/1999JA900500.
- Xu, B. L., J. C. Samson, W. W. Liu, F. Creutzberg, and T. J. Hughes (1993), Observations of optical aurora modulated by resonant Alfvén waves, *Journal of Geophysical Research*, 98(A7), 11,531, doi:10.1029/93JA00435.
- Yahnin, A. G., N. V. Semenova, A. A. Ostapenko, J. Kangas, J. Manninen, and T. Tu runen (2003), Morphology of the spectral resonance structure of the electromagnetic background noise in the range of 0.14 Hz at  $L = 5.2$ , *Annales Geophysicae*, 21(3), 779–786, doi:10.5194/angeo-21-779-2003.
- Zettergren, M., K. Lynch, D. Hampton, M. Nicolls, B. Wright, M. Conde, J. Moen, M. Lessard, R. Miceli, and S. Powell (2014), Auroral ionospheric F region density cavity formation and evolution: MICA campaign results, *Journal of Geophysical Research: Space Physics*, 119(4), 3162–3178, doi:10.1002/2013JA019583.